UNIVERSITY OF OKLAHOMA

GRADUATE COLLEGE

FLUVIAL ARCHITECTURE OF THE BURRO CANYON FORMATION USING UAV-BASED PHOTOGRAMMETRY - IMPLICATIONS FOR RESERVOIR PERFORMANCE, ESCALANTE CANYON, SOUTHWESTERN PICEANCE BASIN, COLORADO

A THESIS

SUBMITTED TO THE GRADUATE FACULTY

in partial fulfillment of the requirements for the

Degree of

MASTER OF SCIENCE

By

SARAH CLARK
Norman, Oklahoma
2018

FLUVIAL ARCHITECTURE OF THE BURRO CANYON FORMATION USING UAV-BASED PHOTOGRAMMETRY - IMPLICATIONS FOR RESERVOIR PERFORMANCE, ESCALANTE CANYON, SOUTHWESTERN PICEANCE BASIN, COLORADO

A THESIS APPROVED FOR THE
CONOCOPHILLIPS SCHOOL OF GEOLOGY AND GEOPHYSICS

BY

Dr. Matthew J. Pranter, Chair

Dr. John D. Pigott

Dr. Rex D. Cole

This is dedicated to my husband, Neal, and our family. With your love and support, I was able to accomplish some of my geology dreams with no reservations throughout this graduate school adventure.

ACKNOWLEDGMENTS

This research was funded through the Reservoir Characterization and Modeling Laboratory at the University of Oklahoma. I would like to recognize Dr. Matthew Pranter for his patience, guidance, and enthusiastic support throughout the course of this project. I would like to recognize Dr. Rex Cole, Dr. John Pigott, and Dr. Zulfiquar Reza for their advice and technical guidance. I would like to recognize Schlumberger for their donation of Petrel E&P and ECLIPSE software and Spectrum Petrographics, Inc. for making the thin sections used in my research. Lastly, I would like to thank my friends and fellow students for all their support and assistance.

TABLE OF CONTENTS

LIST OF TABLES

LIST OF FIGURES

ABSTRACT

The Cretaceous Burro Canyon Formation in the southern Piceance Basin, Colorado represents low-sinuosity to sinuous braided fluvial deposits that consist of amalgamated channel complexes, amalgamated and isolated fluvial-bar channel fills, and floodplain deposits. Lithofacies primarily include granule-cobble conglomerates, conglomeratic sandstones, cross-stratified sandstones, upward-fining sandstones, and gray-green mudstones. To assess the effects of variable sandstone-body geometry and internal lithofacies and petrophysical heterogeneity on reservoir performance, conventional field methods are combined with unmanned-aerial-vehicle- (UAV-) based photogrammetry to create representative outcrop-based reservoir models. Outcrop reservoir models and fluid-flow simulations compare three reservoir scenarios of the Burro Canyon Formation based on stratigraphic variability, sandstone-body geometry, and lithofacies heterogeneity. Simulation results show that lithofacies variability can account for almost 50% variation in breakthrough time. Internal channel-bounding surfaces reduce breakthrough time by 2%, volumetric sweep efficiency by 8%, and recovery efficiency by 10%. Three lateral grid resolutions and two permeability-upscaling methods for each reservoir scenario are explored in fluid-flow simulations to investigate how upscaling impacts reservoir performance. Results show that coarsely resolved grids experience delayed breakthrough by as much as 40% and greater volumetric sweep efficiency by an average of 10%. Permeability models that are upscaled using a geometric mean preserve slightly higher values than those using a harmonic mean. For upscaling based on a geometric mean, breakthrough times are delayed by an average of 17% and volumetric sweep efficiency is reduced by as much as 10%. Results of the study highlight the importance of properly incorporating

stratigraphic details into 3-D reservoir models and preserving those details through proper upscaling methods.

INTRODUCTION

Fluvial reservoirs are heterogeneous at different scales as related to the stratigraphic framework, architectural elements, and lithofacies. At the bedding and lithofacies scale, it has been shown that sedimentary structures have a significant control on porosity and permeability heterogeneity and associated fluid flow (e.g., Weber, 1982; Hurst and Rosvoll, 1991; Corbett and Jensen, 1993; Jackson et al., 2003). Fluvial lithofacies associations (architectural elements - different types of fluvial sandstone bodies) exhibit internal heterogeneity that impacts fluid-flow (e.g., Fustic et al. 2011; Hubbard, et al., 2011; Labrecque, et al., 2011), and fluvial reservoir connectivity varies at the field scale owing to the stratigraphic variability in sandstone-body stacking patterns (e.g., Willis, 2007; Pranter et al., 2009; Smith et al., 2009). Therefore, to create reservoir models that are representative in terms of storage and flow characteristics, it is essential to model the spatial distribution of permeability and other properties that are tied to the individual lithofacies, architectural elements, and the stratigraphy. Different scales of detail are critical; however, common practices of modeling fluvial reservoirs do not explicitly address all of these sedimentological details. Importantly, the significance of these fluvial stratigraphic features on secondary recovery has not been rigorously evaluated using geologically constrained fluid-flow simulation models.

Deposits of the Cretaceous Burro Canyon Formation in the Piceance Basin, Colorado were investigated using both outcrop and subsurface data (core data). In the study area, the Burro Canyon Formation is overlain unconformably by the Cretaceous Dakota Formation and underlain unconformably by the Upper Jurassic Morrison

Formation (Figure 1). The Cretaceous rocks outcrop in eastern and southeastern Utah and northwestern Colorado and have previously been interpreted as mainly braided to meandering river and floodplain deposits. However, details regarding the environment of deposition and the reservoir-scale sedimentology and stratigraphy are limited. Stokes (1952) identified the age of the Burro Canyon Formation as Early Cretaceous in both Utah and Colorado utilizing fossil assemblages from outcrops.

Young (1960, 1973) studied the Dakota Group on the Colorado Plateau, which includes the Cedar Mountain (equivalent to the Burro Canyon Formation) and the Naturita Formation (now termed the Dakota Formation). The study interpreted the lithofacies and environments of deposition in outcrops in Utah and Colorado. The interval is interpreted as a transgressive system with deposits progressing from inland environments in the Cedar Mountain Formation, through coastal in the Naturita Formation, and marine in the overlying Mancos Shale. Young (1960) also showed that the sandstone bodies found in Escalante Canyon below the green mudstone are equivalent to both the lower and middle Cedar Mountain Sandstones to the west by recording and correlating 150 stratigraphic sections throughout the Colorado Plateau. Young (1970, 1975) regionally correlated the lithology and environments of deposition of Lower Cretaceous deposits in the study area and surrounding areas using outcrop-based studies. Since the 1970s, there has been limited published work on the stratigraphy, lithofacies, and depositional setting of the Burro Canyon Formation in the southern Piceance Basin. Most recently, several studies have been conducted on similar Upper Cretaceous fluvial and shallow-marine deposits of the Mesaverde Group in the southern Piceance Basin using similar methods of investigation to this study. The

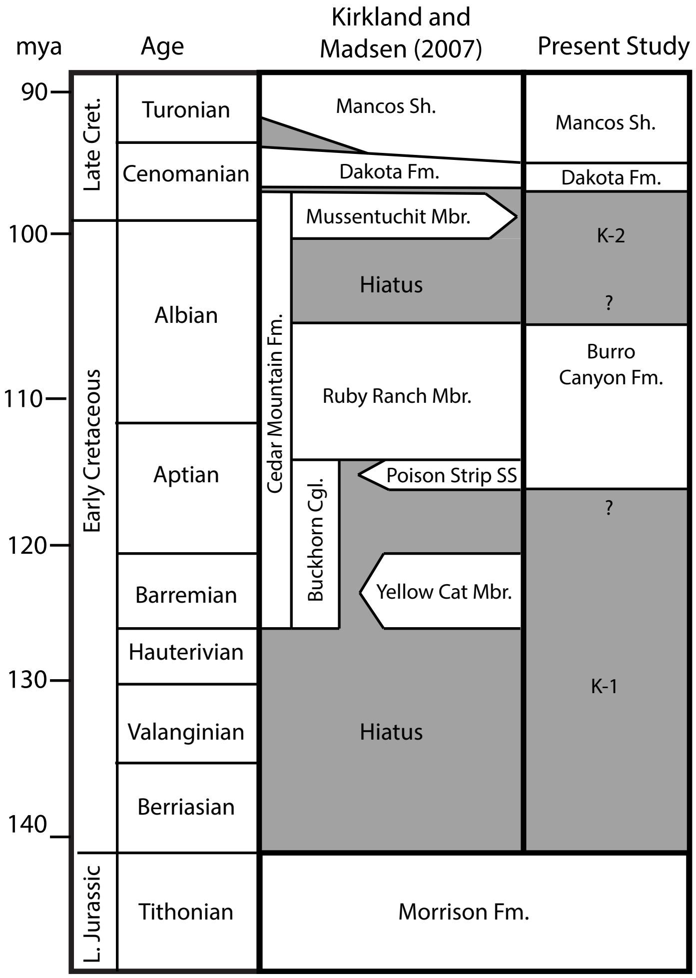

Figure 1. Stratigraphic nomenclature used in this study and past studies. The Cretaceous deposits have been divided and named multiple ways by varying studies in the past. The Burro Canyon Formation is the target of this study. Modified from Cole (2017, personal communication)

environments of deposition and reservoir characteristics of the units were described using outcrop and subsurface data. Cole and Cumella (2003, 2005), Ellison (2004), and Pranter et al. (2007) explored reservoir-scale lithologic heterogeneity of fluvial point bars of the Williams Fork Formation in the southern Piceance Basin using conventional sedimentological studies of outcrops combined with 2-D and 3-D outcrop-based modeling. Fluvial sandstone-body geometry and dimensions were captured and interpreted using high-resolution ground-based light detection and ranging (LIDAR) data, photomosaics, and field measurements. Outcrop models and flow simulations were used to compare scenarios of heterogeneity based on different lithologies, shale drapes, observed-grain size trends, petrophysical properties, and modeling methods to demonstrate how breakthrough time and sweep efficiency are affected by different levels of heterogeneity.

The limited studies of the Burro Canyon interval have focused mainly on the regional stratigraphy and age of the formation and none have investigated the interval at smaller scale. To better understand the 1) reservoir-scale sedimentology and stratigraphy of the Burro Canyon interval and 2) the significance of the different scales of fluvial heterogeneity, this study expands on relevant previous work and analyzes lithofacies, architectural elements, and their characteristics to interpret the environment of deposition and evaluate the stratigraphic variability of the deposits.

One well-exposed outcrop locality, Escalante Canyon along the Gunnison River in Delta County, Colorado, was analyzed (Figure 2). This location was chosen because of its accessibility, lack of vegetation, and its ideal orientation of outcrop areas trending

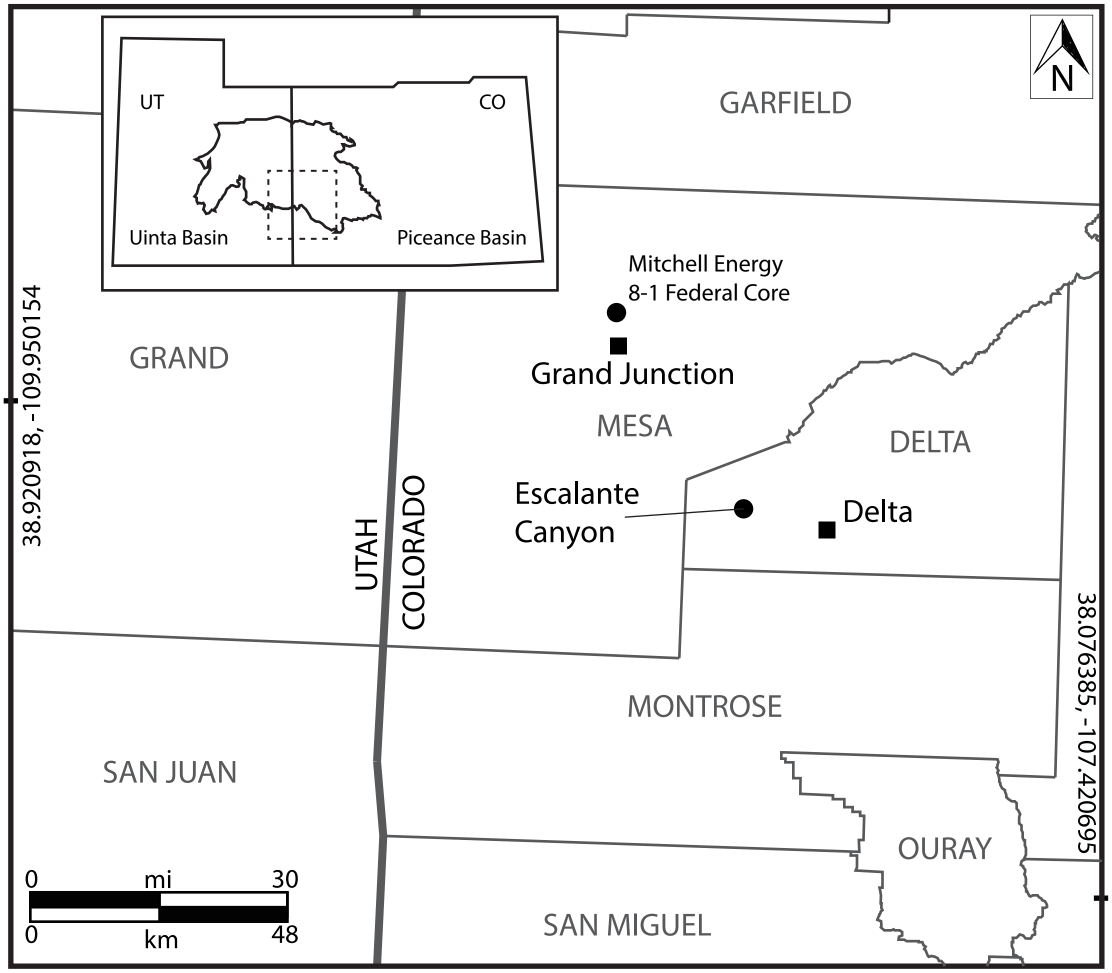

Figure 2. Location map of eastern Utah and Western Colorado with inset map of Uinta and Piceance basins area. The study area, Escalante Canyon, is located in Delta County, Colorado. Petrophysical data from the Mitchell Energy 8-1 Federal core (API 05-077-08026), in Mesa County, Colorado, is used in outcrop reservoir modeling in this study.

west-east along the Gunnison River and southwest-northeast along the exposed canyons providing a ‘three-dimensional’ outcrop.

This study explores the significance of different levels of fluvial heterogeneity on production performance using multiscale fluvial reservoir modeling and fluid-flow simulations from the scale of facies to that of amalgamated channel complexes. Model construction and quantification of stratigraphic and sedimentological heterogeneity sequentially includes additional smaller scales of stratigraphic detail beginning with 1) 2-D model construction of fluvial reservoir stratigraphic heterogeneity; 2) incorporation of sandstone-body (architectural-element) scale analysis and modeling; and 3) incorporation of smaller scale bedding / lithofacies modeling of internal architectural-element heterogeneity. Each smaller scale of heterogeneity is added to the previous larger-scale features. Importantly, secondary recovery performance is evaluated to determine the significance of stratigraphic and sedimentological features on dynamic processes. Multiple two-dimensional static and dynamic outcrop-based models of the Burro Canyon Formation were constructed using commercial software. Additionally, the implication of upscaling geologic-model grid resolution (cell size) for fluid-flow simulation is investigated in terms of breakthrough time, volumetric sweep efficiency, and recovery efficiency.

GEOLOGIC SETTING

The Piceance Basin is a northwest-southeast-trending basin surrounded by the White River uplift to the east, Axial arch and Uinta Mountains to the north, Douglas Creek arch to the west, Uncompahgre uplift to the southwest, Gunnison uplift and Elk Mountains to the south, and Sawatch uplift to the southeast (Johnson, 1989). The basin began forming in the Late Cretaceous (Campanian) during the Laramide Orogeny (c. 75-40 Ma) (Johnson and Flores, 2003).

The Piceance Basin now resides in an area once dominated by a much larger Rocky Mountain Foreland Basin System that was created by the Sevier Orogeny (c. 140-50 Ma) (Johnson and Flores, 2003). Clastic sediments were carried from the Sevier belt to the northeast by multiple pulses of sedimentation owing to the rising orogenic movement in the Early Aptian, with periods of less active erosion and meandering stream systems in between each of the pulses. During early Albian time, a shallow sea approached the basin from the north and south bringing new depositional environments to the former coastal plain (Appendix A). The sea spread and approached northwestern Colorado from the northeast drastically shrinking the coastal plain just prior to the end of the Albian (Young, 1975). Basin development during the Early Cretaceous through early Late Jurassic basin was dominantly caused by flexural subsidence while Late Cretaceous to mid-Cenozoic time saw basin partitioning caused by basement-involved Laramide structures (DeCelles, 2004). (See summaries in Johnson and Flores, 2003; DeCelles, 2004).

The Burro Canyon Formation is Aptian-Albian in age and lies unconformably on top of the Morrison Formation and is overlain unconformably by the Dakota

Formation (Figure 1). The Burro Canyon Formation in Colorado is the stratigraphic equivalent to the Cedar Mountain Formation in Utah. It is composed of mainly sandstones and conglomerates that are regularly encountered in the lower half of the Burro Canyon Formation and are thought to be deposited by northeast-east trending braided-river systems within incised valleys from a source in the Sevier Orogenic belt (Young, 1975). A green mudstone is also common through the upper portion of the Burro Canyon Formation and was most likely deposited in a meandering stream, floodplain, or lacustrine environment (Young, 1975; Cole, 2017, personal communication).

METHODOLOGY

Conventional Field Methods

To analyze the stratigraphy and interpret the environment of deposition of the Burro Canyon Formation, two stratigraphic sections (measured sections MS-1 and MS-2) were measured and described along the west and east sides of 650 road in Escalante Canyon (Figure 3; Appendix A). The measured sections cover approximately 160 m (524 ft) and traverse through the upper portions of the Morrison, Burro Canyon, and Dakota formations. The measured sections include descriptions of lithology, grain size, sedimentary structures, paleocurrent indicators, and bounding surfaces. A Brunton Compass was used to acquire paleocurrent measurements (N=120) by measuring dip and azimuth of cross-stratification and scour surfaces. Outcrop gamma-ray measurements were also acquired along both measured section traverses to assist in lithology identification and for comparison to subsurface well logs (comparison to the Mitchell Energy 8-1 Federal core in Mesa County, Colorado). Total-count gamma-ray (GR) data were acquired using a 0.3-m (1-ft) spacing with a Super-Spec RS-125 scintillometer (Radiation Solutions, Inc.).

UAV-based Photogrammetry

High-resolution, calibrated images of the 816 m- (2677 ft-) long, south-facing exposure along the Gunnison River were captured at multiple distances using a DJI Phantom 3 drone (Unmanned Aerial Vehicle – UAV) (Figure 3). Images are from approximately 3 m (10 ft) away from the outcrop face to facilitate identification of small-scale sedimentary structures and lithofacies associations in areas that were not

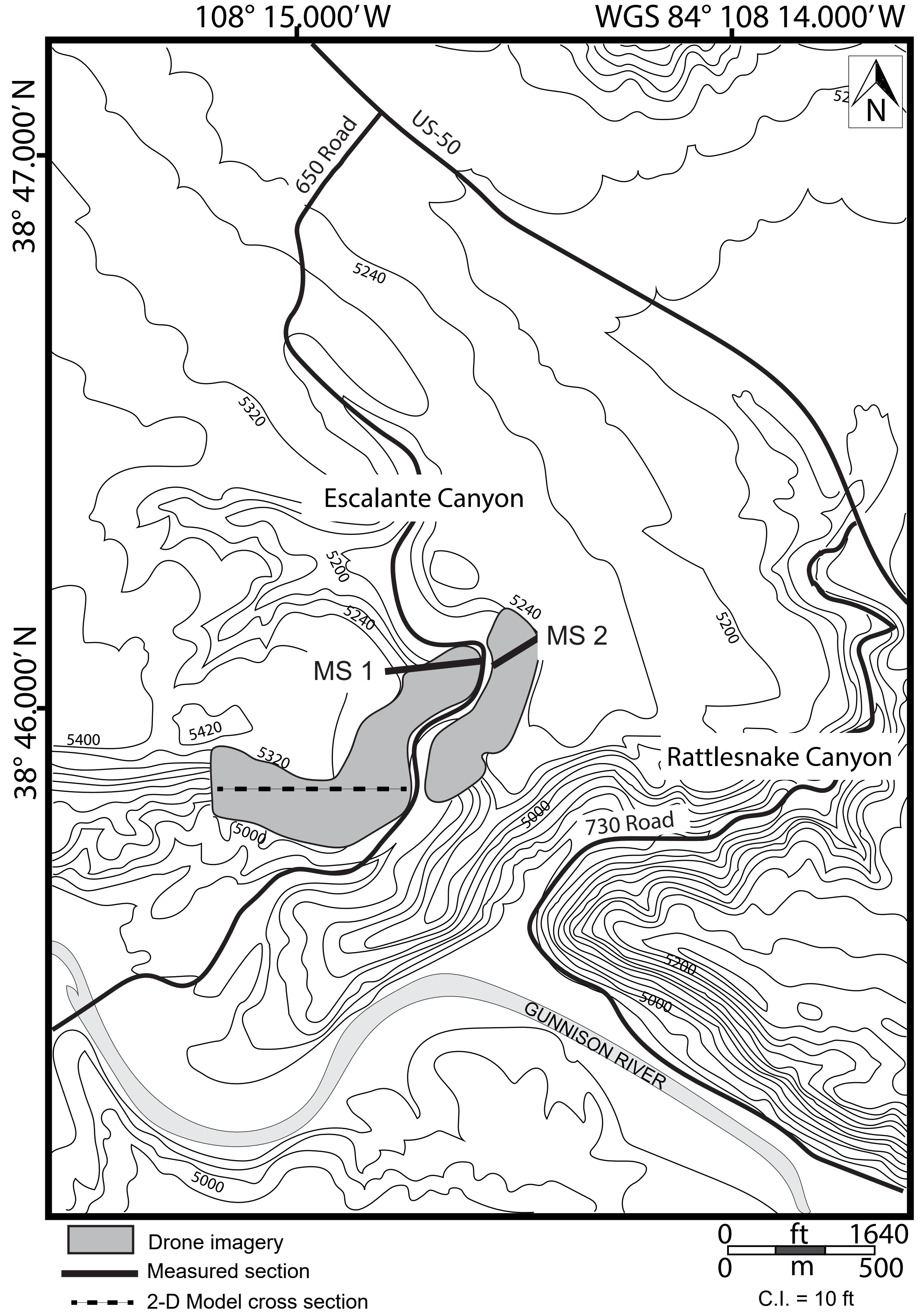
108° 15.000′W
WGS 84° 108 14.000′W
38° 47.000′ N
38° 46.000′ N
N
US-50
650 Road
5240
5320
5200
Escalante Canyon
5240
5240
MS 2
MS 1
5200
5400
5420
5320
Rattlesnake Canyon
5000
730 Road
5000
5200
5000
GUNNISON RIVER
5000
Drone imagery
Measured section
2-D Model cross section
0 ft 1640
0 m 500
C.I. = 10 ft

Figure 3. Topographic map of Escalante Canyon, Delta County, Colorado. Measured sections, MS 1 and MS 2, were taken along the west and east sides of the canyon (black lines) and drone images were acquired along 650 Road in the canyon and on the south-facing wall along the Gunnison River (grey shading). The cross-section of the outcrop reservoir models created in the study is indicated by the black dashed line.

accessible (Appendix B). A second set of images was acquired from a distance of approximately 15-30 m (50-100 ft) to provide data to capture the large-scale features of the outcrop, correlate stratigraphic surfaces, map and measure architectural elements and their bounding surfaces, and evaluate how those elements vary stratigraphically. Multiple three-dimensional renderings of the outcrop were produced using the georeferenced images in Pix4DMapper Pro software (Figure 4). UAV imaging requires specific conditions and techniques for capturing the images and post-processing to produce the highest resolution and most complete dataset to create 3-D models (Appendix B).

Width and thickness values of sandstone bodies were measured from the georeferenced 3-D renderings of the outcrop in Pix4DMapper Pro to assist in interpretations of the architectural elements in the Burro Canyon Formation, and the accuracy of the measurements was validated by features with known length placed in the images at the time of acquisition (Appendix A). Utilizing both measured sections and UAV-based imaging, four properties were considered to define architectural elements: bounding surfaces, scale, external geometry, and internal geometry (Miall, 1985).

Measured sections recorded in Escalante Canyon were used to interpret lithofacies and bounding surfaces observed in the 3-D outcrop rendering. Thirteen vertical ‘pseudo wells’ were created at approximately 0.4 ha- (1 ac-; 0.001 mi^2) spacing (50 m [164 ft] between pseudo wells) across the outcrop and lithofacies and bounding surfaces were recorded along their traverses (Figure 4). The pseudo wells were imported into Petrel and discrete lithofacies logs were created from the measured

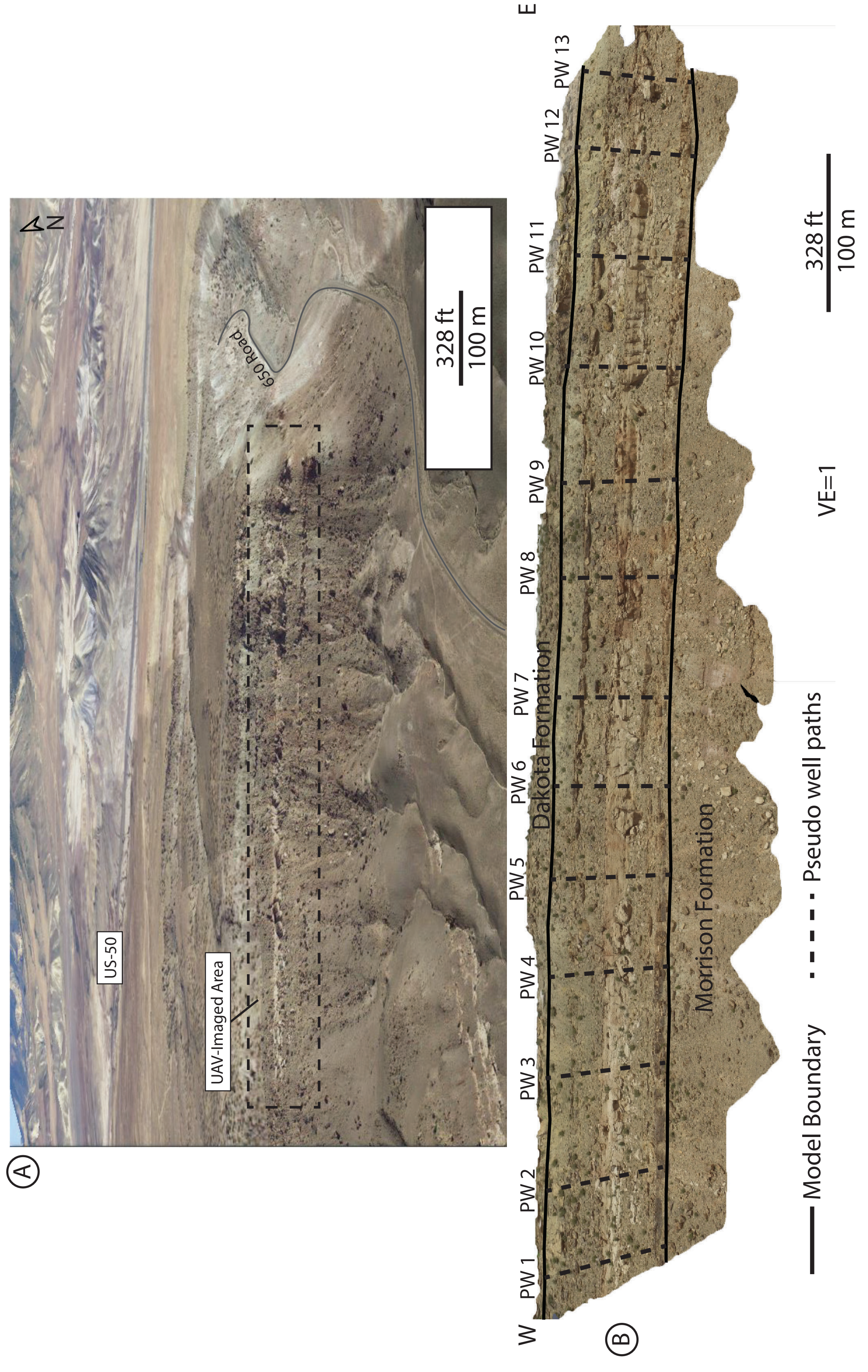
A
N
US-50
UAV-Imaged Area
650 Road
328 ft
100 m
B
W
E
PW 1
PW 2
PW 3
PW 4
PW 5
PW 6
PW 7
PW 8
PW 9
PW 10
PW 11
PW 12
PW 13
Dakota Formation
Morrison Formation
Model Boundary
Pseudo well paths
VE=1
328 ft
100 m

Figure 4. (A) An overview image of Escalante Canyon. View is from the south-facing outcrop chosen for reservoir modeling (B) and the outcrop cut along 650 Road used for recording measured sections. (B) The southern-facing wall of Escalante Canyon along the Gunnison River was chosen for the outcrop reservoir models owing to excellent exposure of the sandstone bodies of the Burro Canyon formation. The 13 pseudo wells (PW 1-13) used to create lithofacies logs along their traverses are shown as black dashed lines. The reservoir model boundaries are indicated by solid black lines.

section interpretations and from the drone imagery to constrain lithofacies models (Figure 5). Bounding surfaces were also interpreted in the outcrop rendering and were imported into Petrel and digitized as surfaces to create zones for the three model scenarios.

Outcrop Reservoir Modeling

Three 2-dimensional outcrop-based reservoir models (Models 1-3) of the Burro Canyon Formation along the 816 m- (2677 ft -) long exposure (Figure 3) were constructed using commercial software to explore the different scales of fluvial heterogeneity observed in Escalante Canyon. The models were created with a 1 m x 1 m (3.2 ft x 3.2 ft) lateral grid size to capture small-scale variations in facies and petrophysical trends. The models are approximately 816 m x 25 m x 60 m (2677 ft x 82 ft x 196 ft) in the x-, y-, and z-directions of a Cartesian-grid system and vary in total number of cells: Model 1 is 13,623,475 cells, Model 2 is 17,933,150 cells, and Model 3 is 25,715,075 cells. The number and shape of zones changes in each model, but layering was kept at 0.1 m (0.3 ft) for all reservoir zones to capture the finer stratigraphic variation (Figure 6; Appendix C). The three models (Models 1-3) were created to represent increasing levels of heterogeneity to explore their effects on fluid flow. Model 1 is the least heterogeneous scenario and contains only cross-stratified sandstone and gray-green mudstone lithofacies with reservoir bodies in contact with injector and producer wells (Figure 6A). Model 2 is an intermediate scenario with five lithofacies and the addition of isolated reservoir bodies (Figure 6B). Model 3 is the most heterogeneous scenario and the closest approximation to the actual outcrop. It contains

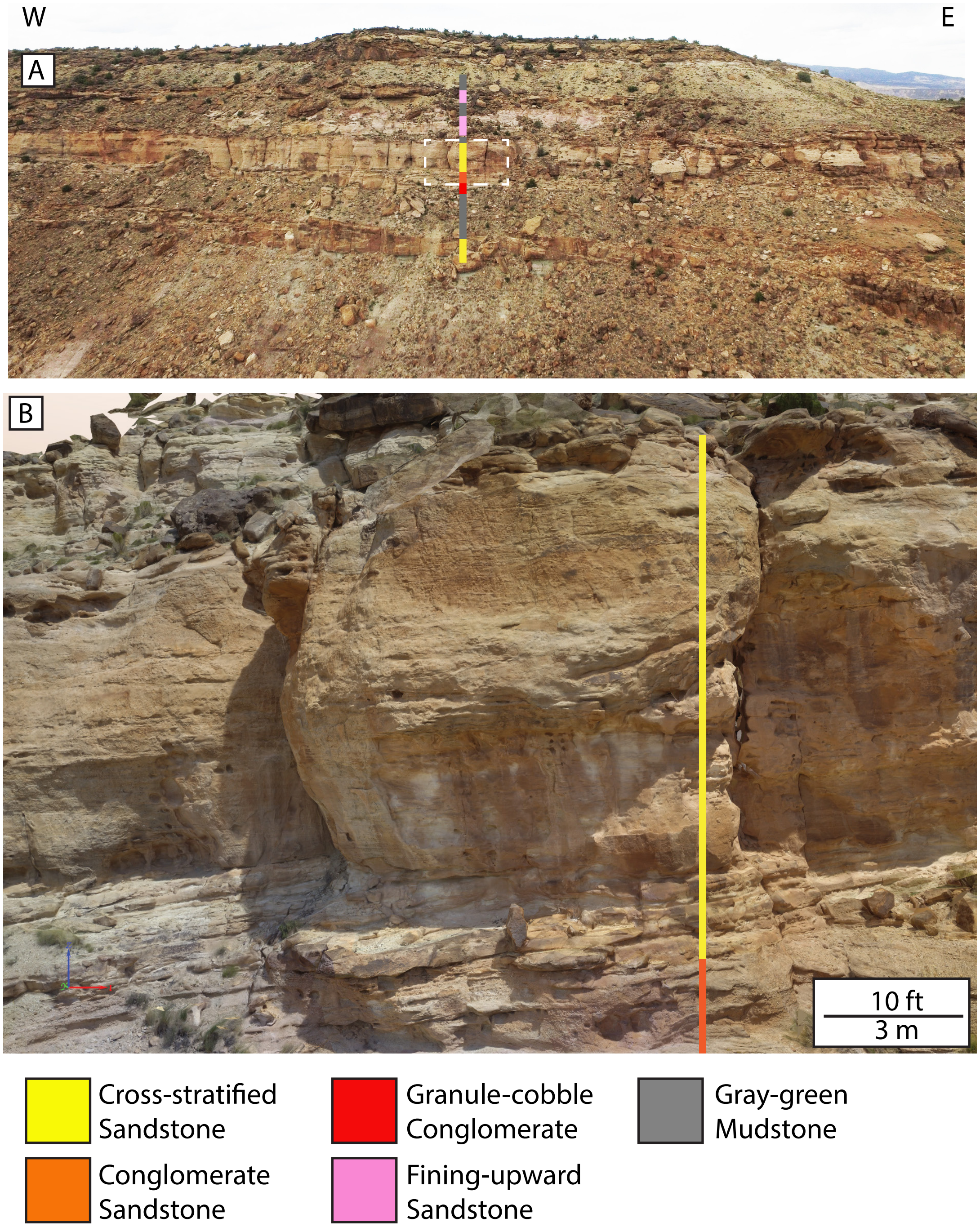

Figure 5. (A) Overview image of the outcrop in Escalante Canyon used for reservoir modeling, showing an example of a lithofacies log created along a pseudo well traverse. UAV-based outcrop renderings were created in Pix4DMapper Pro and used to interpret lithofacies within the Burro Canyon Formation to apply to outcrop reservoir modeling. (B) Image captured with the DJI Phantom 3 from ~ 3 m (10 ft) away from the rock face along the pseudo well shown in (A) to capture small-scale details such as lithology and sedimentary structures. An example lithofacies log is interpreted along the image. The 13 pseudo wells with interpreted logs were then used to constrain lithofacies models later in the study.

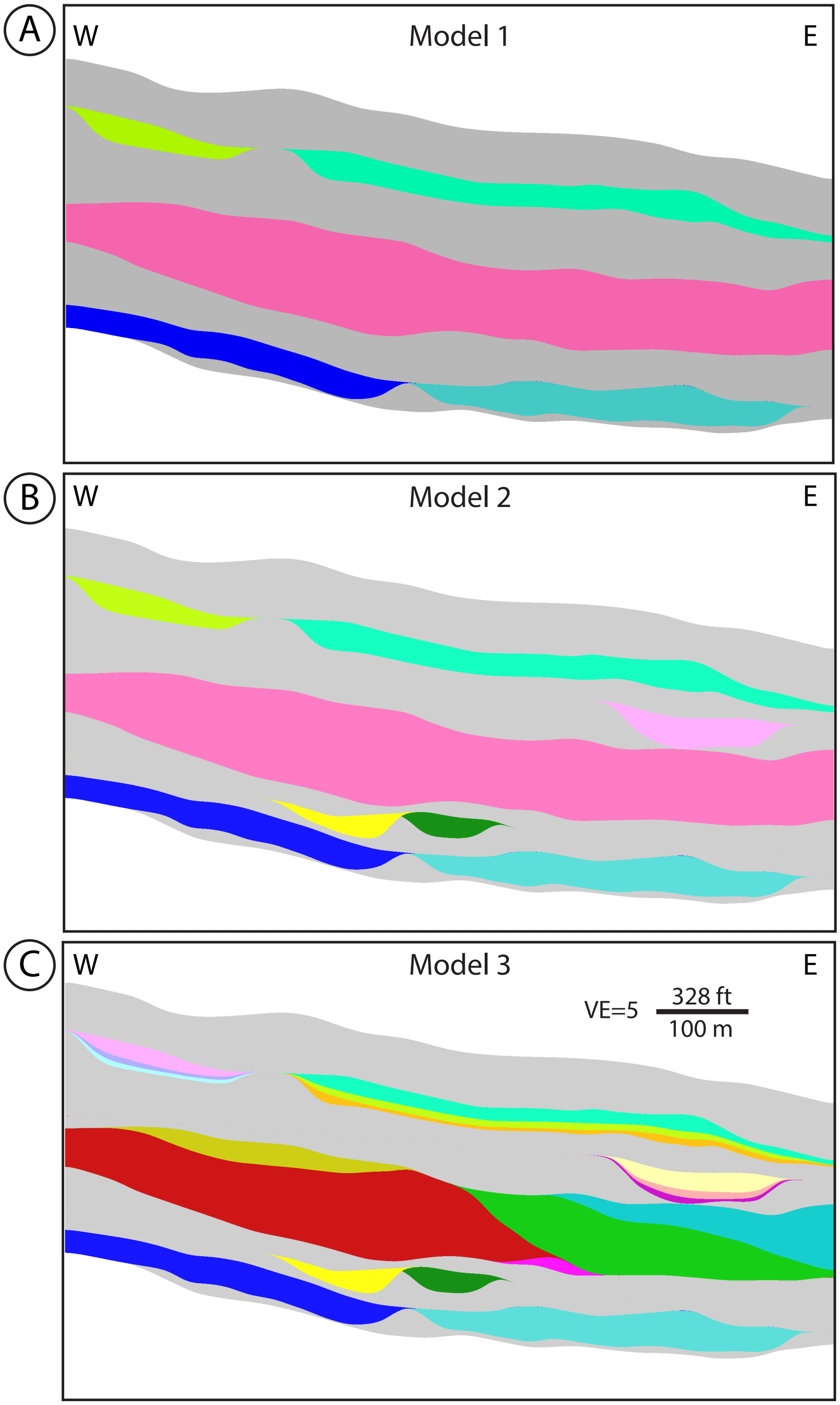
A
W
Model 1
E
B
W
Model 2
E
C
W
Model 3
E
VE=5
328 ft
100 m

Figure 6. Two-dimensional stratigraphic framework for each model scenario (Model 1-3). (A) Model 1 is the least heterogeneous and contains 9 zones (each zone is indicated by a unique color except for floodplain facies in grey). (B) Model 2 contains 14 zones. (C) Model 3 is the most heterogeneous scenario and contains 24 zones. The models all contain a 1 x 1 m (3.2 x 3.2 ft) lateral grid and reservoir zones (non-mudstone) are divided into 0.1 m (0.3 ft) vertical layers. Models are 816 x 25 x 57 m (2677 x 82 x 196 ft) in the x-, y-, and z-directions of a Cartesian grid system. Total cells contained in the models are: Model 1: 13,623,475; Model 2: 17,933,150; Model 3: 25,715,075.

five lithofacies, additional zones based on channel-bounding surfaces, and petrophysical trends imposed in some reservoir zones where decreasing-upward porosity is associated with fining-upward sandstones and conglomeratic sandstones (Figure 6C). Models were constructed at reservoir depth utilizing the Burro Canyon Formation depths from the Mitchell Energy 8-1 Federal core to accurately represent the temperature and pressure environment during the fluid-flow simulation process.

Lithofacies Modeling

Lithofacies models were created for the three lithofacies scenarios (Models 1-3) using sequential-indicator simulation and are constrained to the model zones (stratigraphic framework), lithofacies logs for measured sections and pseudo wells, lithofacies percentages from outcrop, and variogram inputs based on measurements of the lateral and vertical continuity of lithofacies acquired from a UAV-based 3-D rendering of the outcrop (Appendix C). The outcrop is oriented approximately perpendicular to the paleo-flow direction of 51°, so the major direction of continuity is set to 51° for all models and zones.

Petrophysical Modeling

Porosity and permeability models were created for the three lithofacies scenarios (Models 1-3) using sequential-Gaussian simulation and were conditioned to the corresponding lithofacies model. Porosity and permeability data were obtained from the Mitchell Energy 8-1 Federal core in Mesa County, Colorado (Figure 2; Appendix C). Minimum, maximum, and mean values and the standard deviation were used to establish porosity and permeability histograms for each lithofacies and used to constrain the models (Appendix C). In all models, non-reservoir zones (mudstone lithofacies) were set to 0% for porosity and 0 mD for permeability. Variogram information was assigned based on values used in the lithofacies models with consideration of published values in other fluvial-reservoir modeling studies (Appendix C) (e.g., Pranter et al., 2009). Model 3 includes upward-decreasing porosity-depth trends for zones containing upward-fining sandstone and conglomeratic sandstone lithofacies (Appendix C). The trends were created in two ways depending on if the zone exhibits a single upward-fining trend or multiple upward-fining cycles: 1) a linear function in stratigraphic depth assuming isotropic conditions in the horizontal plane that created a continuous trend through the whole reservoir zone, and 2) for zones containing multiple cycles of thin-bedded (~0.3 m; ~1 ft) upward-fining sandstone, porosity logs were created for the pseudo wells and used to impose the trends at smaller intervals. Permeability models were created with core-derived data distributions and co-kriging was used to constrain permeability to the porosity models to ensure the permeability models relate to porosity trends for each scenario. Uniform porosity and permeability models were also created for each model scenario by assigning an average porosity and permeability value to the fine-to-medium grained cross-stratified sandstone facies. These models represent the most simplistic petrophysical models (base case) to compare to more complex scenarios during fluid-flow experiments.

Model Upscaling

Owing to limitations in computational power and associated run time, small-scale geologic models must often be upscaled prior to fluid-flow simulation. The original static outcrop models are detailed and geologically accurate and include many cells (cell counts varied from 13 to 26 million cells), therefore, upscaling was required. Importance is placed on using appropriate upscaling methods to maintain important small-scale geological features that effect fluid flow, while still coarsening the grid adequately to simulate fluid flow within a reasonable timeframe.

Averaging (volume-weighted) algorithms were used to aerially upscale lithofacies and petrophysical models from a 1 m x 1 m (3.2 ft x 3.2 ft) grid to three larger grid sizes: 2 m x 2 m (6.5 ft x 6.5 ft), 4 m x 4 m (13 ft x 13 ft), and 8 m x 8 m (26.2 ft x 26.2 ft) to assess the effects of upscaling on reservoir performance. Only the aerial cell dimensions were upscaled; vertical upscaling was not done to the model layers. It is important to note that the stratigraphic details were preserved vertically. For lithofacies upscaling, the most abundant lithofacies is assigned to the upscaled model cell. For porosity upscaling, the arithmetic mean is calculated for the upscaled model cell. Two averaging methods, harmonic and geometric, were used to coarsen the permeability models for each grid size to assess the effects of upscaling methods on reservoir performance (Appendix C). Six unique grids for each of the three model scenarios were produced and one uniform scenario (average values of porosity and permeability for sandstone) was created for each grid size and model scenario. The result is a total of 27-simulation scenarios that were evaluated (Table 1).

Effect of Fluvial Reservoir Heterogeneity on Waterflood Performance

Table 1. Summary of upscaled models used in fluid-flow simulations. Model names indicate BC= Burro Canyon, M1= Model 1, M2= Model 2, M3= Model 3; 2x2= 2 x 2 m lateral grid, 4x4= 4 x 4 m lateral grid, 8x8= 8 x 8 m lateral grid; H= harmonic, G= geometric. Uniform property model simulations are not included in list but were created and used in flow simulations for each grid size in each model scenario.

Model Name	Algorithm	Averaging Method (Porosity)	Averaging Method (Permeability)	Total Number Cells
Model 1_2X2H	Averaging (volume-weighted)	Arithmetic	Harmonic	3532464
Model 1_2X2G	Averaging (volume-weighted)	Arithmetic	Geometric	
Model 1_4X4H	Averaging (volume-weighted)	Arithmetic	Harmonic	815184
Model 1_4X4G	Averaging (volume-weighted)	Arithmetic	Geometric	
Model 1_8X8H	Averaging (volume-weighted)	Arithmetic	Harmonic	204102
Model 1_8X8G	Averaging (volume-weighted)	Arithmetic	Geometric	
Model 2_2X2H	Averaging (volume-weighted)	Arithmetic	Harmonic	4651608
Model 2_2X2G	Averaging (volume-weighted)	Arithmetic	Geometric	
Model 2_4X4H	Averaging (volume-weighted)	Arithmetic	Harmonic	1073448
Model 2_4X4G	Averaging (volume-weighted)	Arithmetic	Geometric	
Model 2_8X8H	Averaging (volume-weighted)	Arithmetic	Harmonic	270504
Model 2_8X8G	Averaging (volume-weighted)	Arithmetic	Geometric	
Model 3_2X2H	Averaging (volume-weighted)	Arithmetic	Harmonic	6667128
Model 3_2X2G	Averaging (volume-weighted)	Arithmetic	Geometric	
Model 3_4X4H	Averaging (volume-weighted)	Arithmetic	Harmonic	1534896
Model 3_4X4G	Averaging (volume-weighted)	Arithmetic	Geometric	
Model 3_8X8H	Averaging (volume-weighted)	Arithmetic	Harmonic	386478
Model 3_8X8G	Averaging (volume-weighted)	Arithmetic	Geometric	

To investigate the effect of fluvial-reservoir heterogeneity (lithological and petrophysical) and the impact of upscaling geological models on reservoir performance, subsurface fluid-flow was simulated over a 15-year period using a commercial reservoir simulation software. Waterflood performance in light oil reservoirs was investigated using an injector-producer pair. The injection and production wells were placed on the west (left) and east (right) sides of the outcrop models, respectively. The wells penetrate the entire thickness of the model and only reservoir zones were completed for both wells. Effect of heterogeneity and model resolution on frontal displacement within waterflood settings were determined. Simulations are evaluated in terms of 1) breakthrough time (BTT), 2) volumetric sweep efficiency at breakthrough time, 3) recovery efficiency at breakthrough time and at 15 years, and 4) cumulative production of oil, gas, and water at 15 years.

Initial reservoir pressure and fluid distributions, and operational conditions were kept the same for all 27 scenarios explored. Parameters for fluids, initial conditions, relative permeability and compaction used in these scenarios are presented in Table 2. Petrophysical properties, namely porosity and permeability as described previously, were used for each unique grid scenario. Permeability was considered laterally isotropic, while vertical permeability anisotropy was set at 0.1.

Production was controlled by a maximum allowable flow rate from the producing well initially and when pressure declined, a minimum bottom-hole pressure was imposed. Water injection was controlled by a maximum injection flow rate and a maximum bottom-hole pressure limit (Table 2).

Ⓐ

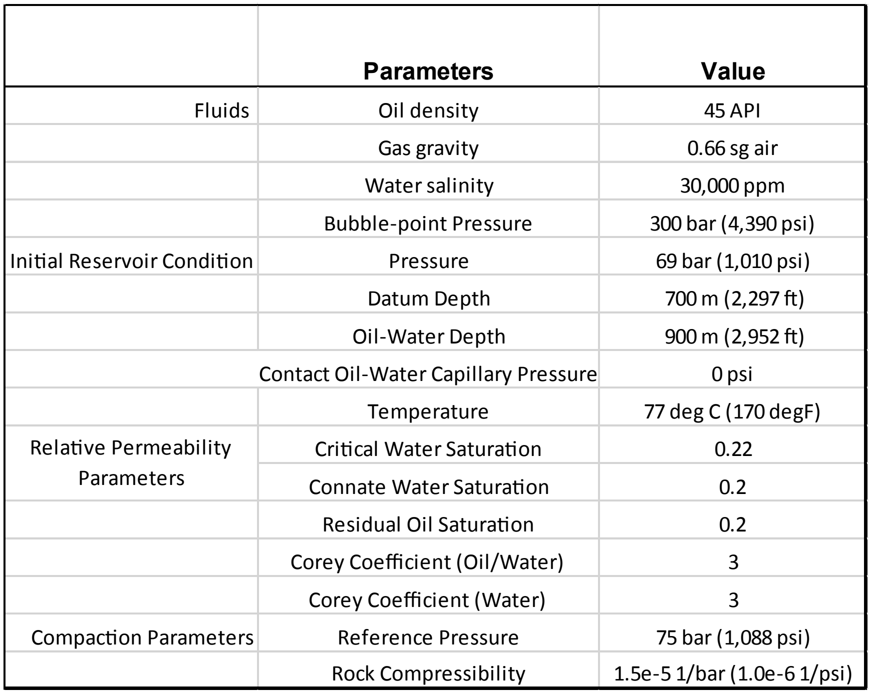

	Parameters	Value
Fluids	Oil density	45 API
	Gas gravity	0.66 sg air
	Water salinity	30,000 ppm
	Bubble-point Pressure	300 bar (4,390 psi)
Initial Reservoir Condition	Pressure	69 bar (1,010 psi)
	Datum Depth	700 m (2,297 ft)
	Oil-Water Depth	900 m (2,952 ft)
	Contact Oil-Water Capillary Pressure	0 psi
	Temperature	77 deg C (170 degF)
Relative Permeability Parameters	Critical Water Saturation	0.22
	Connate Water Saturation	0.2
	Residual Oil Saturation	0.2
	Corey Coefficient (Oil/Water)	3
	Corey Coefficient (Water)	3
Compaction Parameters	Reference Pressure	75 bar (1,088 psi)
	Rock Compressibility	1.5e-5 1/bar (1.0e-6 1/psi)

Ⓑ

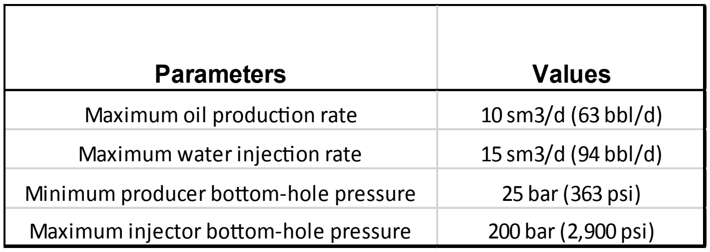

Parameters	Values
Maximum oil production rate	10 sm3/d (63 bbl/d)
Maximum water injection rate	15 sm3/d (94 bbl/d)
Minimum producer bottom-hole pressure	25 bar (363 psi)
Maximum injector bottom-hole pressure	200 bar (2,900 psi)

Table 2. Summary of parameters used in fluid-flow simulations. Parameters were held constant through all simulations. (A) Reservoir inputs for simulations. (B) Controls on injection and production throughout simulations.

RESULTS

Lithofacies and Stratigraphic Architecture

Burro Canyon Formation lithofacies from MS 1 and 2 are 1) granule-cobble conglomerate, 2) conglomeratic sandstone, 3) cross-stratified sandstone, 4) fining-upward sandstone, and 5) gray-green mudstone (Figure 7; Table 3). Cross-stratified sandstone is the dominant facies of the interval and is commonly associated with relatively large-scale amalgamated channel complexes, while gray-green mudstone commonly encases sandstone bodies in non-amalgamated channel complexes. Conglomerate and sandstone facies are considered reservoir facies and mudstone facies are non-reservoir for the outcrop reservoir models.

An idealized stratigraphic section that combines data from two measured sections illustrates the common facies associations (Figure 8; Appendix E). For the Burro Canyon Formation, a general fining-upward succession exists. A granule-cobble conglomerate lies at the base of the formation at the K-1 unconformity with conglomeratic sandstone facies directly overlying it. Cross-stratified sandstone overlies the conglomeratic sandstone and is the most abundant facies in this area. The cross-stratified sandstone generally thins and fines upward and is overlain by the slightly coarser grained fining-upward sandstone facies. Fining-upward sandstone lies directly below the gray-green mudstone facies.

The stratigraphic architecture of the Burro Canyon Formation follows the hierarchy of alluvial strata established by Patterson et al. (2002; 2010), which describes three facies associations composed of small-scale hierarchical elements that vertically stack to create both the external geometry of the reservoir zones and the small-scale,

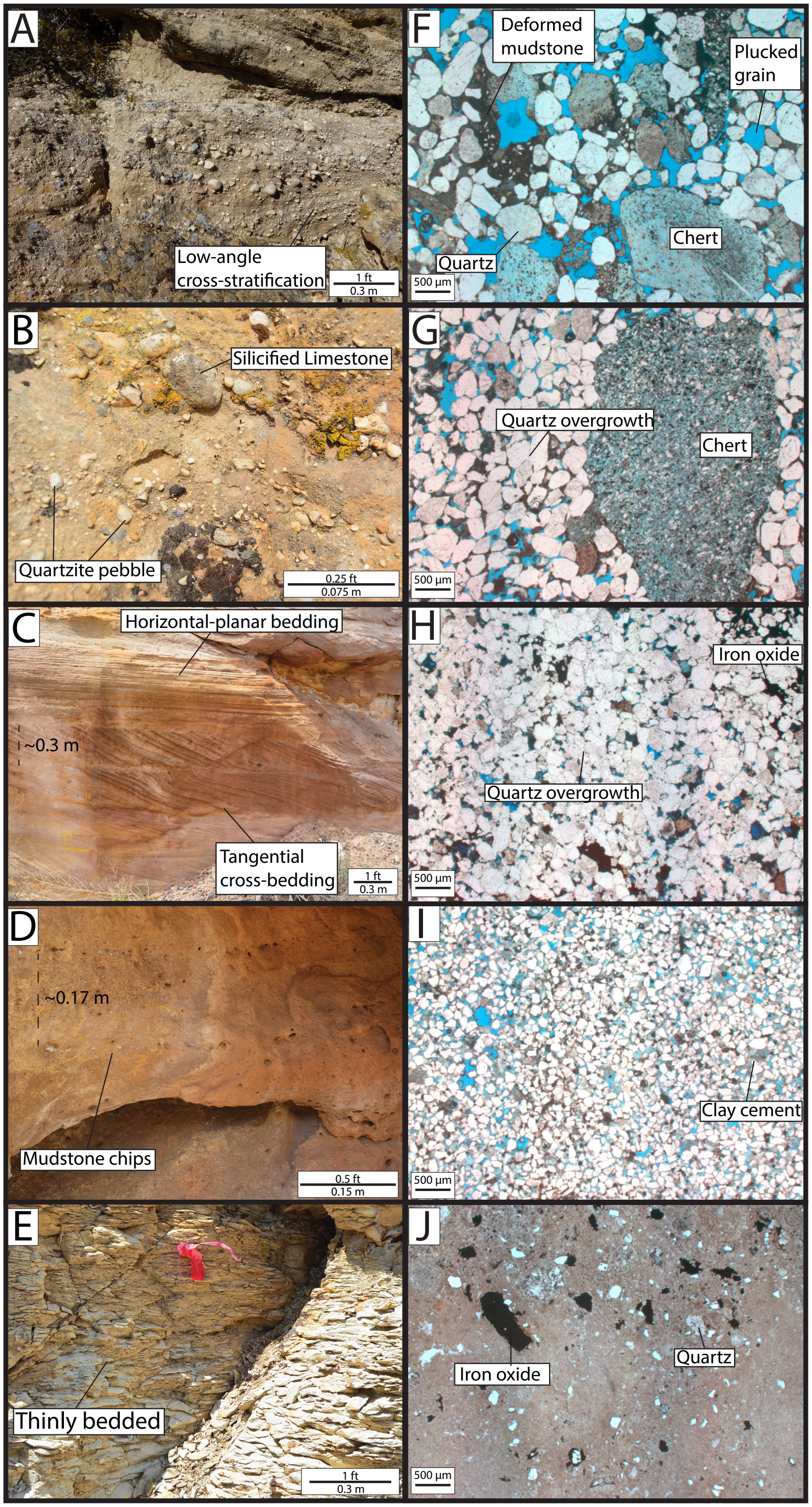
A
Low-angle cross-stratification
1 ft
0.3 m
F
Deformed mudstone
Plucked grain
Chert
Quartz
500 µm
B
Silicified Limestone
Quartzite pebble
0.25 ft
0.075 m
G
Quartz overgrowth
Chert
500 µm
C
Horizontal-planar bedding
~0.3 m
Tangential cross-bedding
1 ft
0.3 m
H
Iron oxide
Quartz overgrowth
500 µm
D
~0.17 m
Mudstone chips
0.5 ft
0.15 m
I
Clay cement
500 µm
E
Thinly bedded
1 ft
0.3 m
J
Iron oxide
Quartz
500 µm

Figure 7. Key facies of the Burro Canyon Formation shown in outcrop (A-E) and in thin section (F-J). Thin sections are in plane-polarized light and is stained red for calcite (epoxy is blue). (A; F) granule-cobble conglomerate, (B; G) conglomeratic sandstone, (C; H) cross-stratified sandstone, (D; I) fining-upward sandstone, (E; J) gray-green mudstone. These lithofacies were used to populate lithofacies models (Models 1-3).

Formation	Facies	Grain Size	Grain Shape/ Sorting	Dominant Features	Environment of Deposition
Burro Canyon	granule-cobble conglomerate	very coarse sand matrix; <7 cm clasts	subangular, moderately sorted matrix; round-subround clasts	low-angle cross-stratification	braided fluvial
Burro Canyon	conlomeratic sandstone	medium-very coarse sand matrix; <9 cm clasts	subround, moderately sorted matrix; subround clasts	large-scale low-angle inclined bedding, clasts commonly found in densley clustered lenses; graded bedding	braided fluvial, channel fill
Burro Canyon	cross-stratified sandstone	fine-medium	subround-subangular, well sorted	varying medium-scale cross-stratification, gravel lag at scour surfaces (limestone and quartzite)	braided fluvial, channel fill
Burro Canyon	fining-upward sandstone	fine-medium	subangular, fining upward cycles	low-angle inclined bedding; mudchips along base of cycles	sinous fluvial, decreasing system energy
Burro Canyon	gray-green mudstone	clay	N/A	unconsolidated, structureless to silicified and thinly laminated	floodplain

Table 3. Summary of key lithofacies observed in the Burro Canyon Formation in Escalante Canyon. (Grain shape interpretations based on Powers, 1953)

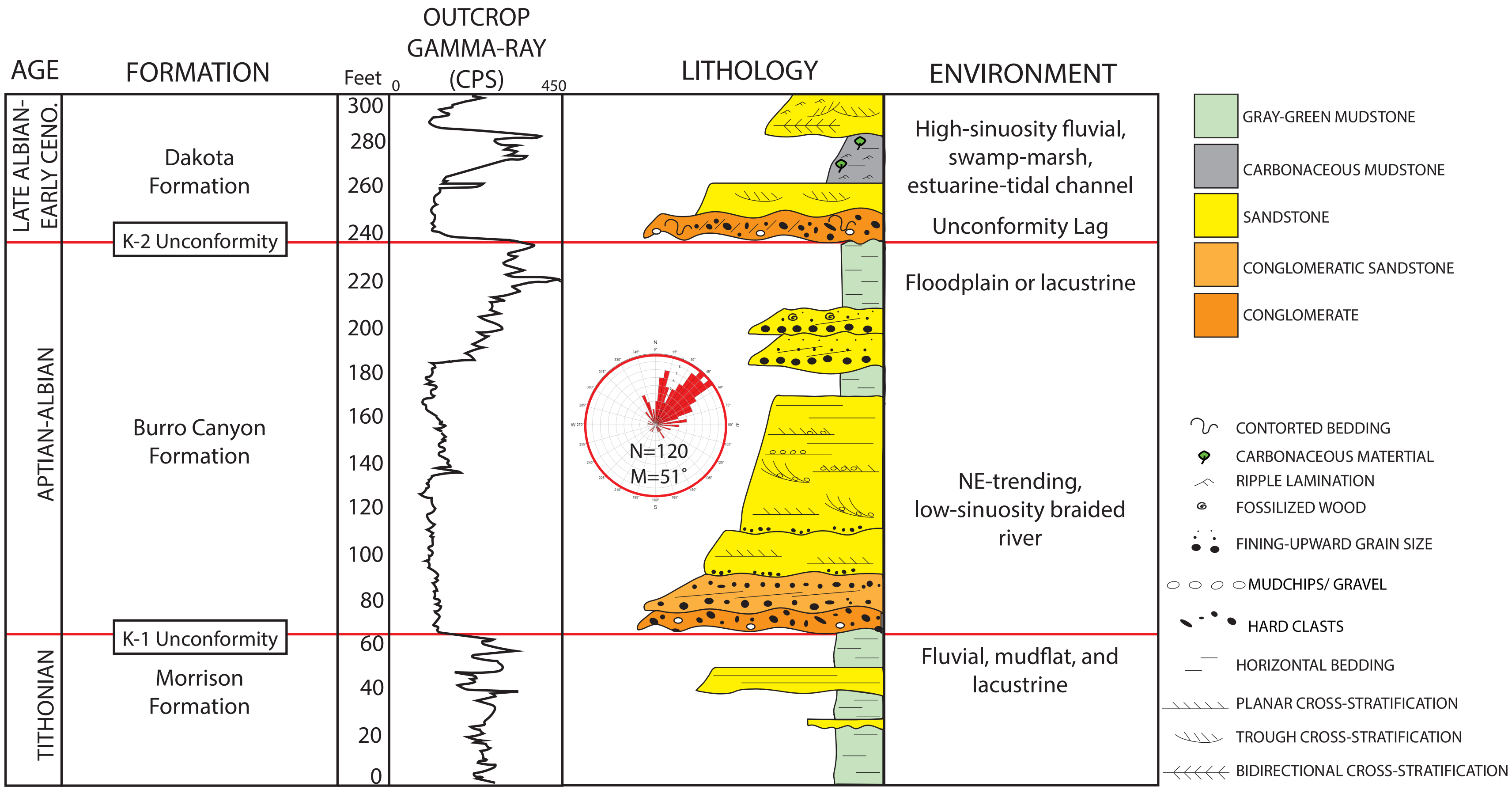

Figure 8. Composite stratigraphic section based on measured sections taken in Escalante Canyon. Outcrop gamma-ray increases from left to right and is merged from two traverses. The Burro Canyon Formation has a fining-upward character overall in the study area and contains high-energy, low-sinuosity to lower-energy, sinuous fluvial deposits with thick intervals of mudstone floodplain deposits.

internal heterogeneity (Figure 9; Appendix A). The Burro Canyon Formation in the study area forms a depositional sequence, which is composed of an amalgamated channel complex, formed by channel-fill elements which have amalgamated over time, overlain by a non-amalgamated channel complex, which contains smaller, disconnected channel-fill elements surrounded by floodplain facies (Figure 9). Patterson et al., (2010) defined the channel-fill element as a relatively conformable succession of genetically related bar or bar-set deposits within a channel defined by bankful discharge. The channel-fill element has a concave-up basal geometry and when preserved, is bounded on top by a transition from channel lithofacies (sandstone-dominated) to floodplain lithofacies (mudstone-dominated). Channel-top facies are commonly eroded during subsequent channel deposition owing to basal scouring that occurs in higher energy systems like the Burro Canyon Formation.

Four main facies associations that comprise the amalgamated and non-amalgamated channel complexes are described below using the naming convention of Patterson et al. (2002) (Figure 10).

Facies Association 1: amalgamated channel complex

The amalgamated channel complex consists of vertically stacked channel-fill elements and is the largest element in the Burro Canyon Formation (Figure 10). The typical facies sequence observed in the channel-fill elements is characterized by a scour surface along a concave-up channel-base and a conglomeratic lag deposit that transitions into a low-angle inclined cross-stratified conglomeratic sandstone which fines and thins upward. Graded beds are common in this lithofacies. Thick packages of

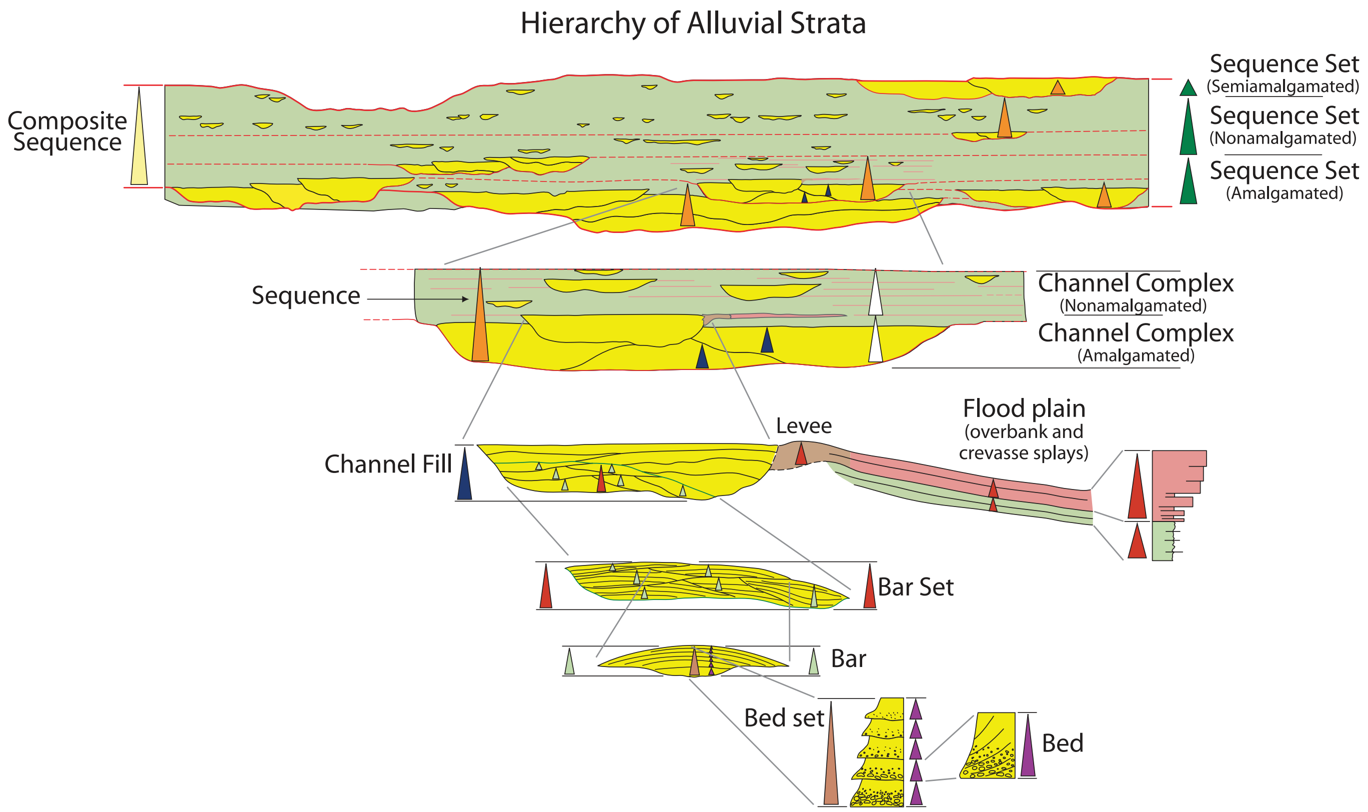

Figure 9. Idealized illustration of alluvial hierarchical elements. Channel sandstones are shown in yellow, floodplain mudstones are in green, levee sandstones are in brown, and crevasse splays are in pink. Red lines indicate sequence boundaries. Colored triangles are associated with each hierarchical element. The Burro Canyon Formation contains a channel complex sequence in Escalante Canyon and is composed of small- to intermediate-scale hierarchical elements such as beds and bedsets, bars and barsets, channel-fills, and channel complexes. See Appendix A for a full description of elements. From Patterson et al., 2010; modified from Sprague et al., 2002.

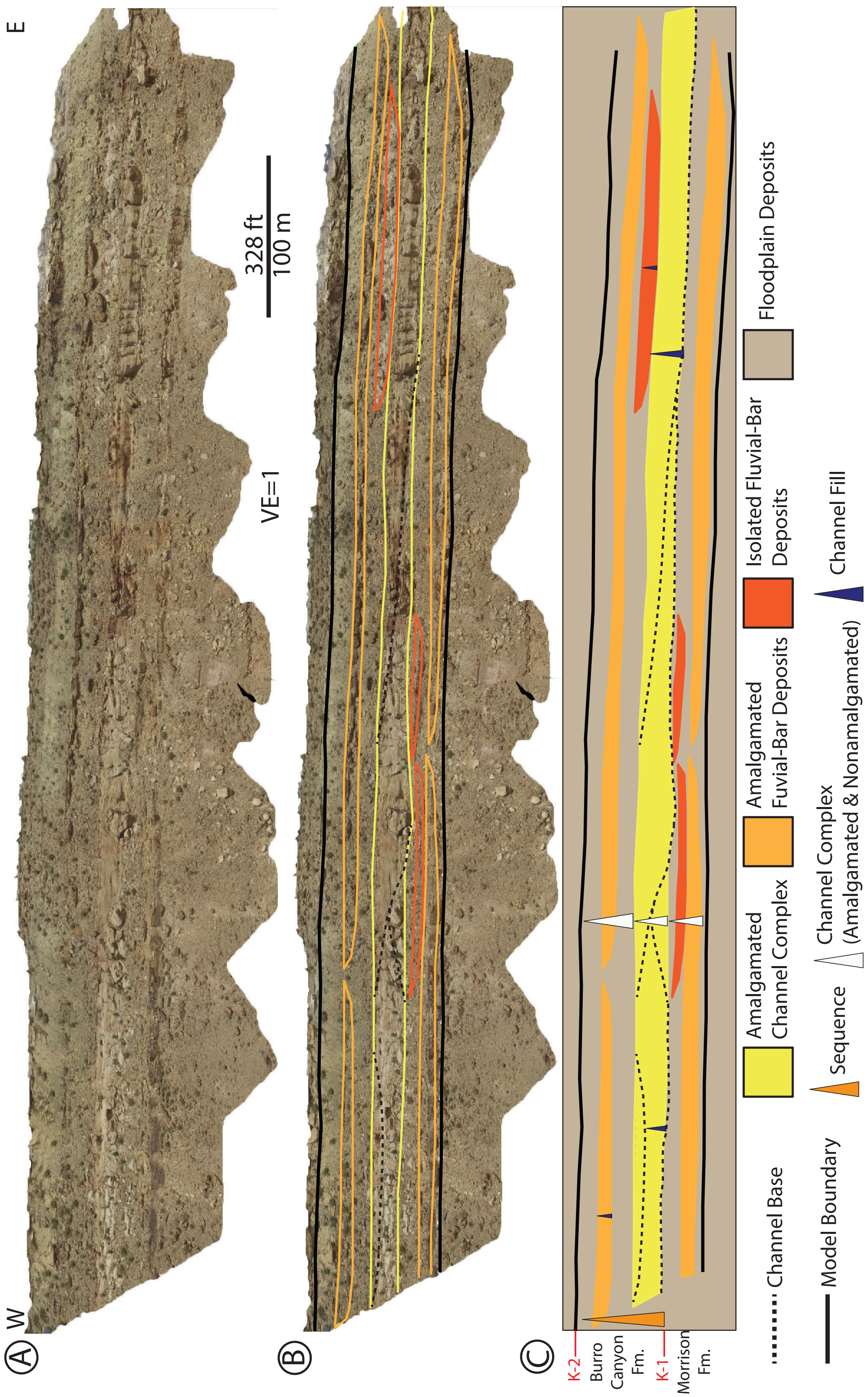

A
B
C
W
E
328 ft
100 m
VE=1
K-2
Burro Canyon Fm.
K-1
Morrison Fm.
Channel Base
Model Boundary
Amalgamated Channel Complex
Sequence
Channel Complex (Amalgamated & Nonamalgamated)
Amalgamated Fuvial-Bar Deposits
Isolated Fluvial-Bar Deposits
Channel Fill
Floodplain Deposits

Figure 10. (A) A UAV-based 3-D rendering of the southern exposure of Escalante Canyon with top and base of Burro Canyon interpreted in black. (B) Four facies associations are identified in the Burro Canyon Formation using UAV-based outcrop renderings. The facies associations and the hierarchical interpretation associated with them were used for populating outcrop reservoir models. (C) A diagrammatic representation of the facies associations and their hierarchical interpretations based on Patterson et al. (2002, 2010). Model boundaries are shown as black lines; the amalgamated channel complex (Facies Association 1) is shown in yellow with black dashed lines indicating channel bases; amalgamated fluvial-bar channel-fill deposits (Facies Association 2) are shown in light orange; isolated fluvial-bar channel-fill deposits (Facies Association 3) are shown in dark orange; and floodplain deposits (Facies Association 4) are shown in tan. Hierarchical elements are shown as triangles.

stacked sandy barsets are directly above the conglomeratic sandstone. The barsets exhibit a variety of stratification types such as tabular-planar and wedge-tangential cross-stratification, and less commonly horizontal planar bedding. Sandy cross-stratified bars tend to have erosional bases with limestone and quartzite clasts lining scour surfaces as gravel lag deposits. Channel-body tops, when preserved, transition from cross-stratified sandstone lithofacies (sandy barsets) to overbank mudstone facies (Walker and Cant, 1984). Channel tops are not preserved within the body of this architectural element because upper channels eroded into the tops of lower channels preventing overbank fines from being preserved. The channel-fill elements stack vertically and laterally to form amalgamated channel complexes which are thick and laterally extensive. The lateral extent of the amalgamated channel complex is larger than what is exposed in outcrop, but what is exposed is approximately 816 m (2677 ft) perpendicular to paleoflow orientation. The channel complex thickness is an average of 17.5 m (57 ft).

Facies Association 2: amalgamated fluvial-bar channel-fill deposits

Amalgamated fluvial-bar channel-fill deposits contain packages of sandstone with low-angle inclined cross-stratification to horizontal bedding. Sandstone beds fine-upward and commonly contain mudstone rip-up clasts along basal surfaces. Individual beds stack vertically to create barsets that comprise amalgamated fluvial-bar channel-fill deposits. These deposits are less laterally extensive than the amalgamated channel complexes of Facies Association 1 and are encased in floodplain mudstones. Together with Facies Association 3, they form a non-amalgamated channel complex (Figure 10).

This architectural element is on average 438 m (1437 ft) wide perpendicular to channel flow and 12 m (38 ft) thick.

Facies Association 3: isolated fluvial-bar channel-fill deposits

Isolated fluvial-bar channel fills are like amalgamated fluvial-bar channel fills in that they contain sandstones with low-angle inclined cross-stratification to horizontal bedding. Sandstone grain size decreases upward within individual beds and mudstone rip-up clasts are common along scour surfaces. Beds stack vertically to form fining-upward sandstone successions that compose the isolated fluvial-bar channel-fill deposits. Facies Association 3 is completely isolated and encompassed in floodplain mudstones and is much less laterally extensive than Facies Association 2 and together, they comprise non-amalgamated channel complexes (Figure 10). The isolated bar deposits measure on average 137 m (449 ft) wide perpendicular to channel flow and are 4 m (13 ft) thick.

Facies Association 4: floodplain deposits

Floodplain deposits are composed of mudstone facies, encase channel deposits, and have no discrete boundaries. Floodplain deposits are considered as non-reservoir rocks in this study.

Outcrop Reservoir Models

Lithofacies models

Three lithofacies model scenarios were constructed of the Burro Canyon Formation to explore different levels of heterogeneity within the fluvial deposits (Figure 11A-C). All non-reservoirs zones (Facies Association 4) were modeled as homogeneous mudstone facies in all model scenarios. The most simplistic reservoir scenario, Model 1, (Figure 11A) represents Facies Associations 1, 2, and 4 (amalgamated channel complex, amalgamated fluvial-bar channel fill, and floodplain) and only contains cross-stratified sandstone and gray-green mudstone facies. This model assumes there is no internal lithological heterogeneity in the reservoir bodies and is used as a base case for comparison to the more complex and geologically representative models. All Facies Associations (1-4) are included in Model 2 (Figure 11B) and the internal lithological heterogeneity of the main amalgamated channel complex is controlled by lithofacies logs to more accurately represent the lithofacies successions observed in outcrop. The most geologically representative model, Model 3, (Figure 11C) incorporates the channel-bar architecture within the amalgamated channel complex and the geometries associated with irregular channel-scour surfaces (channel basal surfaces) and associated facies. The channel-scour surfaces and the associated facies can impact fluid movement through the amalgamated channel complex.

Petrophysical models

Three-porosity and three-permeability models were constrained to the three different lithofacies model scenarios and variogram inputs (Figure 12). Model 1 porosity (Figure 12A) and permeability (Figure 12B) volumes are constrained by core-derived values for cross-stratified sandstone in the reservoir zones (Appendix C). As a

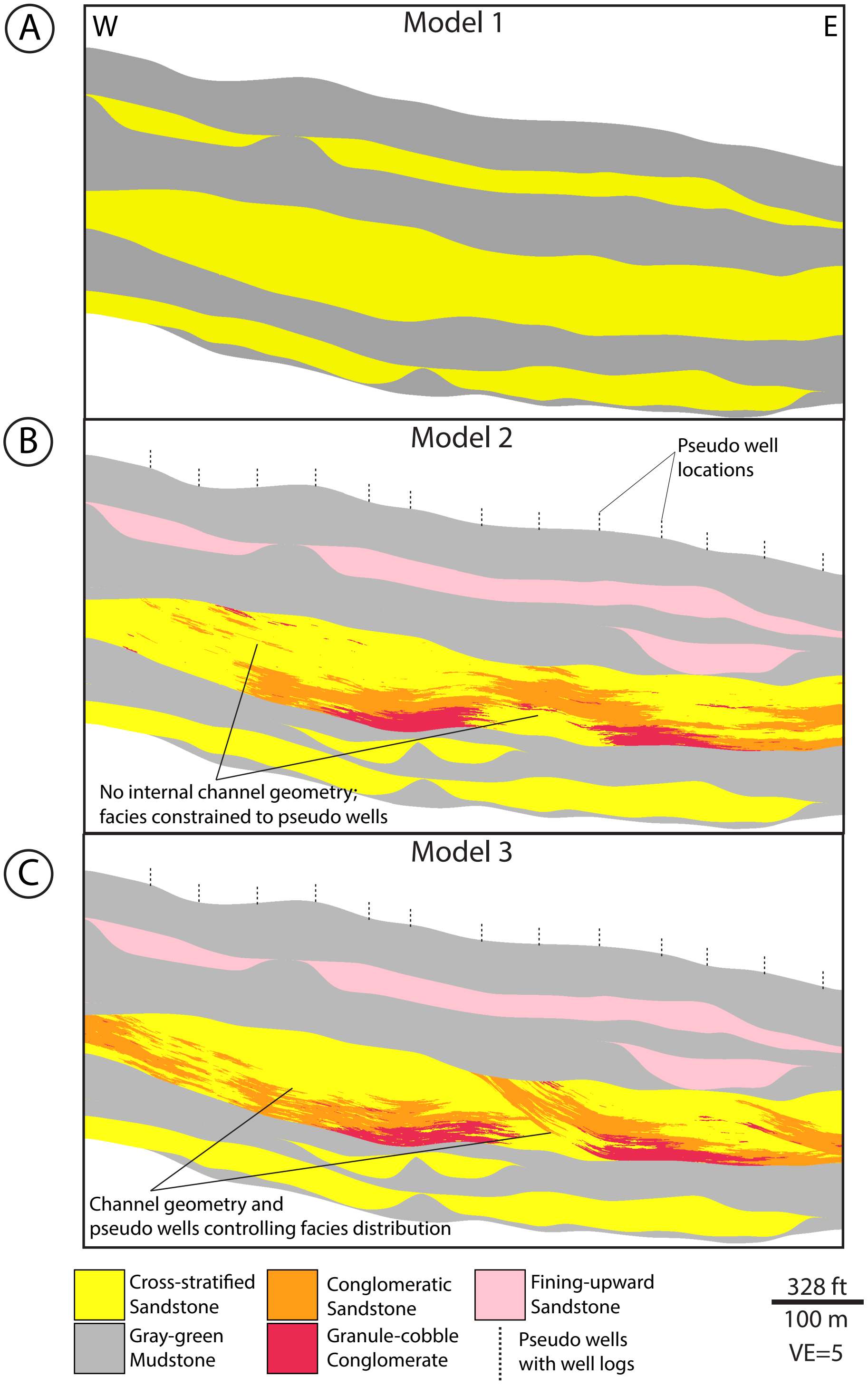
A
W
Model 1
E
B
Model 2
Pseudo well locations
No internal channel geometry; facies constrained to pseudo wells
C
Model 3
Channel geometry and pseudo wells controlling facies distribution
Cross-stratified Sandstone
Conglomeratic Sandstone
Fining-upward Sandstone
Gray-green Mudstone
Granule-cobble Conglomerate
Pseudo wells with well logs
328 ft
100 m
VE=5

Figure 11. Lithofacies models were created for each model scenario (1-3) (A, B, C) of the southern exposure of the Burro Canyon Formation in Escalante Canyon. There is increasing complexity included in each succeeding model to assess the impact of internal heterogeneity and sandstone-body connectivity on fluid-flow analysis. (A) Model 1 contains only cross-stratified sandstone and mudstone and only amalgamated architectural elements. (B) Model 2 includes all facies associations and key lithofacies seen in the Burro Canyon Formation. (C) Model 3 introduces channel-bases within the amalgamated channel complex in the middle of the model. Pseudo wells with lithofacies logs that were used to constrain Models 2 and 3 are shown as black dashed lines.

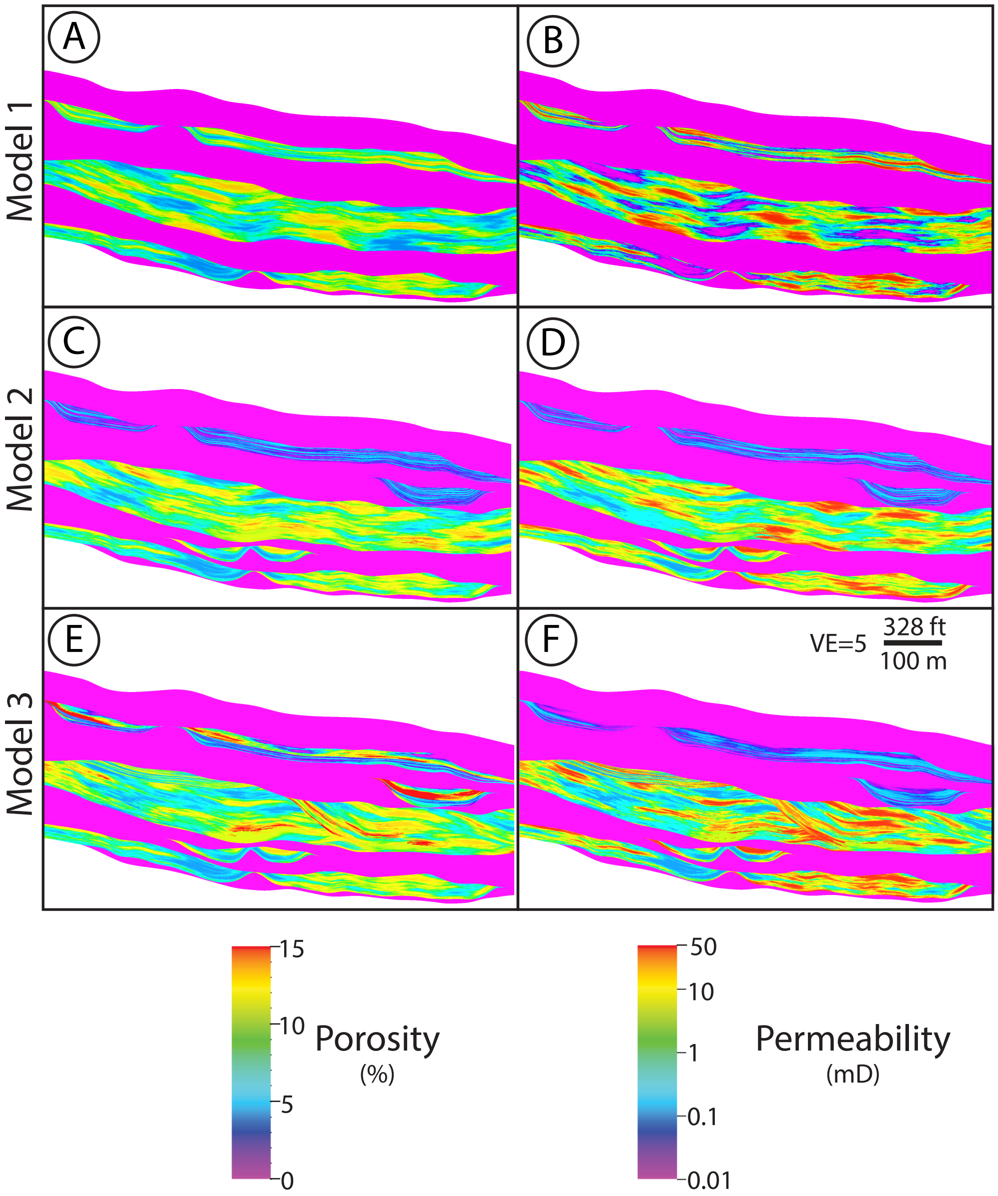
A
B
C
D
E
F
Model 1
Model 2
Model 3
VE=5
328 ft
100 m
15
10
5
0
Porosity
(%)
50
10
1
0.1
0.01
Permeability
(mD)

Figure 12. Porosity and permeability models were created for each model scenario (1-3) on the southern exposure of the Burro Canyon Formation. All models used porosity and permeability data from the Mitchel Energy 8-1 Federal core and were constrained to their associated lithofacies model. (A) Model 1 is populated with porosity and permeability data associated with cross-stratified sandstone. (B) Model 2 utilizes porosity and permeability data for all lithofacies modeled in the scenario. (C) Model 3 introduces decreasing-upward porosity trends associated with fining-upward sandstones and conglomeratic sandstones. In all scenarios, all non-reservoir zones (mudstone lithofacies) were set to 0% porosity and 0 mD permeability.

result, the upper reservoir zones contain much higher porosity and permeability values than in Models 2 (Figure 12C; D) and 3 (Figure 12E; F), where the upper zones are populated with fining-upward sandstone petrophysical values which are lower than those of the cross-stratified sandstone lithofacies (Appendix C). The main amalgamated channel complex in Model 1 has more variation in petrophysical values than in Models 2 and 3. This is because the entire zone is populated with one lithofacies that has a wider range of values in Model 1 (Figure 11A). Whereas Models 2 (Figure 11B) and 3 (Figure 11C) incorporate three lithofacies in that zone and are constrained by each of their coinciding petrophysical values which have less variability overall than the cross-stratified sandstone in Model 1. In the porosity and permeability volumes for Model 1, there are larger patches of values than in the other models because they are not constrained to lithofacies well logs. Model 3 contains channel bounding surfaces that control the orientation of lithofacies distributions within the amalgamated channel complex which in turn controls the directionality of petrophysical values. In Model 2, variograms alone are constraining the distribution of porosity and permeability values in the amalgamated channel complex.

Impact of Heterogeneity on Flow

Twenty-seven dynamic fluid-flow simulations were performed to investigate how lithofacies and petrophysical property variations within fluvial deposits impact reservoir performance. Porosity and permeability models conditioned to lithofacies models were used to conduct fluid-flow simulations for each of the three lithofacies heterogeneity scenarios.

Floodplain mudstones are the most important barriers to flow preventing fluid communication from upper and lower reservoir zones to the amalgamated channel complex. The upper reservoir zones (Facies Associations 2 and 3) show that lithofacies and petrophysical trends are important even in isolated reservoirs that are not connected to the injector well. The upper reservoir zones in Model 1 have cross-stratified sandstone with higher porosity and permeability than the upward-fining sandstones in the same reservoir zones of Models 2 and 3 (Figure 12; Appendix C). Therefore, cumulative oil and gas production from these deposits is greater in Model 1 than in Models 2 and 3, with Model 3 having the lowest cumulative production (Figure 13; Table 4). Overall, there is a 0.5% decrease in cumulative oil production for the lowest producing simulation, 8x8H-grid, from Model 1 to Model 3 and a 7% decrease for the highest producing simulations, 2x2U-grid for Model 1 and 8x8U-grid for Model 3. There is a 7% and 11% decrease in lowest and highest cumulative gas production, respectively, from Model 1 to Model 3.

The degree of fingering, defined as a preferential channeling of fluids (*sensu* Willhite, 1986), varies between the three model scenarios. In Model 1, reservoir zones are all assigned cross-stratified sandstone and associated petrophysical properties. This creates a more homogeneous reservoir than in Models 2 and 3 where multiple lithofacies are included. Conglomerates have lower petrophysical properties than cross-stratified sandstones; thus, creating areas of lower reservoir-quality rock. In addition, fluid flows along pathways in Model 3 differently owing to the directionality of lithofacies associations within the amalgamated channel complex. The irregular basal scour surfaces of channel deposits in the complex change the orientation and

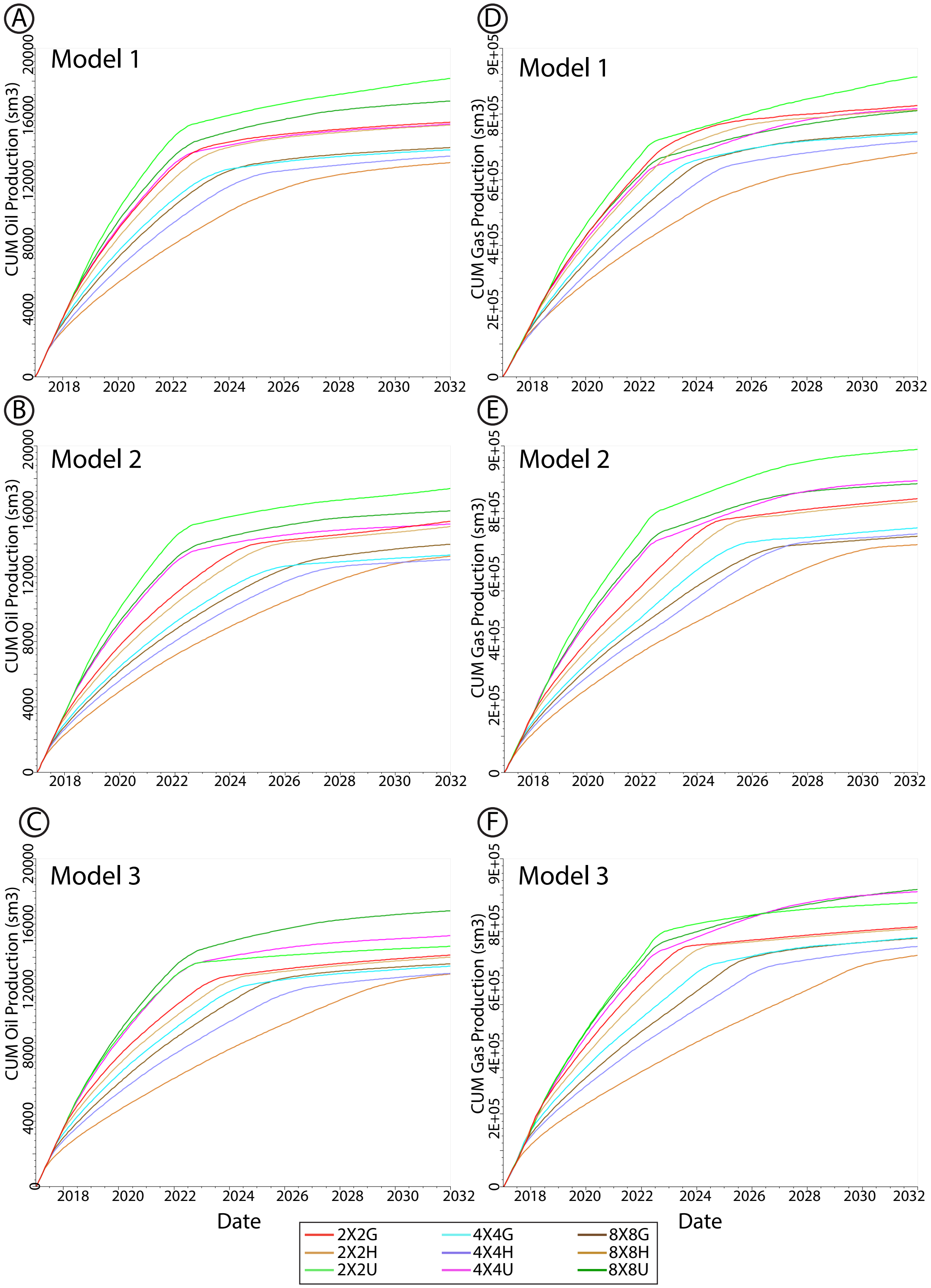
A
Model 1
CUM Oil Production (sm3)
0
4000
8000
12000
16000
20000
2018
2020
2022
2024
2026
2028
2030
2032
D
Model 1
CUM Gas Production (sm3)
0
2E+05
4E+05
6E+05
8E+05
9E+05
B
Model 2
C
Model 3
E
Model 2
F
Model 3
Date
Date
2X2G
2X2H
2X2U
4X4G
4X4H
4X4U
8X8G
8X8H
8X8U

Figure 13. Cumulative oil and gas production graphs are produced after all fluid-flow simulations for (A, D) Model 1 simulations, (B, E) Model 2 simulations, and (C, F) Model 3 simulations. The upper reservoir zones in Model 1 have cross-stratified sandstone which consists of higher porosity and permeability than the fining upward sandstones of Models 2 and 3. The cumulative oil production from these deposits is greater in Model 1 than in Models 2 and 3, with Model 3 having the lowest cumulative production owing to the fining-upward sandstones that exhibit lower reservoir quality. Model 1 simulations produced 13000 sm3 (82000 bbl) to 18200 sm3 (114000 bbl) oil (39% increase) compared to Model 2 simulations which produced 13000 sm3 (82000 bbl) to 17400 sm3 (110000 bbl) oil (33% increase) and Model 3 simulations which produced 13000 sm3 (82000 bbl) to 16800 sm3 (106000 bbl) oil (29% increase). Overall, this represents a 0.5% decrease in cumulative oil production for the lowest producing simulation, 8x8H-grid, from Model 1 to Model 3 and a 7.3% decrease for the highest producing simulations, 2x2U-grid for Model 1 and 8x8U-grid for Model 3. Cumulative gas production is greater in Model 1 than in Models 2 and 3. Model 1 simulations produced 682000 sm3 (429000 bbl) to 914000 sm3 (5751000 bbl) gas (34% increase); Model 2 simulations produced 629000 sm3 (3956000 bbl) to 891000 sm3 (5605000 bbl) gas (41% increase); and Model 3 simulations produced 635000 sm3 (3993000 bbl) to 816000 sm3 (5135000 bbl) gas (28% increase). There is a 6.9% and 10.7% decrease in lowest and highest cumulative gas production, respectively, from Model 1 to Model 3.

A

Model Name	Cumulative Oil Production	Percent Change
Model 1	13000 sm^3 - 18200 sm^3 (82000 bbl - 114000 bbl)	39%
Model 2	13000 sm^3 - 17400 sm^3 (82000 bbl - 110000 bbl)	33%
Model 3	13000 sm^3 - 16800 sm^3 (82000 bbl - 106000 bbl)	29%

B

Model Name	Cumulative Gas Production	Percent Change
Model 1	682000 sm^3 - 914000 sm^3 (429000 bbl - 5751000 bbl)	34%
Model 2	629000 sm^3 - 891000 sm^3 (3956000 bbl - 5605000 bbl)	41%
Model 3	635000 sm^3 - 816000 sm^3 (3993000 bbl - 5135000 bbl)	28%

Table 4. Summary of (A) cumulative oil production and (B) cumulative gas production ranges in model scenarios 1, 2, and 3. Cumulative oil and gas is greatest in Model 1 scenarios and lowest in Model 3 scenarios. Model 1 also has the greatest range of cumulative production (39% change from least to greatest oil production and 34% change in gas production), while Model 3 has the lowest range of cumulative production (29% change in oil production and 28% in gas production).

distribution of high porosity and permeability lithofacies such that the injected water follows the curvature of the channel-fill elements (Figure 14).

Model 1 flow simulations have BTT ranging from 67 months for the 2x2G-grid (2 m x 2 m- Geometric mean upscaling) to 95 months in the 4x4H-grid with an average of 81 months. Model 2 grids generally show the longest BTT ranging from 94 months in the 2x2H-grid to 147 months in the 8x8H-grid with an average of 108 months, representing a 34% increase in average BTT from the lowest BTT seen in Model 1 (Figure 14; 15; Appendix D). Model 3 BTT ranges from 79 months in the 2x2G-grid to 161 months in the 8x8H-grid with an average of 106 months. Even though Model 3 is the most heterogeneous scenario, the simulations do not have the longest BTT. The irregular basal-scour surfaces of the channels juxtapose high porosity and permeability lithofacies against each other, thus creating pathways for fluids to flow across the amalgamated channel complex to the producing well with reduced BTT. In contrast, Model 2 has an area of low porosity and permeability in the center of the amalgamated channel complex that reduces fluid flow in the simulations (Figure 16).

Recovery efficiency for oil is the ratio of the cumulative amount of oil produced for a specified period of time divided by the amount of oil initially in place. Recovery efficiency is calculated at BTT and also at the end of the 15-year simulation period (Figure 17B, D, F). Generally, recovery efficiencies at the end of the simulation period are very similar between model scenarios, grid sizes, and upscaling methods. Recovery efficiencies at 15 years for Model 1 simulations range from 46.6% to 49.9% (48.6% average); Model 2 simulations range from 46.2% to 50.2% (48.1% average); and Model 3 simulations range from 41.2% to 44.2% (42.3% average); representing about a 13%

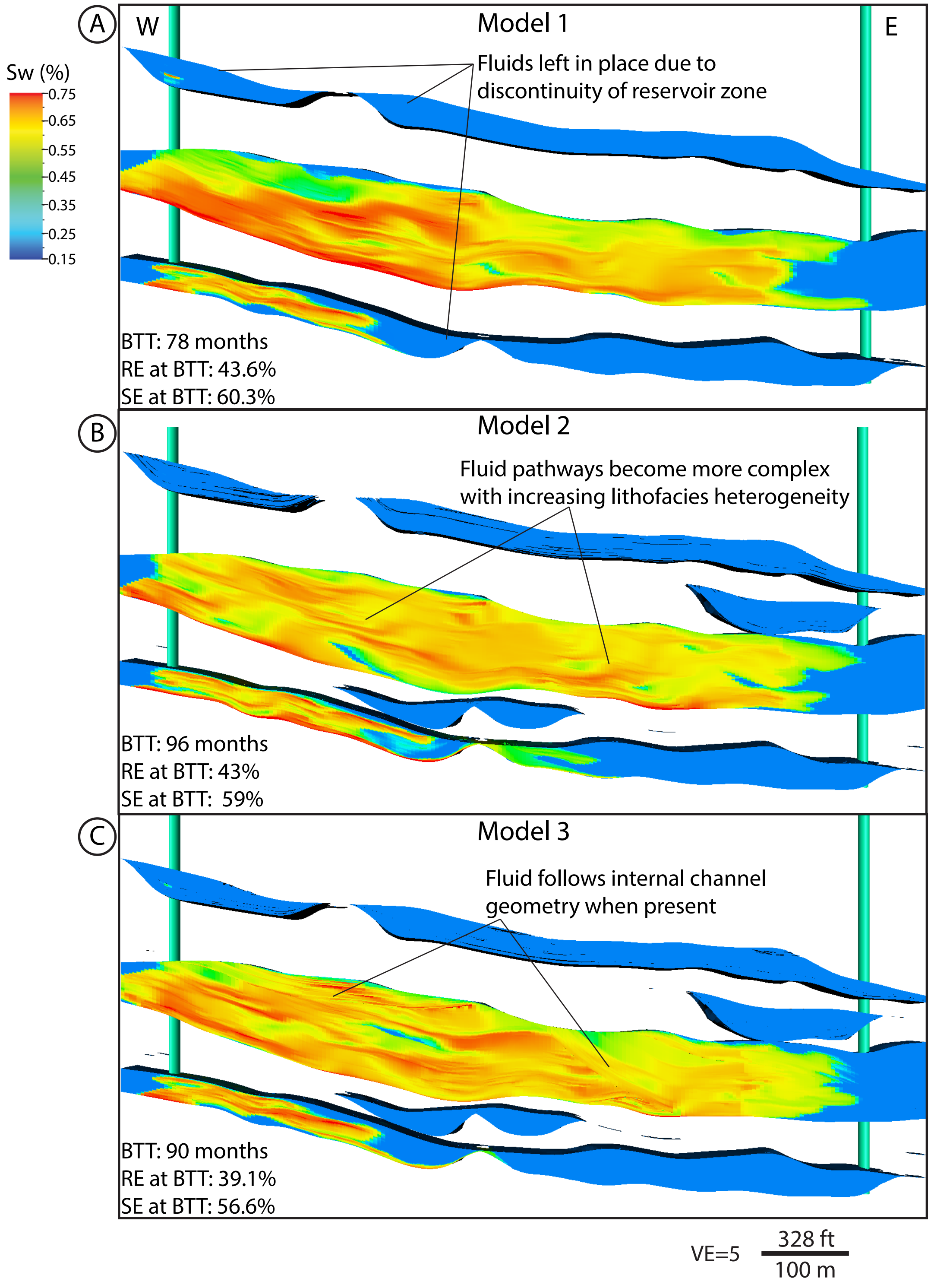
A
W
Model 1
E
Sw (%)
0.75
0.65
0.55
0.45
0.35
0.25
0.15
Fluids left in place due to discontinuity of reservoir zone
BTT: 78 months
RE at BTT: 43.6%
SE at BTT: 60.3%
B
Model 2
Fluid pathways become more complex with increasing lithofacies heterogeneity
BTT: 96 months
RE at BTT: 43%
SE at BTT: 59%
C
Model 3
Fluid follows internal channel geometry when present
BTT: 90 months
RE at BTT: 39.1%
SE at BTT: 56.6%
VE=5
328 ft
100 m

Figure 14. Water saturation models at BTT for 4x4G-grids (upscaled with the geometric mean) in all model scenarios (Model 1-3) (A-C). BTT, recovery efficiency (RE at BTT), and sweep efficiency (SE at BTT) are indicated below each model. Where reservoir zones are disconnected and only penetrated by either the injector or producer well as in the upper and lower zones of Burro Canyon Formation, fluids are left in place and recovery efficiencies are lower than if they were better connected. BTT is fastest in (A) Model 1 scenarios (67-95 months) and slowest in (B) Model 2 scenarios (94-147 months). Recovery efficiency decreases with increased heterogeneity and model complexity where there are more pockets of isolated, lower reservoir quality rocks. Recovery efficiency ranges from 46.65% to 49.93% for Model 1, 46.25% to 50.20% for Model 2, and 41.22% to 44.18% for Model 3 simulations.

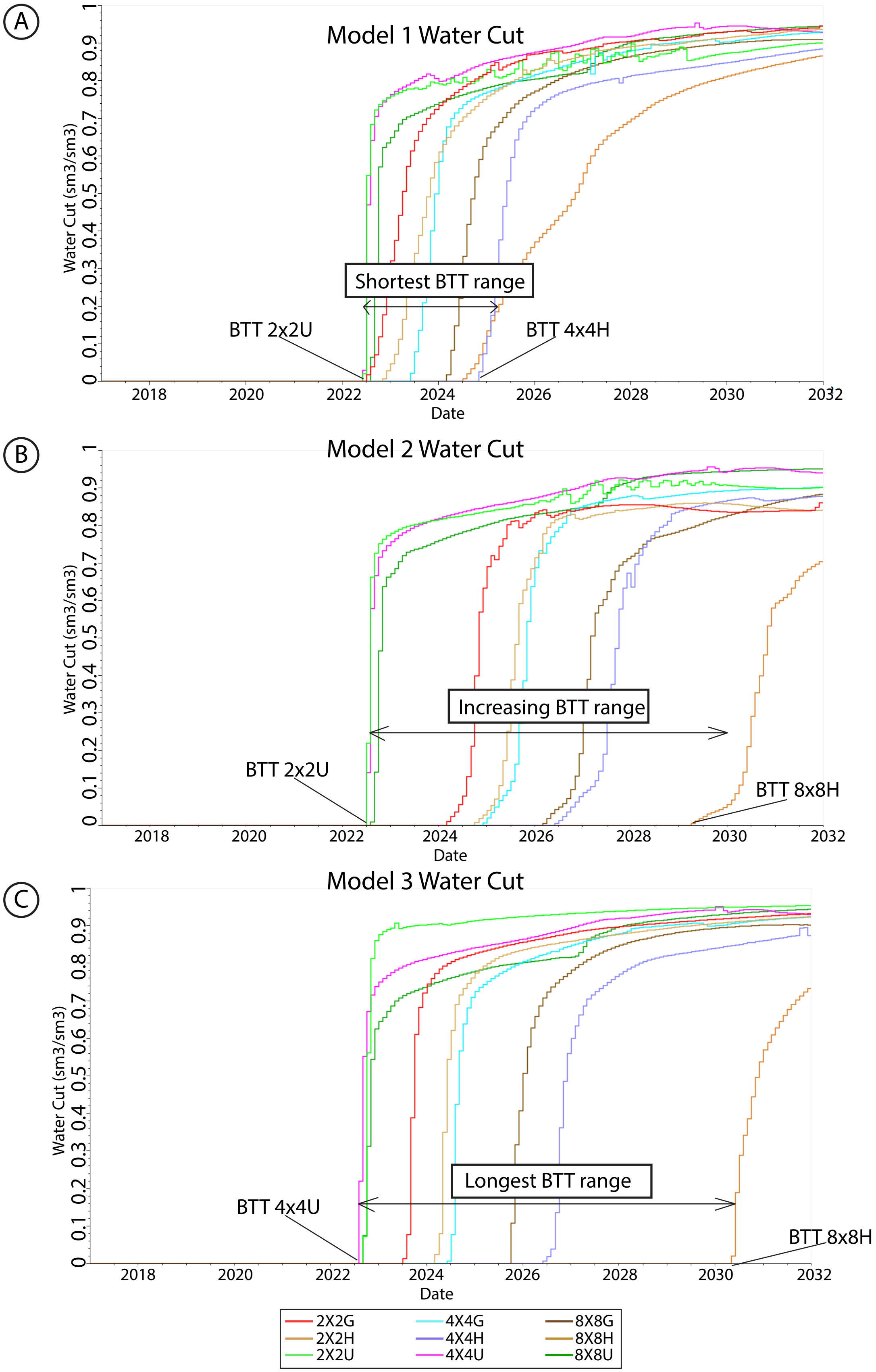
A
Model 1 Water Cut
Water Cut (sm3/sm3)
0
0.1
0.2
0.3
0.4
0.5
0.6
0.7
0.8
0.9
1
Shortest BTT range
BTT 2x2U
BTT 4x4H
2018
2020
2022
2024
2026
2028
2030
2032
Date
B
Model 2 Water Cut
Water Cut (sm3/sm3)
Increasing BTT range
BTT 2x2U
BTT 8x8H
Date
C
Model 3 Water Cut
Water Cut (sm3/sm3)
Longest BTT range
BTT 4x4U
BTT 8x8H
Date
2X2G
2X2H
2X2U
4X4G
4X4H
4X4U
8X8G
8X8H
8X8U

Figure 15. Water cut graphs are shown to indicate BTT for (A) Model 1 simulations, (B) Model 2 simulations, and (C) Model 3 simulations. Model 1 simulations display the shortest BTT (average 81 months), while Model 2 simulations show the longest (average 147 months). The uniform property model simulations have the shortest BTT in all model scenarios (66-69 months). Simulations containing permeability models upscaled using the harmonic mean generally have longer BTT than those using the geometric mean owing to the preservation of higher permeability values in the latter models. 8x8-grid simulations typically display longer BTT (average 117 months) than finer resolution grids (2x2-grids average 82 months). As grid size increases, pathways of small but connected high porosity and permeability values decrease forcing fluid to move through larger zones of poorer-quality rock. Therefore, the fluid has an easier time 'finding' a pathway to flow through in the smaller grid sizes.

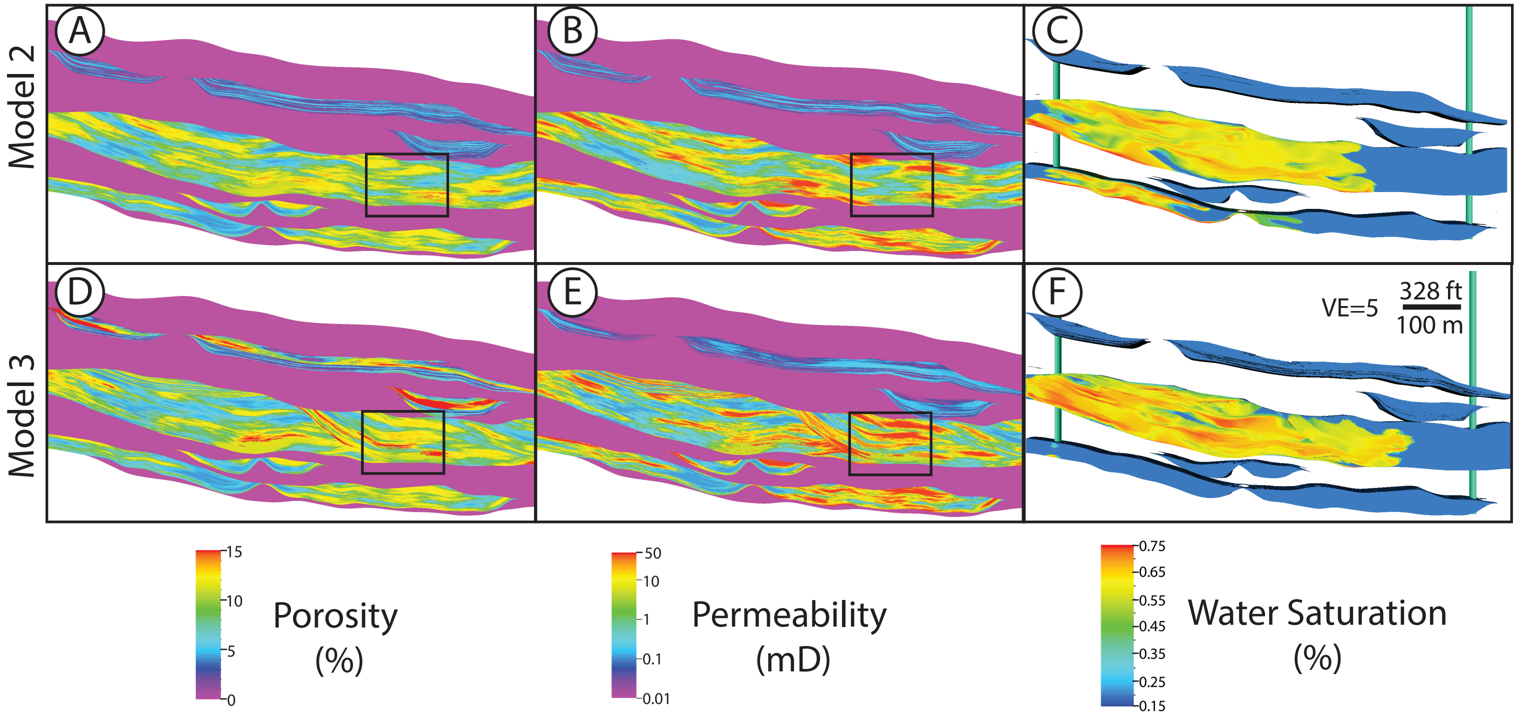

Figure 16. Example of the effect of increased internal heterogeneity on BTT. Model 2 contains a larger area of lower porosity (A) and permeability (B) which slows fluid movement through the second half of the model (C) causing a longer BTT compared to Model 3 which has channel-bases that align facies with higher porosity (D) and permeability (E) values allowing fluid to flow faster through the same section of the model (F) causing a lower BTT. Black boxes indicate areas of petrophysical variation in the models. Model grids-2x2H are shown as an example of this effect.

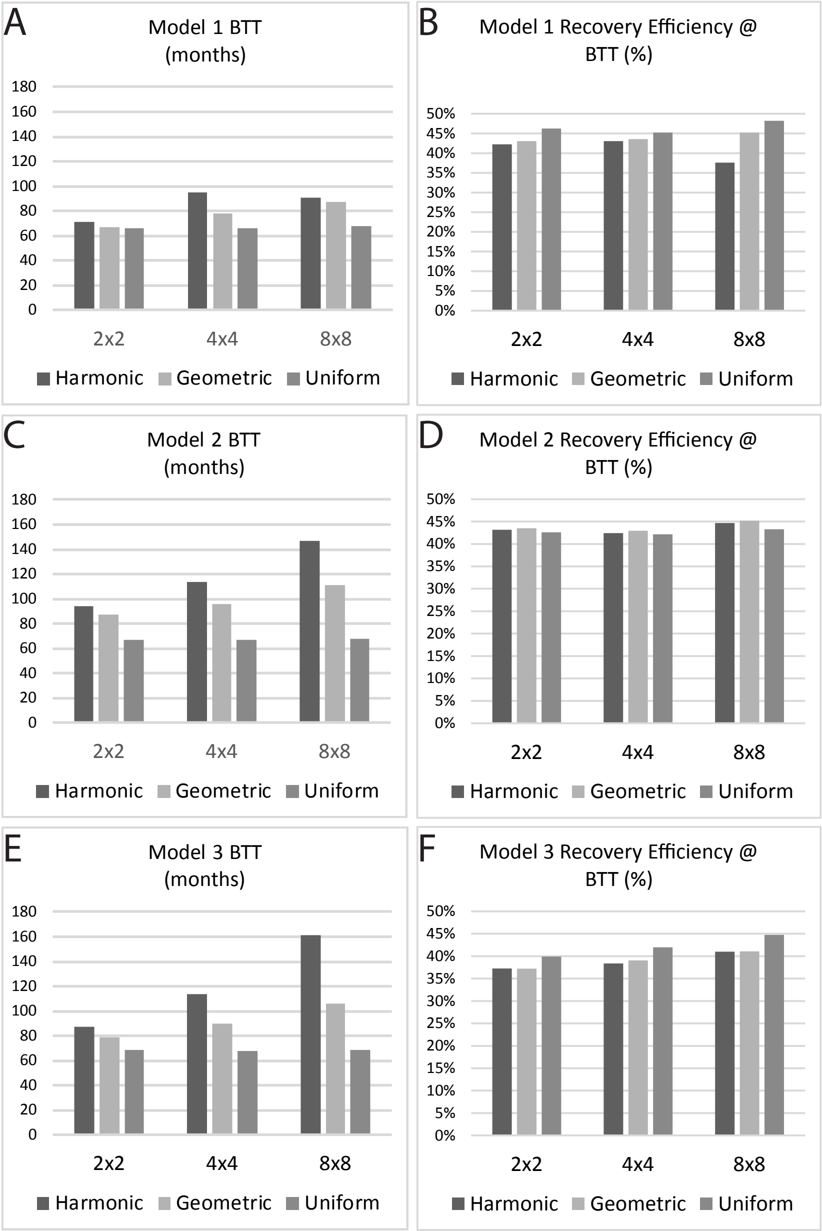

Figure 17. Histograms of fluid-flow simulation results for all model scenarios (1-3), grid sizes, and upscaling methods. Model 1 BTT (in months) (A) and recovery efficiency at BTT (%); Model 2 BTT (C) and recovery efficiency (D); and Model 3 BTT (E)) and recovery efficiency (F). Grid size is in meters and indicated by 2x2, 4x4, and 8x8. Simulations that contained permeability models that were upscaled using the harmonic mean are in dark gray; geometric mean are in light grey, and uniform-petrophysical models are in medium grey.

decrease in average recovery efficiency from Models 1 to 3. The lower recovery efficiency of Model 3 is owing to less water injection into the lower reservoir zones (amalgamated fluvial-bar channel-fill deposits). At BTT, recovery efficiency is also lower in Model 3 scenarios ranging from 37.2% to 41% (39% average) as compared to Model 1: 37.6% to 45.2% (42.4% average), and Model 2: 42.4% to 45.2% (43.6% average). Model 3 has ~10% lower recovery efficiency as compared to Models 2.

Volumetric sweep efficiency is calculated at BTT and is defined as the volume of reservoir contacted by the injected water at a specified time divided by the total volume of reservoir. To calculate sweep efficiency in this study, cells with water injection greater than connate water saturation at BTT were identified, and the sum of the volume of these cells was divided by the total cell volume of reservoir in the model. On average, Model 1 simulations display higher volumetric sweep efficiency (61%) than Model 2 (60.8%) and Model 3 (56.2%), representing a 7.8% decrease from Model 1 to 3. Sweep efficiency ranges from 53.6% to 69.2% in Model 1; 58.7% to 62.5% in Model 2; and 52.2% to 60.8% in Model 3. Similar to recovery efficiency, lower sweep efficiency of Model 3 is owing to less water injection into the lower reservoir zones and a more tortuous path for water flow owing to the irregular basal-scour surfaces of the channels in the amalgamated channel complex.

Impact of Upscaling on Flow

As aerial cell size increases, the character of fluid fingering changes. In the 2x2-grids, flow pathways are finer, while with larger cells, pathways become broader and tend to become more dispersed (Figure 18). Uniform property model simulations

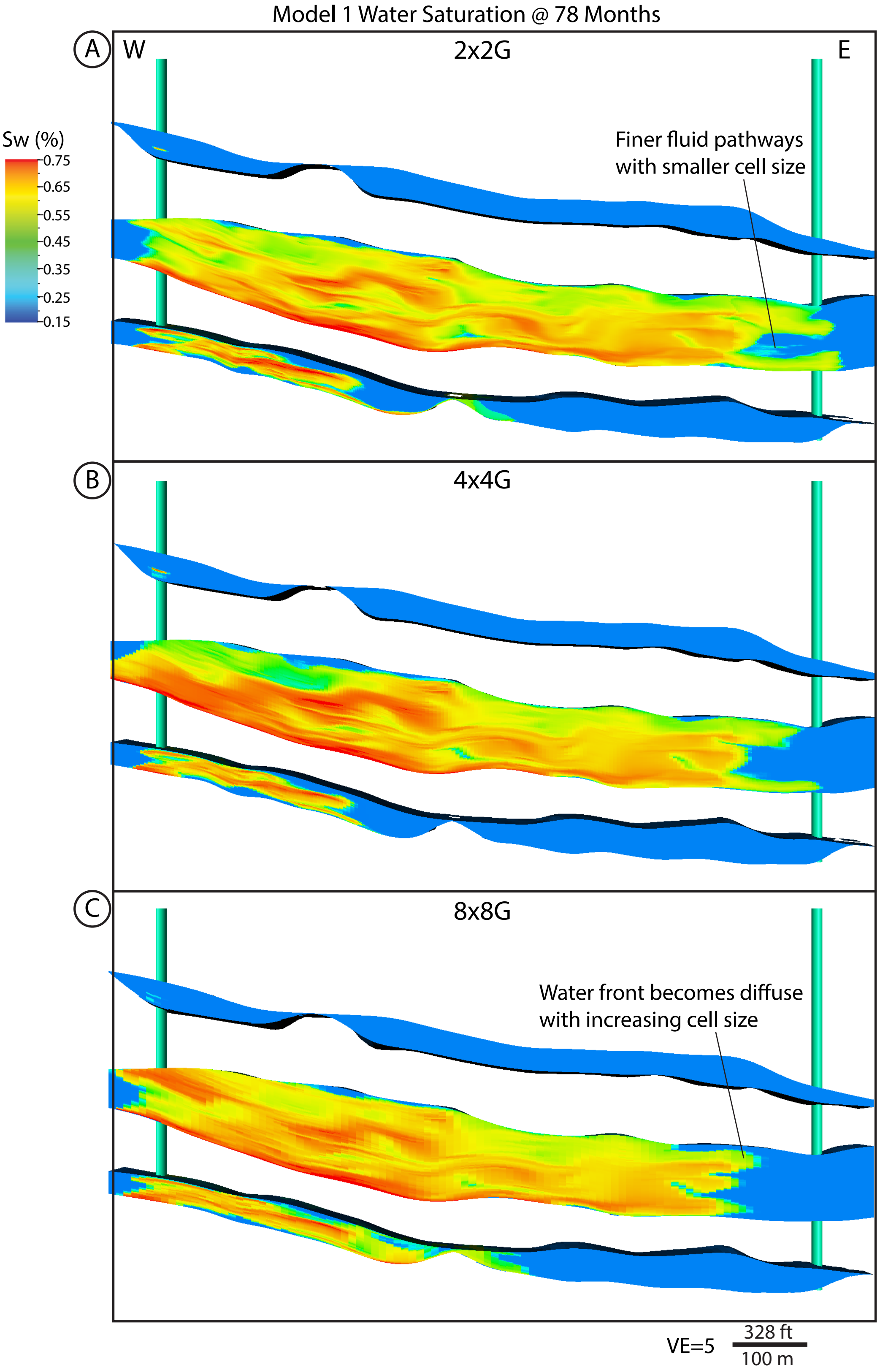
Model 1 Water Saturation @ 78 Months

Finer fluid pathways with smaller cell size

Water front becomes diffuse with increasing cell size

Figure 18. Water saturation models for the Model 1 scenario are shown with the (A) 2x2-, (B) 4x4-, and (C) 8x8-grid sizes to illustrate the effect of increasing cell size on the degree and character of fluid fingering. Fluid pathways are finer in the 2x2-grid simulations (A), whereas the water front increasingly becomes more diffuse and dispersed with increasing cell sizes (B; C).

(models with a single value for porosity and permeability assigned to all reservoir zones) show a piston-like water front movement across the amalgamated channel complex (Appendix D).

Simulations performed with 2x2-grids (2 m x 2 m; 6.5 ft x 6.5 ft) typically have the shortest BTT ranging from 67 to 94 months with an average of 82 months and those with 8x8-grids (8 m x 8 m; 26.2 ft x 26.2 ft) show the longest BTT from 87 to 161 months with an average of 117 months; a 42% increase in average BTT. As grid size increases, pathways of small but connected high porosity and permeability values decrease forcing fluid to move through larger zones of lower quality rock; essentially the fluid has an easier time ‘finding’ a pathway to flow through with the smaller grid sizes. Uniform property model simulations for all model scenarios and grid sizes have very similar BTT ranging from 66 to 69 months. Models using the harmonic mean for upscaling permeability show 17% shorter BTT than models using the geometric mean. This is likely owing to the geometric mean preserving higher ranges of permeability than the harmonic mean (Appendix C).

The highest recovery efficiencies at BTT and at the end of the 15-year simulation period are observed in the 8x8-grid simulations. At BTT, recovery efficiency for the 8x8-grids ranges from 37.5% to 45.2% (42.4% average) and after 15 years ranges from 42.1% to 50.2% (46.7% average). While the lowest recovery efficiencies are observed for the 2x2-grid simulations (41% average) at BTT and the 4x4-grid simulations (45.7% average) at the end of 15 years. This represents a 3.2% decrease in recovery efficiency from the 8x8-grids to the 2x2-grids at BTT and a 2.2% decrease after 15 years between the 8x8-grids and the 4x4-grids. Higher recovery efficiencies are observed in the 8x8-grid simulations. Smaller cell sizes in the 2x2- and 4x4-grid scenarios create pockets of lower quality rock that are disconnected from higher quality rock, retaining the fluids in place. Whereas with larger cell sizes, it is more likely that a single cell will be in contact with a high-quality rock in some degree. Therefore, making it possible for injected water to flow more easily through connected pathways of high reservoir quality rock. Models that were upscaled using the geometric mean show higher recovery efficiencies than those upscaled with a harmonic mean. This is consistent with the geometric mean preserving higher ranges of permeability values than the harmonic mean, allowing for more fluids to be extracted from the higher quality rocks. At BTT, models upscaled using a geometric versus harmonic mean have an average recovery efficiency of 42.3% versus 41%, respectively; representing a 2.9% decrease. After 15 years, these same models have average recovery efficiencies of 47.1% and 45.6%, respectively; representing a 3.1% decrease.

Volumetric sweep efficiency displays similar results to recovery efficiency where grids with larger cell sizes have higher sweep efficiencies. Simulations using the 8x8-grids have a sweep efficiency range from 54.6% to 69.2% with an average of 62.7%; 4x4-grids range from 53.5% to 62.5% with an average of 58.8%; and 2x2-grids have the lowest recovery efficiencies with a range from 52.2% to 60.4% and an average of 56.8%. This represents an average decrease of 9.3% from the 8x8-grids to 2x2-grids. Models that were upscaled using the geometric mean display higher recovery efficiencies than those based on the harmonic mean with average recovery efficiencies of 59.4% and 53.3%, respectively. This represents a 10.4% decrease owing to higher permeability values preserved when the geometric mean is used for upscaling.

DISCUSSION

Environment of Deposition

The lower Burro Canyon Formation represents a low-sinuosity braided fluvial environment and grades into a sinuous fluvial environment in the upper portion of the formation. Although there is not an established facies model for braided fluvial environments (Walker and Cant, 1984), there have been important studies of ancient braided river deposits which show their facies diversity (Moody-Stewart, 1966; Kelling, 1968; Conaghan and Jones, 1975; Campbell, 1976; Cant and Walker, 1976; Miall, 1977b; Allen, 1983; Haszeldine, 1983). However, idealized vertical sections from these studies, such as Miall's (1977a, 1977c) proposed South Saskatchewan type, exhibit common trends in deposits that are also observed in the Burro Canyon Formation (Figure 8). As discussed previously, channel-top or vertical-accretion deposits tend to be fine-grained sandstones and claystones that overlie in-channel sandstones and are rarely preserved in braided-channel deposits (Walker and Cant, 1984). These fine-grained deposits are absent in this outcrop and their scarcity in relation to the amount of in-channel sandstone supports the interpretation that the formation represents braided-fluvial deposits (Walker and Cant, 1984). Channel-floor coarse-grained lag deposits overlying scour surfaces are common in this environment at the base of the amalgamated channel complex (Miall, 1977b; Walker and Cant, 1984; Nichols, 2009). Several types of braid bars are present and identifiable by their stratification types (Table 5) (Miall, 1977a, 1977b). These bars migrate and aggrade to create thick and highly variable complexes of cross-stratified sandstone (Appendix A). The cross-beds tend to fine and thin upward owing to the decreasing flow-strength as the bars build and

Bar Type	Stratification and Interpetation
Longitudinal	low-angle cross-stratification (also massive or crude horizontal bedding) in downstream direction; most commonly gravel bars; can coalesce downstream becoming several hundreds of meters in length; coarsest in central portion of bar and fine upwards and downstream; possibly deposited under very high flow energy; bounded by active channels on either side of bar; diamond- or lozenge-shaped in plan view; wedge-shaped sand units may build out on lee side of bars during waning flow periods
Linguoid and transverse	planar-tabular cross-stratification representing downstream-facing, avalanche slope, sinuous termination progradation in shallow channels; deeper channels can produce trough cross-bedding; commonly deposited in trains of bars (<300 m in length); transverse bars have straighter crests and may represent coalesced lingouid bars or solitary bars that extend across the channel; large scale bedforms probably generated during flood stages; lingouid and transverse bars are difficult to distinguish between in geologic record
Compound	internal stratification can include planar-tabular (linguoid) or trough (dune or scour) cross-stratification, ripple marks, lag deposits (chutes), and fine-grained drape and fill deposits (swales); fining-upward cycles are common; develop from coalescence of dune-type bars over periods of many years; lateral bars, side bars (point bars), and sand flats may develop; can be several kilometers in length; vertical and lateral accretion is very imortant and form in areas of relatively low fluvial energy; can be much larger scales than other bar types and tend to form from coalescence of smaller bedforms, such as dunes and linguoid bars
Cross channel	planar-tabular cross-bedding oblique to flow direction due to straight-crested bars at high-angle to channel trend; wedge-shaped cross-stratification common; may coalesce to form large sand flats

Table 5. Bar types and stratification recognized in the Burro Canyon Formation in Escalante Canyon. From Miall (1977a, 1977b) and Walker and Cant (1984).

the channel shallows (Nichols, 2009). The migration and amalgamation of in-channel sandstones results in laterally extensive sandstone sheets in braided-fluvial environments (Walker and Cant, 1984). Amalgamated channel deposits of the Burro Canyon Formation in the study area typically extend past the outcrop boundaries. Floodplain facies form thick mudstones between channels. They typically do not fully encase the channel sandstones laterally except for Architectural Element 3. Isolated channels are indicative of a lowering of system energy owing to decreasing accommodation space or decreasing sediment supply causing an increase in channel sinuosity and lower net-to-gross ratios in the Burro Canyon Formation through time.

Effect of Sandstone-Body Geometry and Internal Heterogeneity on Reservoir Performance

Within a fluvial reservoir, sandstone-body geometry varies laterally and vertically between amalgamated and isolated elements depending on energy of the depositional system. Facies associations 2 and 3 are often disconnected or in limited fluid communication with other reservoir bodies creating isolated to semi-isolated reservoir compartments which affects recovery efficiency. As observed in the reservoir models, it is possible for isolated reservoir bodies to be penetrated by either the injector or producer well, which impacts oil and gas recovery (Figure 14). It is important to consider these disconnected reservoirs for well planning and when interpreting well logs, where the lateral extents of sandstone bodies is difficult to ascertain. Recovery efficiency can be increased in fluvial reservoirs containing isolated sandstone bodies, if the appropriate well geometry or spacing is used to contact multiple reservoir compartments in low net-to-gross systems.

Internal facies and architectural element heterogeneity can be an important control on the degree and character of fluid fingering within the reservoir which affects recovery efficiency. Within the amalgamated channel complex (Architectural Element 1), the facies associations in Model 3 imposed by the channel geometry are the most important controls on fluid-flow pathways. The channel geometry aligns high porosity and permeability zones such that fluid is able to flow through these areas to the producing well faster than in the Model 2 scenario, (Figure 16). Model 3 scenarios have approximately 1.8% shorter BTT than Model 2 scenarios on average, however Model 3 scenarios showed a 10% decrease in average recovery efficiency at BTT and ~7.5% decrease in average volumetric sweep efficiency from Model 2 scenarios. This is largely owing to less injected water penetrating lower reservoirs in Model 3 scenarios, but also owing to Model 2 having less tortuous pathways for fluid to follow because it does not contain channel-bounding surfaces which direct flow through the models. As discussed previously, it is possible for mudstone-rich channel-top deposits to be preserved on sandy-bar deposits. Owing to their poor reservoir properties, these deposits could act as fluid baffles and control flow across the reservoir; thus, affecting recovery efficiency and BTT. In addition, the isolated reservoir compartments in the upper portions of Model 3 are populated with fining-upward sandstones and, owing to their low porosity and permeability, further prevent complete sweep of fluids through these bodies. So, it is very important when mapping fluvial reservoirs to accurately identify and correlate muddy channel-top (Robinson and McCabe, 1997) and fining-upward sandstone facies when present to ensure the most accurate predictions of fluid movement, recovery efficiency, and volumetric sweep efficiency.

The reservoir models used in the flow simulations in this study are considered two-dimensional and because of this, flow is examined in a perpendicular direction to original paleocurrent. Dodge et al. (1971) and Jones et al. (1987) showed that sandstones with unimodal cross-bedding dip, which are found in channel-fill elements of the Burro Canyon Formation, should have higher permeabilities parallel to depositional dip direction, and thus, parallel to paleoflow. Therefore, owing to the orientation of the 2-D models in this study, longer BTT and lower recovery efficiencies are expected than if the models were oriented parallel to the paleocurrent direction.

Implications of upscaling geological models

The most important factors when considering the degree of upscaling required to perform fluid-flow simulations are: the expected impact of small-scale heterogeneity on fluid flow; time available for simulation performance and computational power of computers available; and methods used for upscaling. Many times, small-scale features can impact fluid flow and are important variables in the modeling process that should not be left out owing to larger cell size. As seen in this study, grid resolution and upscaling method can have significant impacts on BTT. Increasing cell size results in longer average BTT by 40% when increasing cell size from 2 m x 2 m (6.5 ft x 6.5 ft) to 8 m x 8 m (26.2 ft x 26.2 ft), and a 17% increase in BTT is observed when the geometric mean is used to upscale permeability models compared to those using the harmonic mean. Volumetric sweep efficiency is decreased by 9% when cell size is decreased to a 2x2-grid scenario from an 8x8-grid scenario and shows an average of 10% decrease between scenarios using the geometric mean and those using the harmonic mean for upscaling model parameters. As Salazar and Villa (2007) reported, the degree of upscaling required is the critical factor in obtaining reliable future predictions. Upscaled cases need to accurately represent the original small-scale geological model to obtain the best results. In addition, regardless of upscaling method, the original permeability field will always be changed. So, consideration should be taken for determining the most appropriate method for each project, however degree of upscaling is the most prominent aspect. Observed production values can potentially be inconsistent with modeled values owing to these variables and therefore, significant consideration should be placed on the degree of upscaling required for the preservation of important geological features in the model.

CONCLUSIONS

The Burro Canyon Formation represents low-sinuosity braided fluvial deposits at the base that transition upward into sinuous-fluvial deposits. Four main architectural elements are observed, three of which exhibit high reservoir quality: amalgamated channel complexes, amalgamated fluvial-bar channel-fill deposits, isolated fluvial-bar channel-fill deposits, and floodplain deposits. The amalgamated channel complex forms the best reservoir zone owing to its thickness, lateral extent, and high reservoir-quality lithofacies and associated petrophysical values. The low vertical and lateral connectivity of the amalgamated fluvial-bar channel-fill deposits and isolated fluvial-bar channel-fill deposits typically reduces or completely prevents fluid communication between them creating separate reservoir compartments. These architectural elements are completely encased in floodplain deposits.

Two-dimensional reservoir modeling and fluid-flow simulation results show how internal facies heterogeneity of reservoir bodies impacts fluid flow. BTT varies by almost 50% owing to lithofacies variability from Model 1 (shortest) to Model 2 (longest) scenarios. When channel bounding surfaces are modeled in the amalgamated channel complex, as in Model 3, the concave-up curvature associated with them forces fluid through channel-fill elements along different paths than in models without internal bounding. This generally decreases volumetric sweep and recovery efficiency by an average of 8% and 10%, respectively, in more complex model simulations. However, the channel-bases preferentially align lithofacies with high porosity and permeability, creating pathways for flow and decreasing average BTT by ~2% as compared to Model 2 scenarios and increasing average BTT by 23% from Model 1 scenarios.

Fluid-flow studies on varying grid resolution (cell size) indicate a significant effect on BTT. Increasing cell size results in longer average BTT by 40% from 2x2-grid to 8x8-grid scenarios. The method used for upscaling permeability models is also important. Model parameters that are upscaled using the geometric versus harmonic mean preserve slightly higher ranges of permeability and this results in longer average BTT by 17%. Volumetric sweep efficiency is affected by cell size and upscaling method. There is an average of 9% decrease in values between grid scenarios with the highest (8x8-grids) and the lowest (2x2-grids) recovery efficiencies and an average of 10% decrease between models using the geometric mean and those using the harmonic mean for upscaling. Recovery efficiency does not vary significantly with grid resolution where there is approximately a 3% difference between the highest average recovery efficiencies at BTT in the 8x8-grids and the lowest in the 2x2-grids. Recovery efficiency is also relatively unchanged between upscaling methods with a 3% difference on average.

REFERENCES

Allen, J. R., 1983, Studies in fluviatile sedimentation: bars, bar-complexes and sandstone sheets (low-sinuosity braided streams) in the Brownstones (L. Devonian), Welsh Borders: Sedimentary Geology, v. 33, p. 237-293.

Blakey, R., 2014, North American paleogeographic maps: Early “Mid” Cretaceous, 125 Ma: Paleogeography of western North America and the Colorado Plateau Region DVD, Colorado Plateau Geosystems Inc.

Campbell, C. V., 1976, Reservoir geometry of fluvial sheet sandstone. AAPG Bulletin, v. 60, p. 1009-1020.

Cant, D. J., and R. G. Walker, 1976, Development of a braided fluvial facies model for the Devonian Battery Point Sandstone, Quebec, Canadian Journal of Earth Sciences, v. 13, p. 102-119.

Cole, R., and S. Cumella, 2003, Stratigraphic architecture and reservoir characteristics of the Mesaverde Group, southern Piceance Basin, Colorado, in K. M. Peterson, T. M. Olsen, and D. S. Anderson, eds., Piceance Basin 2003 guidebook: Rocky Mountain Association of Geologists, p. 385 - 442.

Cole, R. D., and S. P. Cumella, 2005, Sand body architecture in the lower Williams Fork Formation (Upper Cretaceous), Coal Canyon, Colorado, with comparison to the Piceance Basin subsurface: The Mountain Geologist, v. 42, p. 85– 107.

Conaghan, P. J., and J. G. Jones, 1975, The Hawkesbury sandstone and the Brahmaputra: a depositional model for continental sheet sandstones. Journal of the Geological Society of Australia, v. 22, p. 275-283.

Corbett, P. W. M., and J. L. Jensen, 1993, Application of probe permeametry to the prediction of two-phase flow performance in laminated sandstones (lower Brent Group, North Sea), Marine and Petroleum Geology, vol. 10, no. 4, p. 335-346.

DeCelles, P. G., 2004, Late Jurassic to Eocene evolution of the Cordilleran thrust belt and foreland basin system, western U.S.A. American Journal of Science, 304, p. 105–168, doi: 10.2475/ajs.304.2.105

Dodge, C. F., D. P. Holler, and R. L. Meyer, 1971, Reservoir heterogeneities of some Cretaceous sandstones. AAPG Bulletin, v. 55, p 1814-1828.

Ellison, A. I., 2004, Numerical modeling of heterogeneity within a fluvial point-bar deposit using outcrop and LIDAR data: Williams Fork Formation, Piceance Basin, Colorado: Master’s thesis, University of Colorado, Boulder, Colorado, p. 234

Fustic, M., S. M. Hubbard, R. Spencer, D. G. Smith, D. A. Leckie, B. Bennett, and S. Larter, 2011, Recognition of down-valley translation in tidally influenced meandering fluvial deposits, Athabasca Oil Sands (Cretaceous), Alberta, Canada, Marine and Petroleum Geology, v. 29, p. 219-232.

Haszeldine, R. S., 1983. Fluvial bars reconstructed from a deep, straight channel, Upper Carboniferous coalfield of northeast England. Journal of Sedimentary Petrology, v. 53, p. 1233-1247.

Hubbard, S. M., D. G. Smith, H. Nielsen, D. A. Leckie, M. Fustic, R. J. Spencer, and L. Bloom, 2011, Seismic geomorphology and sedimentology of a tidally influenced river deposit, Lower Cretaceous Athabasca oil sands, Alberta, Canada, AAPG Bulletin, v. 95, no. 7, p. 1123–1145.

Hurst, A., and K. J. Rosvoll, 1991, Permeability variations in sandstones and their relationship to sedimentary structures, San Diego, CA, United States (USA), Acad. Press, San Diego, CA.

Jackson, M. D., A. H. Muggeridge, S. Yoshida, and H. D. Johnson, 2003, Upscaling permeability measurements within complex heterolithic tidal sandstones, Mathematical Geology, vol. 35, no. 5, p. 499-520.

Johnson, R. C., 1989, Geologic history and hydrocarbon potential of Late Cretaceous–age low-permeability reservoirs, Piceance Basin, Western Colorado: U.S. Geological Survey Bulletin, v. 1787-E, p. 51.

Johnson, R. C., and R. M. Flores, 2003, History of the Piceance Basin from Latest Cretaceous through Early Eocene and the characterization of Lower Tertiary sandstone reservoirs. In: Peterson, K. M., Olson, T. M. & Anderson, D. S. (eds) Piceance Basin 2003 Guidebook. Rocky Mountain Association of Geologists, Denver, CO, p. 21–61.

Jones, J. R., A. J. Scott, and L. W. Lake, 1987, The geologic aspects of reservoir characterization for numerical simulation: Mesaverde meander-belt sandstone, northwestern Colorado: Society of Petroleum Engineers Formation Evaluation, SPE Paper 13052, p. 97–107.

Kelling, G., 1968, Patterns of sedimentation in Rhonda beds of south Wales. AAPG Bulletin, v. 52, p. 2369-2386.

Kirkland, J. I., and S. K. Madsen, 2007, The Lower Cretaceous Cedar Mountain Formation, eastern Utah- the view up an always interesting learning curve, *in* Lund W.R. editor, Field guide to geological excursion in southern Utah: Geological Society of America Rocky Mountain Section 2007 Annual Meeting, Grand Junction Geological Society and Utah Geological Association Publication 35, p. 108, compact disk

Labrecque, P. A., S. M. Hubbard, J. L., Jensen, and H. Nielsen, 2011, Sedimentology and stratigraphic architecture of a point bar deposit, Lower Cretaceous McMurray Formation, Alberta, Canada: Bulletin of Canadian Petroleum Geology, v. 59, p. 147-171.

Miall, A. D., 1977a, Lithofacies Types and Vertical Profile Models in Braided River Deposits: A Summary: Canadian Society of Petroleum Geologists, v. 5, p. 23-32.

Miall, A. D., 1977b, A review of the braided-river depositional environment, Earth-Sci. Rev., 13, p. 1-62.

Miall, A. D., 1977c, Lithofacies types and vertical profile models in braided river deposits: a summary, Canadian Society of Petroleum Geologists, v. 5, p. 597-604.

Miall, A. D., 1985, Architectural element analysis: a new method of facies analysis applied to fluvial deposits: Earth-Science Reviews, v. 22, p. 261 – 308.

Moody-Stewart, M., 1966, High- and low-sinuosity stream deposits, with examples from the Devonian of Spitsbergen. Journal of Sedimentary Petrology, v. 36, p. 1102-1117.

Nichols, G., 2009, Sedimentology and Stratigraphy, Second Ed., Wiley-Blackwell, p. 410.

Patterson, P. E., T. A. Jones, C. J. Donofrio, A. D. Donovan, and J. D. Ottmann, 2002, Geologic modeling of external and internal reservoir architecture of fluvial systems, in M. Armstrong, C. Bettini, N. Champigny, and A. Galli, eds., Geostatistics Rio 2000, Proceedings of the Geostatistics Sessions of the 31st International Geological Congress, Rio de Janeiro, Brazil: Kluwer Academic Publishers, p. 41-43.

Patterson, P. E., C. R. Jones, and R. L. Skelly, 2010, Hierarchical description and sequence stratigraphy of Cretaceous alluvial strata, Hawkins Field, Texas, in V. Abreu, J. E. Neal, K. M. Bohacs, and J. L. Kalbas, eds., Sequence Stratigraphy of Siliciclastic Systems – The ExxonMobil Methodology: Tulsa, SEPM (Society for Sedimentary Geology), p. 226.

Powers, M.C., 1953, A new roundness scale for sedimentary particles: Journal of Sedimentary Petrology, 23, p. 117-119.

Pranter, M. J., A. I. Ellison, R. D. Cole, and P. E. Patterson, 2007, Analysis and modeling of intermediate-scale reservoir heterogeneity based on a fluvial point-bar outcrop analog, Williams Fork Formation, Piceance Basin, Colorado. American Association of Petroleum Geologists Bulletin, v. 91, p. 1025-1051.

Pranter, M. J., R. D. Cole, H. Panjaitan, and N. K. Sommer, 2009, Sandstone-body dimensions in a lower coastal-plain depositional setting: lower Williams Fork Formation, Coal Canyon, Piceance Basin, Colorado, U.S.A. American Association of Petroleum Geologists Bulletin, 93, p. 1379–1401.

Robinson, J. W., and P. J. McCabe, 1997, Sandstone-body and shale-body dimensions in a braided fluvial system: Salt Wash Sandstone member (Morrison Formation), Garfield County, Utah. AAPG Bulletin, V. 81, No. 8, p. 1267-1291.

Salazar, M. O., and J. R. Villa, 2007, Permeability upscaling techniques for reservoir simulation, Latin American & Caribbean Petroleum Engineering Conference April 15-18, Buenos Aires, Argentina, Society of Petroleum Engineers, p. 4-6. https://doi.org/10.2118/106679-MS.

Sharma, R. J., 2013, Fluvial architecture and sequence stratigraphy of the Upper Williams Fork Formation, Plateau Creek Canyon, Piceance Basin, Colorado. MS Thesis, University of Colorado, Boulder, CO. p. 132.

Smith, D. G., S. M. Hubbard, D. A. Leckie, and M. Fustic, 2009, Counter point bar deposits: lithofacies and reservoir significance in the meandering modern Peace River and ancient McMurray Formation, Alberta, Canada: Sedimentology, v. 56, p. 1655-1669.

Sprague, A. R., P. E. Patterson, R. E. Hill, C. R. Jones, K. M. Campion, J. C. Van Wagoner, M. D. Sullivan, D. K. Larue, H. R. Feldman, T. M. Demko, R. W. Wellner, J. K. Geslin, 2002, The physical stratigraphy of fluvial strata: a hierarchical approach to the analysis of genetically related elements for improved reservoir prediction: AAPG Annual Convention Abstracts, p. A167-A168.

Stokes, W. L., 1952, Lower Cretaceous in Colorado Plateau. Bulletin of the American Association of Petroleum Geologists, 36, 1766-1776.

Tellez, J. J., and M. J. Pranter, 2016, Application of UAV-based Photogrammetry for Outcrop Characterization of Fluvial Deposits of the Burro Canyon Formation, Piceance Basin, Colorado: AAPG Geoscience Technology Workshop: New Opportunities with Drones: New Needs, FAA Rule Changes, New Technologies.

Walker, R. G., and D. J. Cant, 1984, Sandy fluvial systems, in R. G. Walker, ed., Facies Models, Second Edition, Geoscience Canada, Reprint Series 1, p. 71-89.

Weber, K. J., 1982, Influence of common sedimentary structures on fluid flow in reservoir models, JPT Journal of Petroleum Technology, vol. 34, no. 3, p. 665-672.

Willhite, G. P., 1986, Waterflooding, SPE Textbook Series, 3. Richardson, Texas. 326 p.

Willis, B., 2007, Three-dimensional connectivity of channel point bar architectural elements, AAPG Annual Meeting Abstracts, Long Beach, California, p. 150-151.

Young, R. G., 1960, Dakota Group of Colorado Plateau. Bulletin of the American Association of Petroleum Geologists, 44, p. 156-194.

Young, R. G., 1970, Lower Cretaceous of Wyoming and the Southern Rockies. The Mountain Geologist, 7, p. 105-121.

Young, R. G., 1973, Depositional environments of basal Cretaceous rocks of the Colorado Plateau. In J. E. Fassett, ed., Cretaceous and Tertiary Rocks of the Southern Plateau: A Memoir of the Four Corners Geological Society, Farmington, NM, Four Corners Geological Society, p. 10-27.

Young, R. G., 1975, Lower Cretaceous rocks of northwestern Colorado and northeastern Utah. Rocky Mountain Association of Geologists- 1975 Symposium, p. 141-147.

APPENDIX A

Outcrop Description and Interpretation

Key Lithofacies in the Burro Canyon Formation

Burro Canyon facies A: granule-cobble conglomerate

Granule-cobble conglomerate facies is composed of tan, low-angle cross-stratified conglomerate deposited in longitudinal bars (Table 5). The matrix is composed of very coarse-grained, round to subround sand and the framework is commonly white, gray, and red, round to subround, pebble- and cobble-sized clasts (<7 cm; 2.8 in). Clasts are mostly chert, silicified limestone, and quartzite.

Burro Canyon facies B: conglomeratic sandstone

Conglomeratic sandstone facies is composed of tan to red, large-scale, low-angle, inclined cross-stratified conglomeratic sandstone. Clasts are white to gray, subround, very coarse-grained to pebble-sized (<9 cm; 3.5 in) and commonly found as densely clustered lenses. This facies was probably deposited within longitudinal bars. The matrix is medium-to coarse-grained, subround, moderately sorted sandstone. Graded beds are common in this facies with the largest clasts lining basal surfaces and cycles range from approximately 2 cm (0.78 in) to 15 cm (6 in) in thickness, and thin and fine upwards. Bedding can become contorted in some areas.

Burro Canyon facies C: cross-stratified sandstone

Cross-stratified sandstone is composed of tan to red, varying medium-scale cross-stratified sandstone. Stratification observed includes tabular-planar cross-stratification, wedge-tangential cross-stratification, and less-commonly horizontal-planar bedding indicating the migration of linguoid, transverse, and cross-channel bars across each other (Table 5). This facies could also consist of compound bar deposits. The sandstone is fine- to medium-grained and well sorted, with mudstone and quartzite gravel clasts found along scour surfaces. Bedding ranges from 0.15 m to 0.3 m (0.5 ft to 1 ft) thick.

Burro Canyon facies D: fining-upward sandstone

Fining-upward sandstone facies is composed of tan to red, low-angle to horizontal bedded sandstone with fining-upward cycles ranging in thickness from approximately 0.17 m to 3 m (0.5 ft to 9.8 ft). This facies was likely deposited in a compound bar setting such as a side bar or lateral bar. Grains are mostly subangular, fine to medium sand. Angular mudstone chips are commonly found along the base of beds.

Burro Canyon facies E: gray-green mudstone

Gray-green mudstone facies is found as a highly unconsolidated, vegetation and colluvium covered mudstone and in some areas is silicified, thinly laminated and very brittle. Unconsolidated sections are slope-forming and covered in colluvium and vegetation in some areas.

Figure A-1. Paleogeographic map of the region surrounding the study area during the time of the Burro Canyon Formation deposition, ~110 Ma, as the Sevier Orodenic Belt continued to rise and the Cretaceous Interior Seaway encroached on the area. The position of the study area (dashed boxed) is indicated. Modified from Blakey (2014).

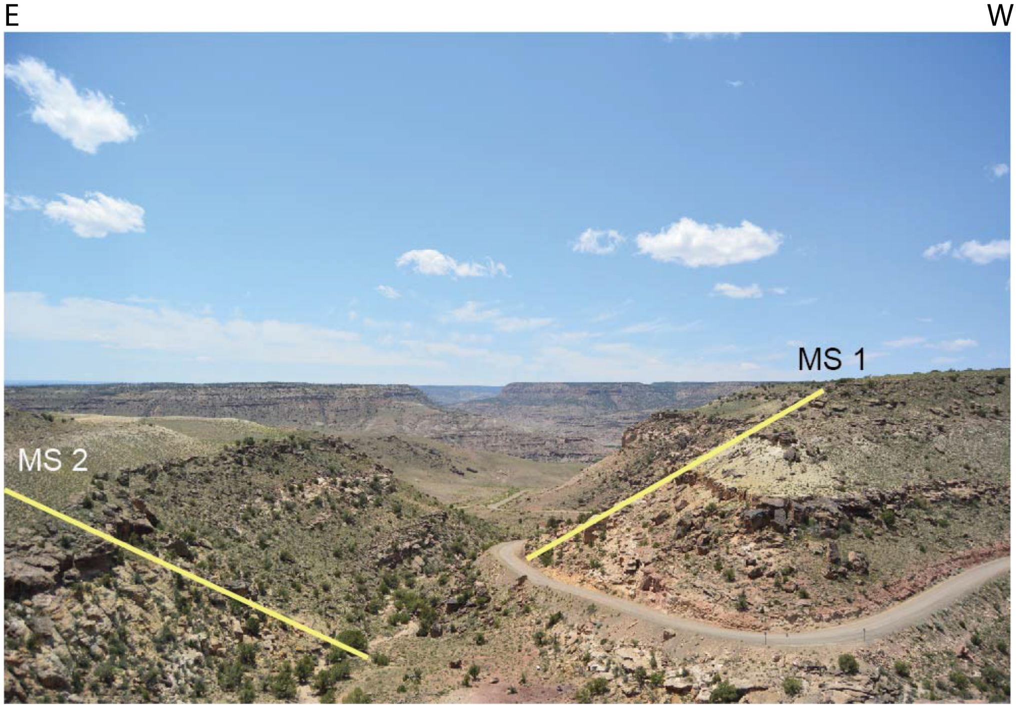

Figure A-2. Approximate location of Measured Section 1 (MS 1) and Measured Section 2 (MS 2) traverses along 650 Road in Escalante Canyon. Measured sections locations are shown in yellow. Actual paths taken are not depicted due to their complexity. This view is along 650 Road facing south (Figure 3).

Figure A-3. Images (A) and (B) showing the amalgamated channel complex (Facies Association 1) in the Burro Canyon Formation where Measured Section 1 was recorded. (A) shows braid bars stacking to form thick and highly-variable complexes of cross-stratified sandstone. (B) is a closer look at the same interval showing cross-stratification.

Alluvial Hierarchical Element	**Description**
Bar	The aggregate of genetically related beds and bedsets deposited within a confined channel. May form by lateral- or downstream-accretion, or as vertically aggrading fields of migrating bedforms.
Bar Set	A relatively conformable succession of genetically related bars that amalgamate vertically and/or laterally within the channel. Typically exhibit a fining-upward grain-size trend.
Channel-Fill	A relatively conformable succession of genetically related bar or bar-set elements that are deposited and preserved within a river channel that is defined by bankful discharge. Typically exhibit a fining-upward grain-size trend which reflects scouring, filling, and abandonment of the channel.
Channel Complex	Two or more channel-fill elements of similar fill type and their coeval floodplain deposits. Stratal stacking patterns may be described as amalgamated, semi-amalgamated, or non-amalgamated.
Depositional Sequence	A relatively conformable succession of genetically related channel-complex elements and their coeval floodplain strata bounded by regional surfaces of erosion or their correlative conformities ("sequence boundaries"). Typically composed of an amalgamated sand-rich channel complex element that is conformably overlain by a non-amalgamated mud-rich channel complex element.
Sequence Set	Two or more sequences that possess a similar stratal stacking pattern, bounded above and below by regional erosional surfaces or their correlative conformities. Three types are recognized: amalgamated, semi-amalgamated, and non-amalgamated. Allogenic mechanisms, such tectonism or climate, are the primary influences on sequence set accumulation.
Composite Sequence	A succession of sequence sets recording a basin-scale cycle of decreasing and increasing accommodation relative to sedimentation. Rapidly decreasing accommodation results in regional surfaces of erosion which are overlain by amalgamated or semi-amalgamated sequence sets reflecting a return to positive accommodation. These deposits are overlain by non-amalgamated sequence sets which reflect a pronounced increase in accommodation. The non-amalgamated sequence set may be succeeded by a semi-amalgamated sequence set resulting from a decrease in accommodation prior to development of the overlying regional surface of erosion.

Table A-4. Summary of alluvial hierarchical elements
(From Sharma, 2013; *sensu* Patterson et al., 2010)

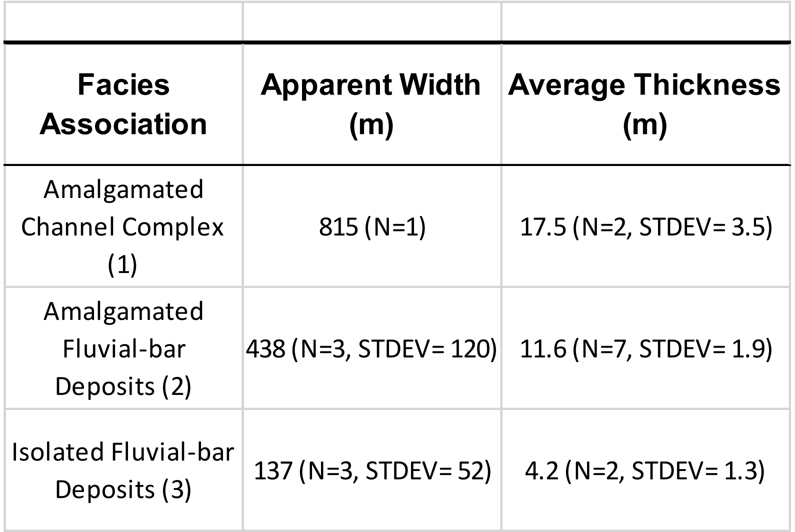

Facies Association	Apparent Width (m)	Average Thickness (m)
Amalgamated Channel Complex (1)	815 (N=1)	17.5 (N=2, STDEV= 3.5)
Amalgamated Fluvial-bar Deposits (2)	438 (N=3, STDEV= 120)	11.6 (N=7, STDEV= 1.9)
Isolated Fluvial-bar Deposits (3)	137 (N=3, STDEV= 52)	4.2 (N=2, STDEV= 1.3)

Appendix A-5. Measurements were recorded across each Facies Association (1-3) and averaged to assist with stratigraphic interpretation. Number of measurements (N=) is recorded along with standard deviation (STDEV=).

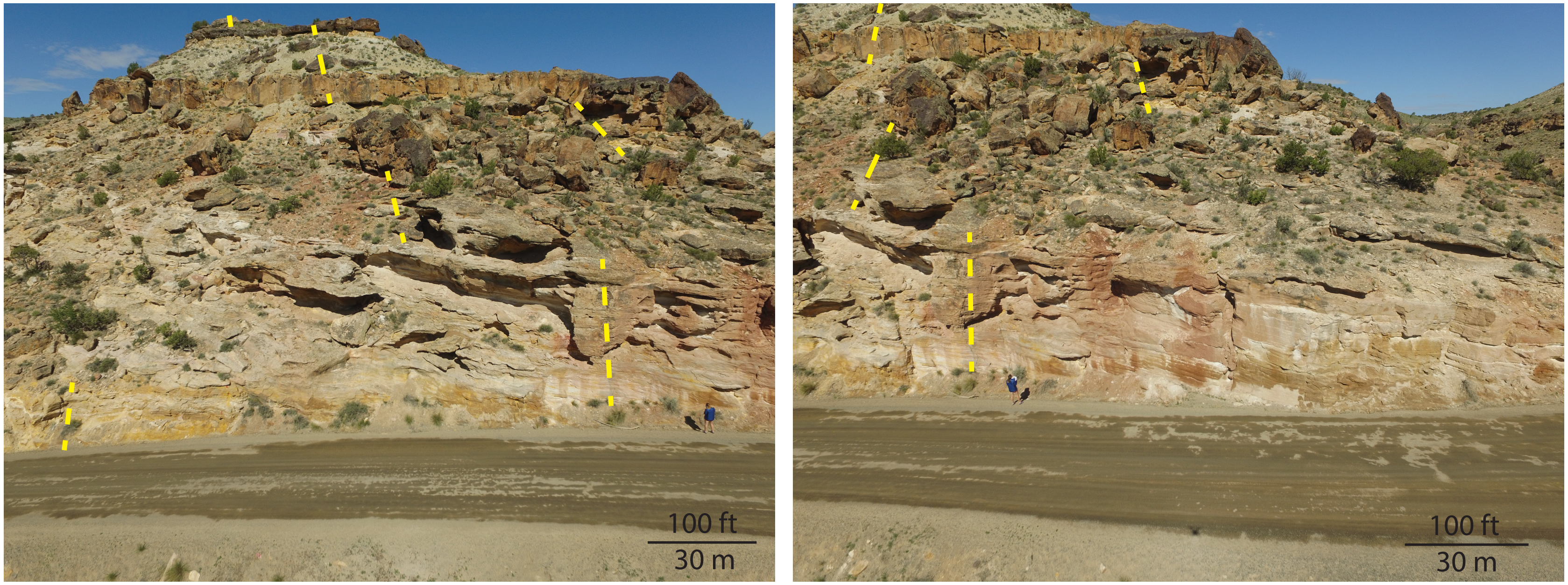

Appendix A-6. Photographs of the west side of 650 Road through Escalante Canyon showing approximate traverse of Measured Section 1 in the yellow dashed lines. (A) shows complete path of MS 1 and (B) shows more exposure of the thick amalgamated channel complex that was used for interpretation of the 3-D drone rendering. The exposures along 650 Road are heavily vegetated and rubble-covered, making it difficult to find complete exposures of the sandstones and conglomerates in the area.

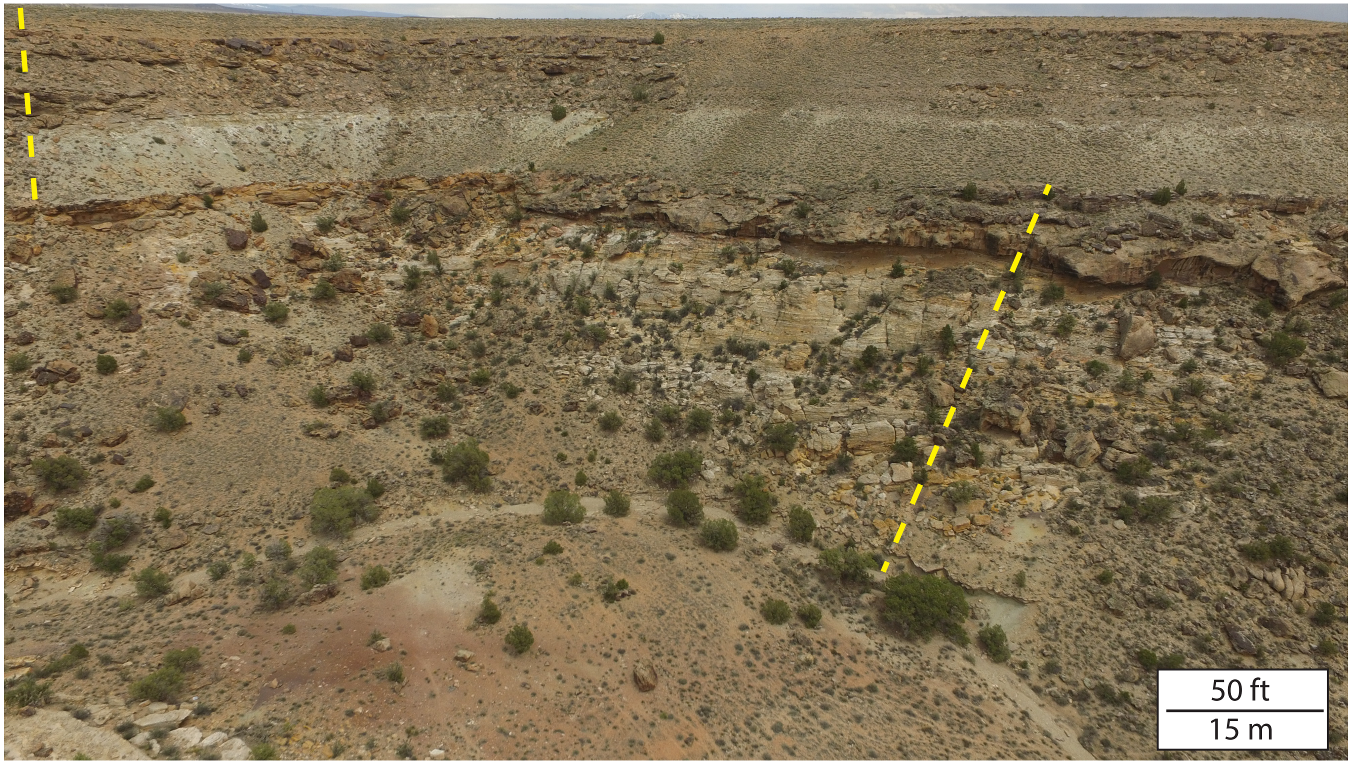

Appendix A-7. Photographs of the east side of 650 Road through Escalante Canyon showing approximate traverse of Measured Section 1 in the yellow dashed lines. (A) shows complete path of MS 2 and (B) shows more exposure of the thick amalgamated channel complex that was used for interpretation of the 3-D drone rendering.

Appendix A-8. Photomicrographs of thin sections used in Figure 7. Images in cross polarized light. (A) Conglomerate facies, (B) conglomeratic sandstone facies, (C) cross-stratified sandstone facies, (D) fining-upward facies, (E) grey-green mudstone facies.

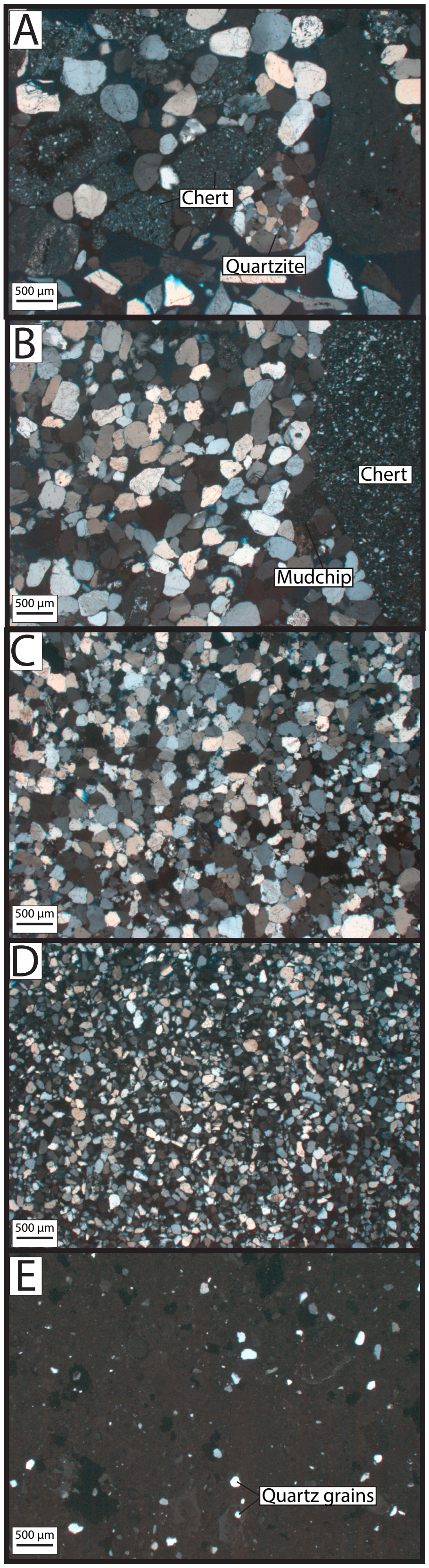

APPENDIX B

UAV-Imaging

Drone images were captured under certain conditions, such as consistent time of day to best illuminate the outcrop face creating consistency in rock coloring; images were taken with at least 75% overlap between neighboring images (<15° camera angle change) and with an acquisition grid including both vertical and oblique camera angles to ensure the processing software could accurately stitch them together at high-resolution. Artifacts such as the sky or bodies of water behind the outcrop in the images needed to be edited and removed in Adobe Photoshop CC prior to being imported into Pix4DMapper Pro to avoid processing artifacts.

Figure B-1. The DJI Phantom 3 drone (shown here) was used for imaging the Burro Canyon Formation. Camera is f/2.8 with 94o field of view and 3-axis gimbal.

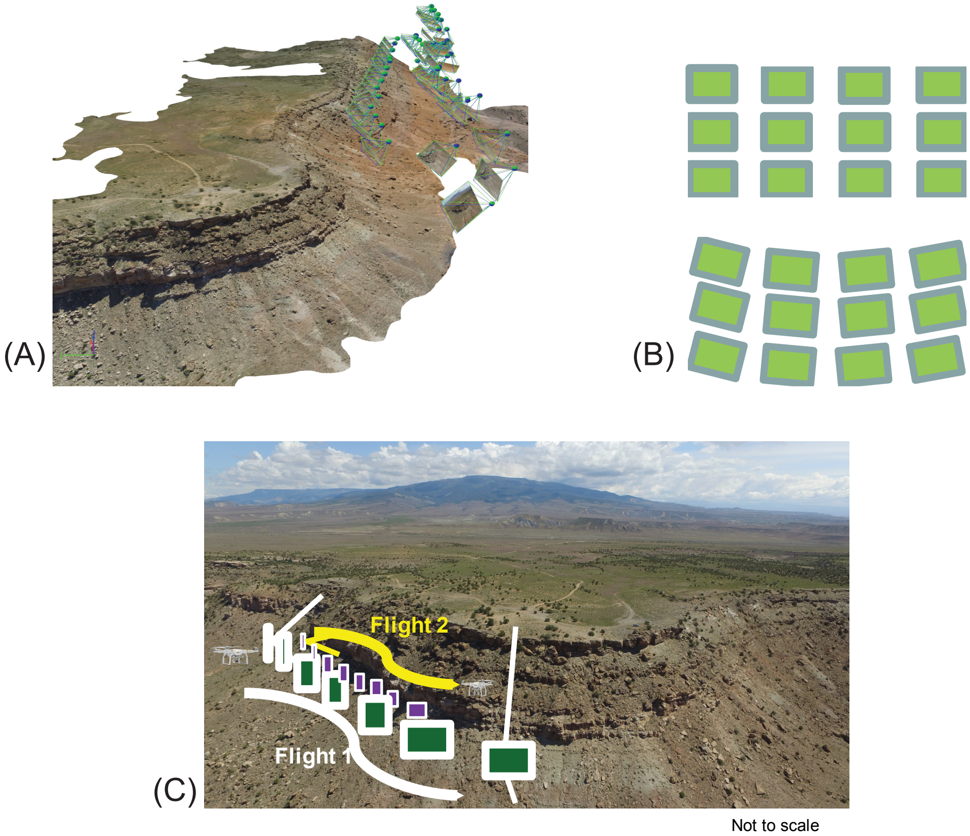

Appendix B-2. To create a successful, high resolution 3-D rendering of the Burro Canyon outcrop with Pix4DMapper Pro, the images need to be captured at optimum angles and overlap. (A) 3-D outcrop reconstruction of the northeast side of Escalante Canyon with drone camera locations at the time of image capture shown as green squares to the right of the outcrop. (B) Idealized image acquisition grid with both vertical (top) and oblique (bottom) camera angles. Minimum 75% image overlap required for successful model creation. (C) Hypothetical flight trajectory maximizing overlap and keeping a consistent flight path for the software to follow for an outcrop model.

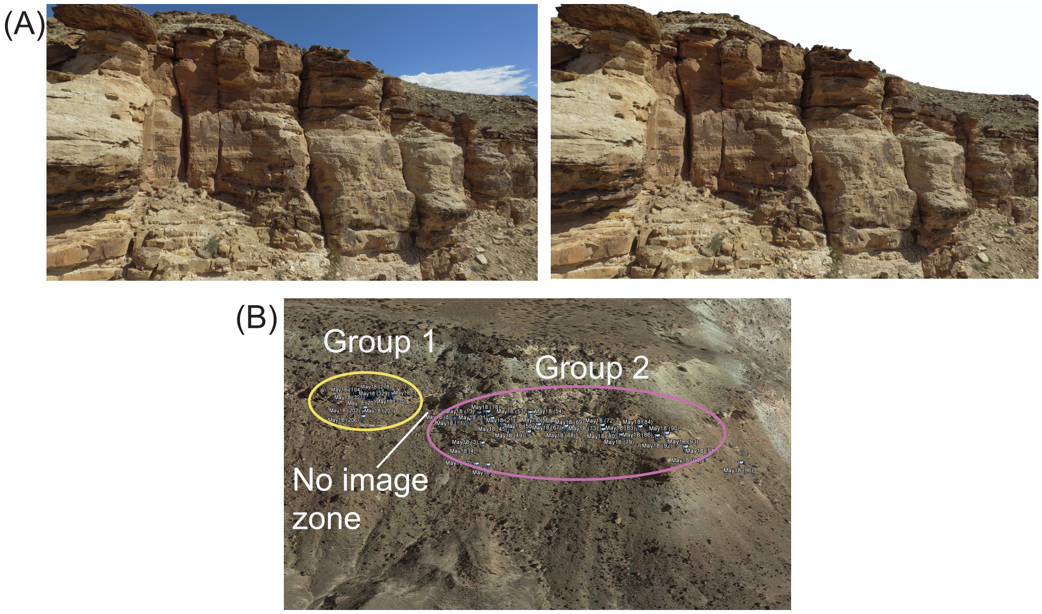

Appendix B-3. Images taken with a drone need to be edited and sorted before importing into Pix4DMapper Pro to create high-resolution 3-D renderings of the outcrop. (A) Using Photoshop, remove any sky or water surfaces from images. The processing software has difficulty recognizing the difference between sky and outcrop here. B) Image locations are imported into Google Earth to manually group them into processing groups. If there is a large gap with no image overlap, the software will not be able to model them accurately and there will be large errors on their location. For best results, the model should have one group which has all of the images located in it with significant overlap (minimum 75% overlap in 3 dimensions- maximum camera angle change of 15o between images).

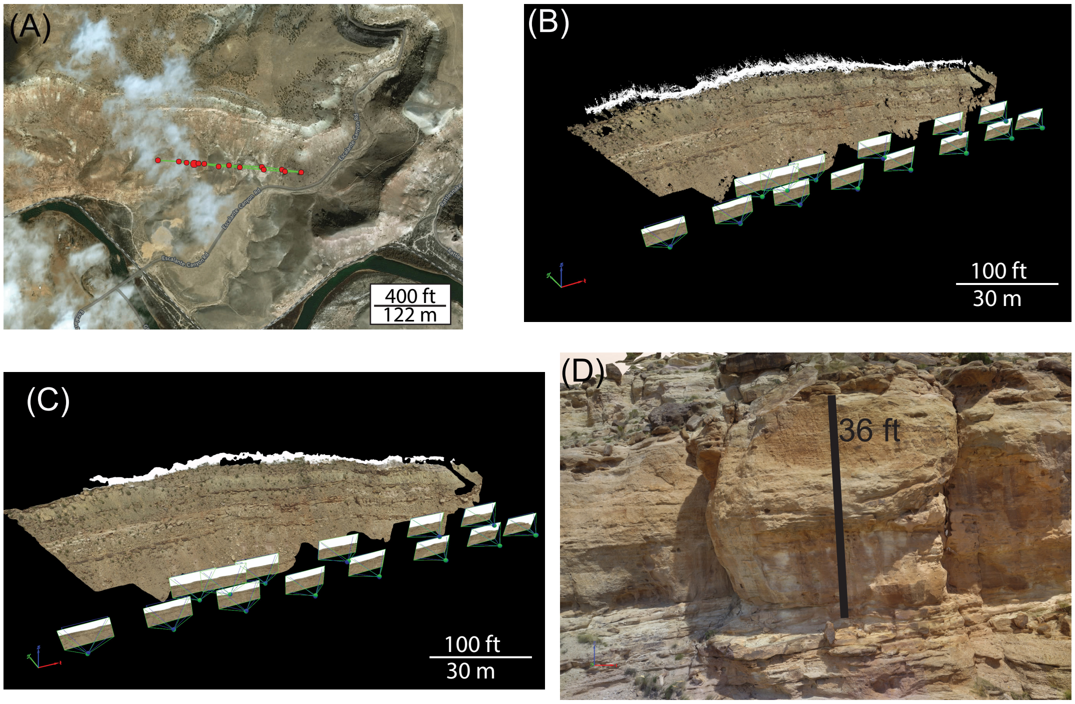

Appendix B-4. Steps taken in Pix4DMapper Pro to create a 3-D outcrop rendering. (A) Map view with drone image locations indicated with red dots and flight path shown with green lines. (B) Densified Point Cloud created from 14 images of the south side of Escalante Canyon. Drone camera positions shown in green squares. (C) Triangle mesh draped over point cloud to add texture to reconstruction. (D) Detailed triangle mesh created using drone imaging ~10-20 feet away from outcrop face to be able to recognize and interpret lithologies and sedimentary structures along an inaccessible vertical face of the outcrop. The sandstone and conglomerate shown comprises an amalgamated channel complex that can become as thick as ~55 ft in some areas making it difficult to interpret without technology or rappelling from the top of the outcrop.

APPENDIX C
Reservoir Modeling

Zone	Zone Division	Layer Thickness	Number of Layers
Model 1			
1	Proportional		40
2	Follow base	0.1	
3	Follow base	0.1	
4	Proportional		70
5	Follow base	0.1	
6	Proportional		43
7	Follow base	0.1	
8	Follow base	0.1	
9	Proportional		20
Model 2			
1	Proportional		40
2	Follow base	0.1	
3	Follow base	0.1	
4	Proportional		60
5	Follow base	0.1	
6	Proportional		30
7	Follow base	0.1	
8	Proportional		33
9	Follow base	0.1	
10	Follow base	0.1	
11	Proportional		26
12	Follow base	0.1	
13	Follow base	0.1	
14	Proportional		20
Model 3			
1	Proportional		40
2	Follow base	0.1	
3	Follow base	0.1	
4	Follow base	0.1	
5	Follow base	0.1	
6	Follow base	0.1	
7	Follow base	0.1	
8	Proportional		60
9	Follow base	0.1	
10	Follow base	0.1	
11	Follow base	0.1	
12	Proportional		30
13	Follow base	0.1	
14	Follow base	0.1	
15	Follow base	0.1	
16	Follow base	0.1	
17	Follow base	0.1	
18	Proportional		33
19	Follow base	0.1	
20	Follow base	0.1	
21	Proportional		26
22	Follow base	0.1	
23	Follow base	0.1	
24	Proportional		20

Appendix C-1. Summary of layering scheme for each zone in each model scenario.

Zone	Lithology	Assigned Value
1	Mudstone	Grey-green mudstone
2	Sandstone	F-M grained x-stratified sandstone
3	Sandstone	F-M grained x-stratified sandstone
4	Mudstone	Grey-green mudstone
5	Sandstone	F-M grained x-stratified sandstone
6	Mudstone	Grey-green mudstone
7	Sandstone	F-M grained x-stratified sandstone
8	Sandstone	F-M grained x-stratified sandstone
9	Mudstone	Grey-green mudstone

Appendix C-2. Summary of assigned values used in Model 1 lithofacies model by zone.

Zone	Lithology	Assigned Value	Major Horizontal Range (ft)	Minor Horizontal (ft)	Vertical Range (ft)	Direction of Anisotropy	Lithology (%)
1	Mudstone	Grey-green mudstone					
2	Sandstone	Fining upward Sandstone					
3	Sandstone	Fining upward Sandstone					
4	Mudstone	Grey-green mudstone					
5	Sandstone	Fining upward Sandstone					
6	Mudstone	Grey-green mudstone					
7	Conglomerate		400	200	5	51	9.12
7	Conglomeratic sandstone		400	200	5	51	24.17
7	Sandstone		400	200	5	51	66.71
8	Mudstone	Grey-green mudstone					
9	Sandstone	F-M grained x-stratified sandstone					
10	Sandstone	F-M grained x-stratified sandstone					
11	Mudstone	Grey-green mudstone					
12	Sandstone	F-M grained x-stratified sandstone					
13	Sandstone	F-M grained x-stratified sandstone					
14	Mudstone	Grey-green mudstone					

Appendix C-3. Summary of variogram values used in Model 2 lithofacies model by zone.

Zone	Lithology	Assigned Value	Major Horizontal Range (ft)	Minor Horizontal (ft)	Vertical Range (ft)	Direction of Anisotropy	Lithology (%)
1	Mudstone	Grey-green mudstone					
2	Sandstone	Fining upward sandstone					
3	Sandstone	Fining upward sandstone					
4	Sandstone	Fining upward sandstone					
5	Sandstone	Fining upward sandstone					
6	Sandstone	Fining upward sandstone					
7	Sandstone	Fining upward sandstone					
8	Mudstone	Grey-green mudstone					
9	Sandstone	Fining upward sandstone					
10	Sandstone	Fining upward sandstone					
11	Sandstone	Fining upward sandstone					
12	Mudstone	Grey-green mudstone					
13	Conglomerate		400	200	5	51	2
13	Conglomeratic sandstone		400	200	5	51	16.32
13	Sandstone		400	200	5	51	81.61
14	Conglomerate		400	200	5	51	16.42
14	Conglomeratic sandstone		400	200	5	51	40.31
14	Sandstone		400	200	5	51	43.28
15	Sandstone	F-M grained x-stratified sandstone					
16	Conglomerate		400	200	5	51	9.6
16	Conglomeratic sandstone		400	200	5	51	23.27
16	Sandstone		400	200	5	51	67.13
17	Sandstone	F-M grained x-stratified sandstone					
18	Mudstone	Grey-green mudstone					
19	Sandstone	F-M grained x-stratified sandstone					
20	Sandstone	F-M grained x-stratified sandstone					
21	Mudstone	Grey-green mudstone					
22	Sandstone	F-M grained x-stratified sandstone					
23	Sandstone	F-M grained x-stratified sandstone					
24	Mudstone	Grey-green mudstone					

Appendix C-4. Summary of variogram values used in Model 3 lithofacies model by zone.

Zone	Lithology	Assigned Value	Major Horizontal Range (ft)	Minor Horizontal (ft)	Vertical Range (ft)	Direction of Anisotropy
1	Mudstone	0				
2	Sandstone		300	170	1	51
3	Sandstone		300	170	1	51
4	Mudstone	0				
5	Sandstone		200	100	3	51
6	Mudstone	0				
7	Sandstone		200	100	2	51
8	Sandstone		200	100	2	51

Appendix C-5. Summary of variogram values used in Model 1 porosity and permeability models by zone.

Zone	Lithology	Assigned Value	Major Horizontal Range (ft)	Minor Horizontal (ft)	Vertical Range (ft)	Direction of Anisotropy
1	Mudstone	0				
2	Sandstone		300	170	0.3	51
3	Sandstone		300	170	0.3	51
4	Mudstone	0				
5	Sandstone		300	170	0.3	51
6	Mudstone	0				
7	Conglomerate		200	100	3	51
7	Conglomeratic sandstone		200	100	3	51
7	Sandstone		200	100	3	51
8	Mudstone	0				
9	Sandstone		200	100	2	51
10	Sandstone		200	100	2	51
11	Mudstone	0				
12	Sandstone		200	100	2	51
13	Sandstone		200	100	2	51

Appendix C-6. Summary of variogram values used in Model 2 porosity and permeability models by zone.

Zone	Lithology	Assigned Value	Major Horizontal Range (ft)	Minor Horizontal (ft)	Vertical Range (ft)	Direction of Anisotropy
1	Mudstone	0				
2	Sandstone		300	170	3	
3	Sandstone		300	170	0.3	51
4	Sandstone		300	170	0.72	
5	Sandstone		300	170	4	
6	Sandstone		300	170	0.3	51
7	Sandstone		300	170	0.81	
8	Mudstone	0				
9	Sandstone		300	170	4	
10	Sandstone		300	170	0.3	51
11	Sandstone		300	170	1.7	
12	Mudstone	0				
13	Conglomerate		200	100	3	51
13	Conglomeratic sandstone		200	100	3	51
13	Sandstone		200	100	3	51
14	Conglomerate		200	100	3	51
14	Conglomeratic sandstone		200	100	3	51
14	Sandstone		200	100	3	51
15	Sandstone		200	100	0.3	51
16	Conglomerate		200	100	3	51
16	Conglomeratic sandstone		200	100	3	51
16	Sandstone		200	100	3	51
17	Sandstone		200	100	0.3	51
18	Mudstone	0				
19	Sandstone		200	100	2	51
20	Sandstone		200	100	2	51
21	Mudstone	0				
22	Sandstone		200	100	2	51
23	Sandstone		200	100	2	51

Appendix C-7. Summary of variogram values used in Model 3 porosity and permeability models by zone. Permeability models used a cokriging algorithm to condition models to porosity volumes.

(A)

Porosity distributions	Normal distributions			
Lithofacies	**Minimum Value**	**Maxiumum Value**	**Average**	**Standard Deviation**
Granule-cobble conglomerate	5	11	8.27	2.64
Conglomeratic sandstone	7	14.6	10.51	2.29
F-M grained x-stratified sandstone	4	13	8.91	3.23
Grey-green mudstone	Assigned 0			
Fining upward sandstone	0.9	5.7	2.67	2.64

(B)

Permeability distributions	Lognormal distributions			
Lithofacies	**Minimum Value**	**Maxiumum Value**	**Average**	**Standard Deviation**
Granule-cobble conglomerate	0.4	4.4	0.4	2.82
Conglomeratic sandstone	0.3	34	4.76	9.42
F-M grained x-stratified sandstone	0.1	48	8.25	15.76
Grey-green mudstone	Assigned 0			
Fining upward sandstone	0.01	0.2	0.1	0.1

Appendix C-8. (A) Porosity and (B) permeability data distributions used for petrophysical modeling. Data was calculated from the Mitchel Energy Federal 8-1 core.

Model 1 Porosity Model Histograms

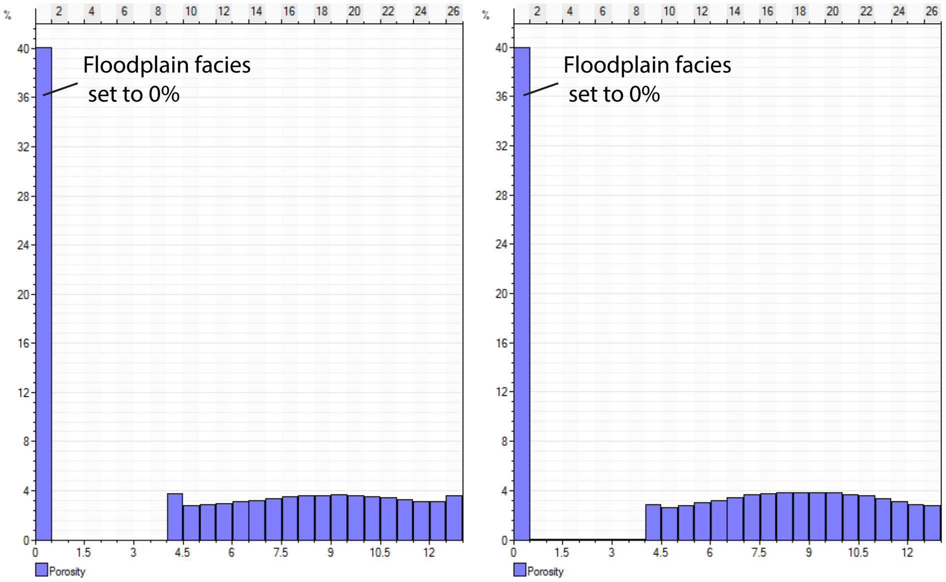
1 m x 1 m

2 m x 2 m

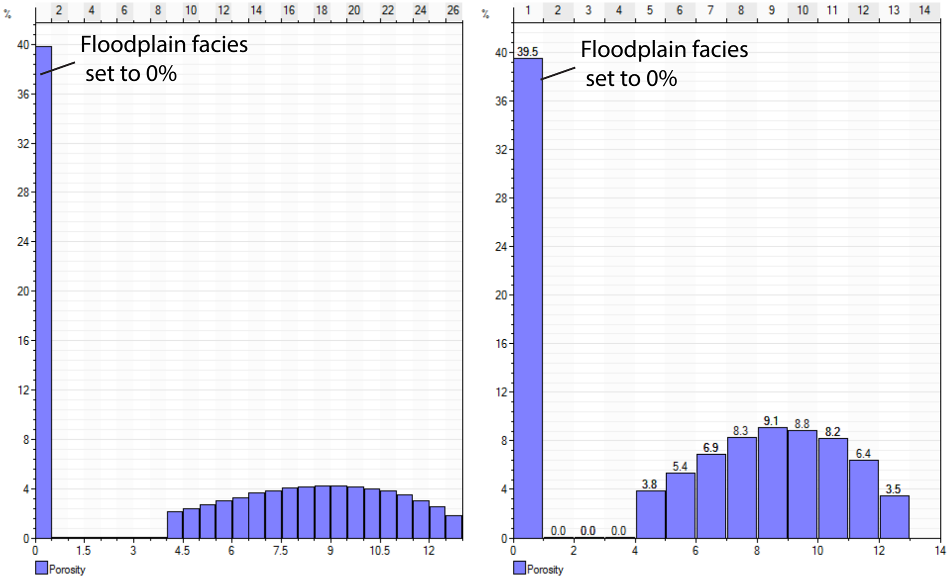
4 m x 4 m

8 m x 8 m

Appendix C-9. Model 1 porosity model data histograms for each grid size.

Model 1 Permeability Model Histograms

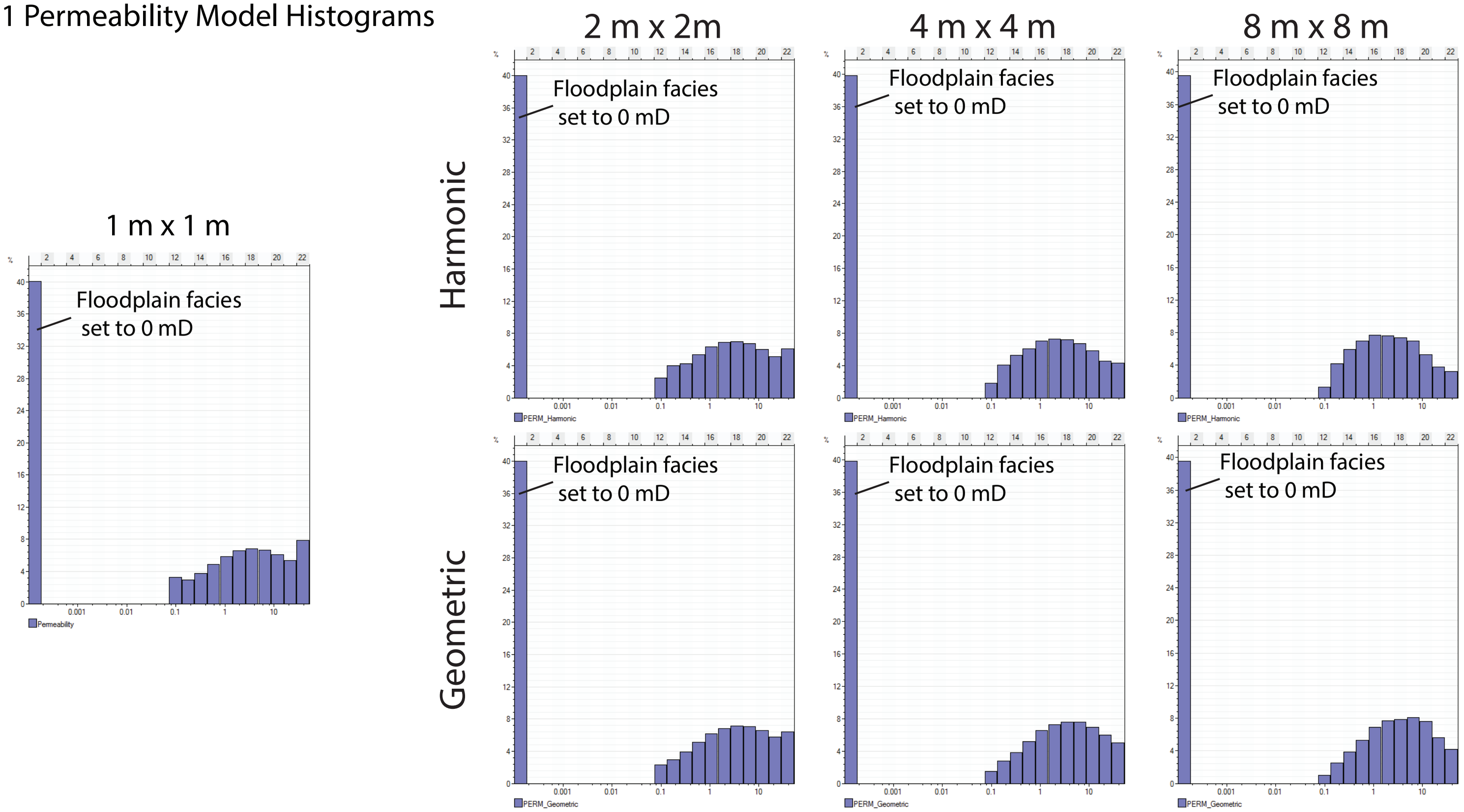

Appendix C-10. Model 1 permeability model data histograms for each grid size and upscaling method (harmonic and geometric).

Model 2 Porosity Model Histograms

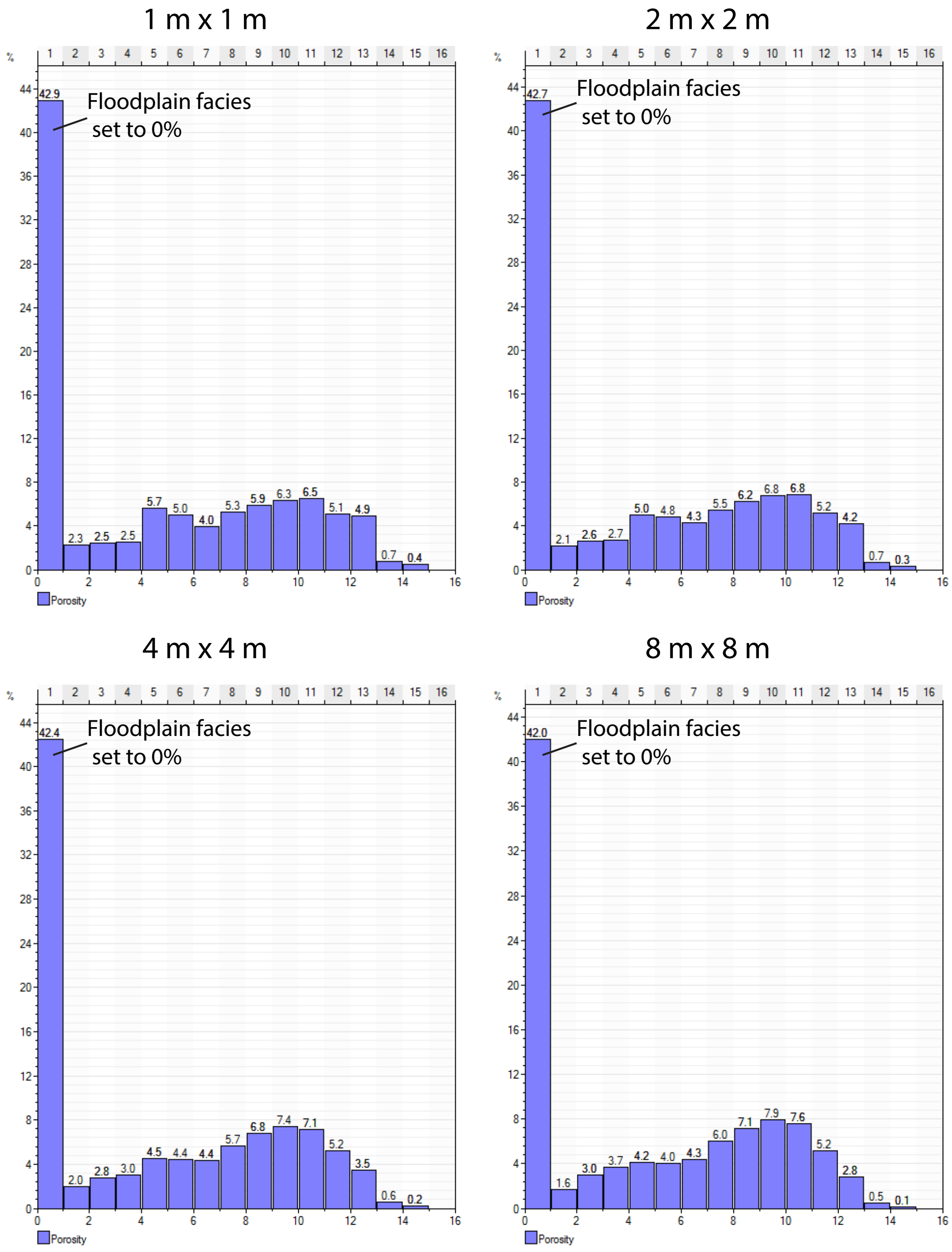

Appendix C-11. Model 2 porosity model data histograms for each grid size.

Model 2 Permeability Model Histograms

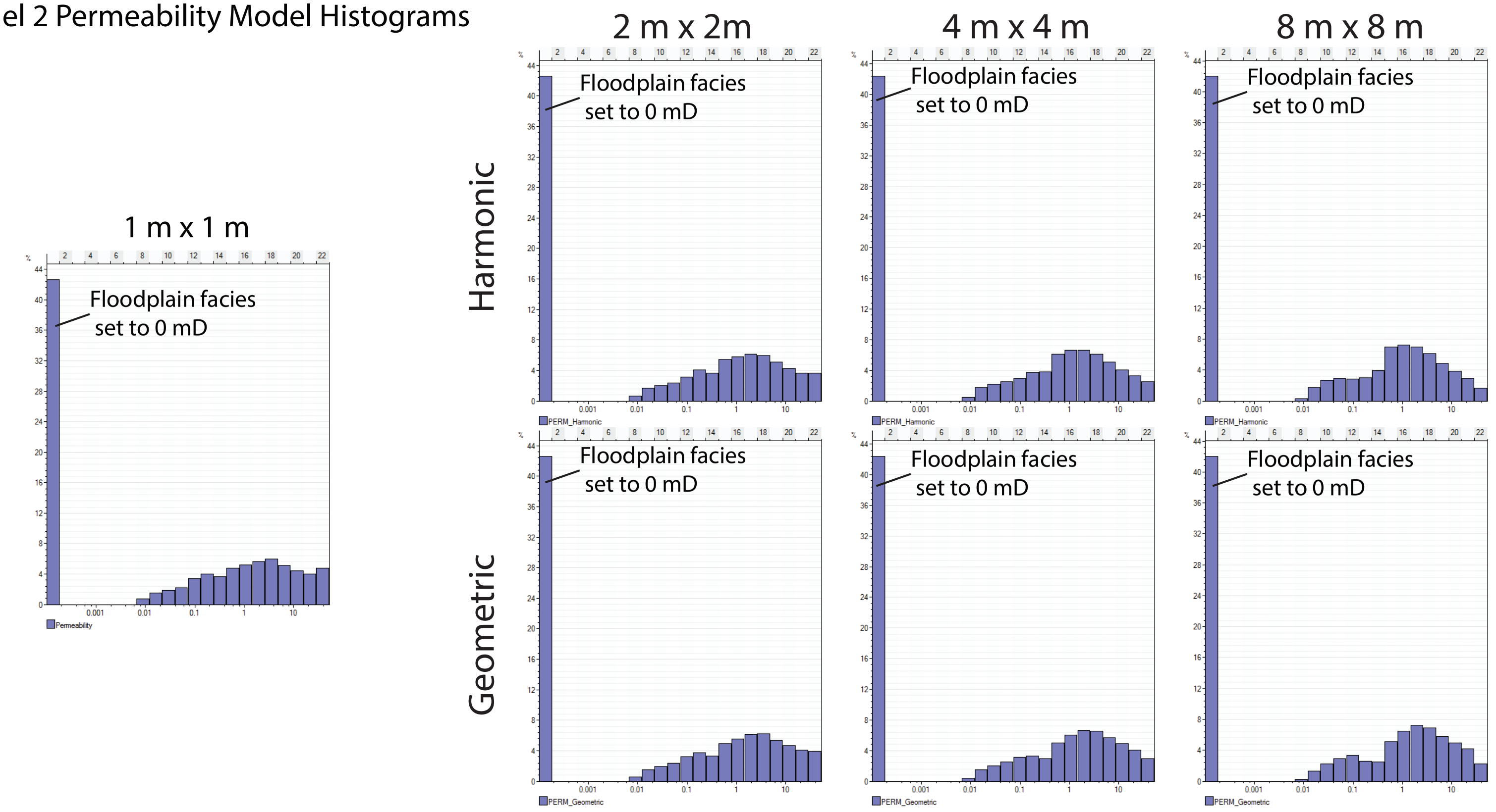

Appendix C-12. Model 2 permeability model data histograms for each grid size and upscaling method (harmonic and geometric).

Model 3 Porosity Model Histograms

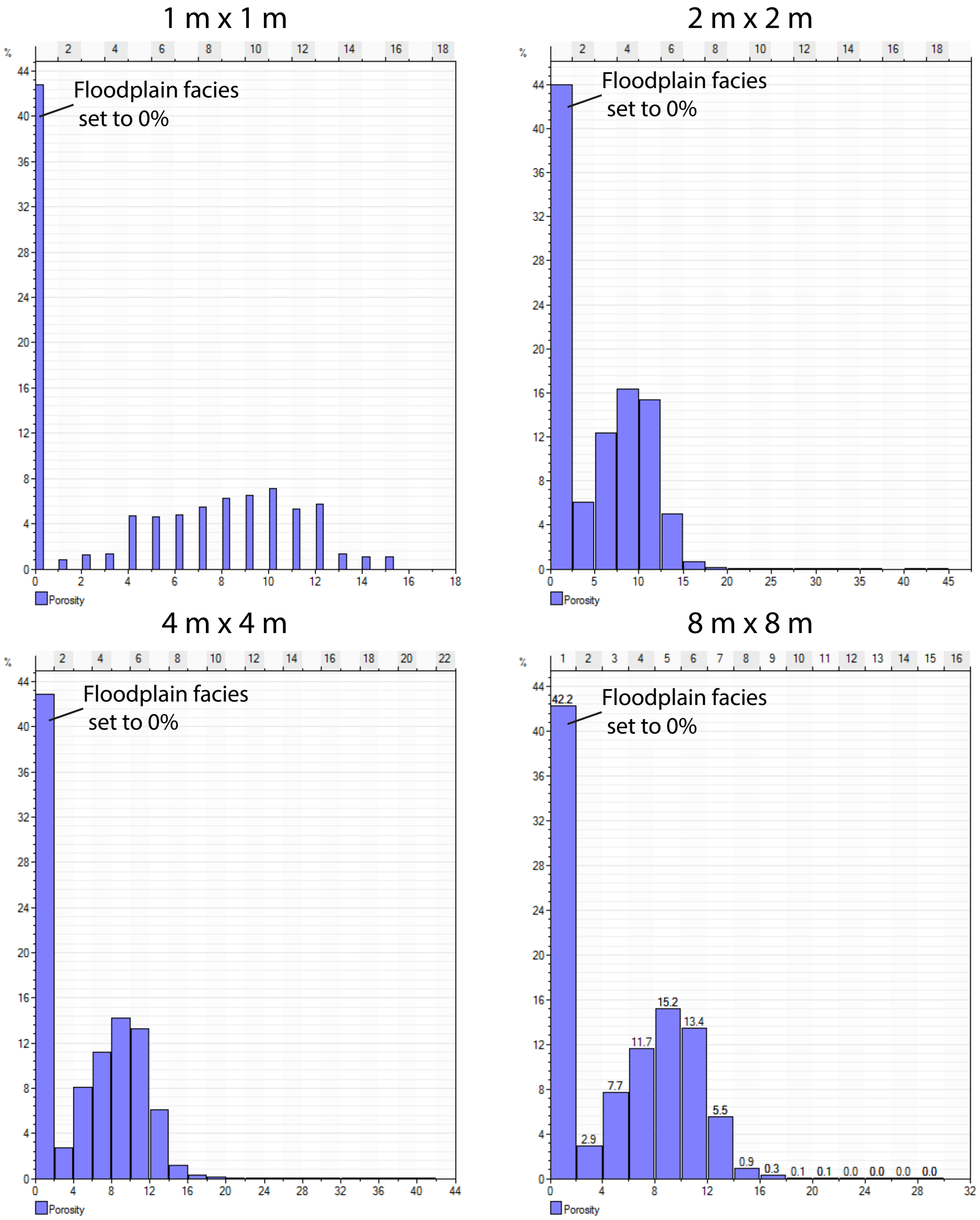
1 m x 1 m

2 m x 2 m

4 m x 4 m

8 m x 8 m

Appendix C-13. Model 3 porosity model data histograms for each grid size.

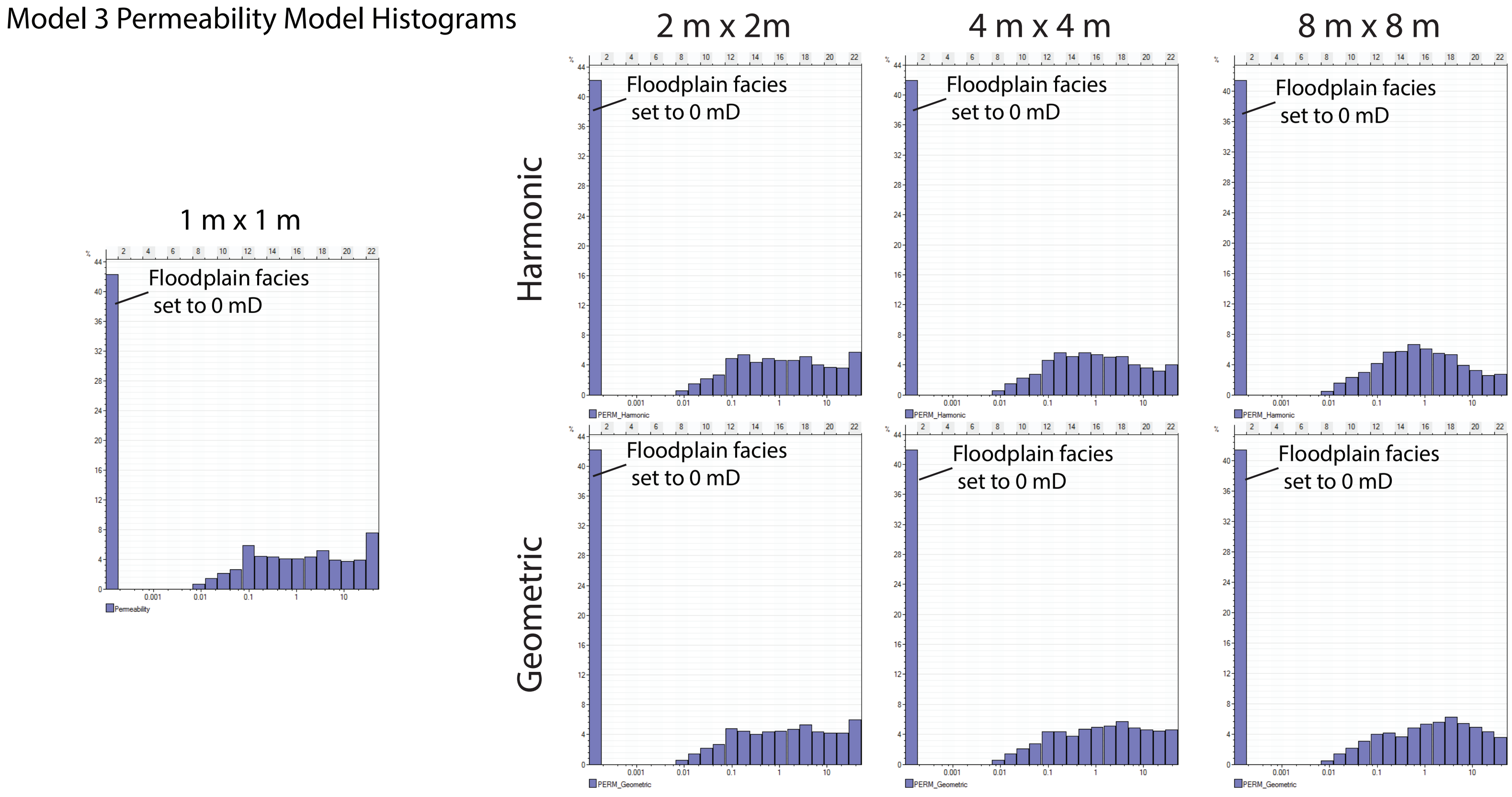
Model 3 Permeability Model Histograms

Appendix C-14. Model 3 permeability model data histograms for each grid size and upscaling method (harmonic and geometric).

(A) Model 1 Lithofacies

Grid Size	% Granule-cobble conglomerate	% Conglomeratic sandstone	% F-M grained x-stratified sandstone	% Grey-green mudstone	% Fining upward sandstone
1x1	0	0	60	40	0
2x2	0	0	60	40	0
4x4	0	0	60.2	39.8	0
8x8	0	0	60.5	39.5	0

(B) Model 2 Lithofacies

Grid Size	% Granule-cobble conglomerate	% Conglomeratic sandstone	% F-M grained x-stratified sandstone	% Grey-green mudstone	% Fining upward sandstone
1x1	3	8	35	42.6	11.4
2x2	3	8	35.1	42.6	11.4
4x4	2.9	7.9	35.3	42.3	11.5
8x8	2.8	7.8	35.6	41.9	11.8

(C) Model 3 Lithofacies

Grid Size	% Granule-cobble conglomerate	% Conglomeratic sandstone	% F-M grained x-stratified sandstone	% Grey-green mudstone	% Fining upward sandstone
1x1	3.2	9.6	33.2	42.3	11.7
2x2	3.2	9.6	33.3	42.1	11.8
4x4	3.1	9.6	33.6	41.8	11.9
8x8	3.1	9.5	34	41.3	12.1

Appendix C-15. Histogram percentages for upscaled lithofacies (A) Model 1, (B) Model 2, and (C) Model 3 by grid size.

Depth	Permeability (mD)	Porosity (%)	Formation
2212.5	0.01	4.8	Mancos
2329.5	0.01	2	Dakota
2330.5	0.01	5.6	Dakota
2331.5	0.01	6.2	Dakota
2336.5	0.1	14.4	Dakota
2337.5	0.1	12.1	Dakota
2338.5	0.3	15.1	Dakota
2339.5	0.2	13.5	Dakota
2340.5	0.2	10.6	Dakota
2341.5	0.2	12	Dakota
2342.5	0.3	11.8	Dakota
2355.5	0.01	6.9	Dakota
2357.5	0.01	5.8	Dakota
2358.5	0.1	4.8	Dakota
2360.5	0.01	6.3	Dakota
2361.5	0.01	2.8	Dakota
2374.5	0.8	5.5	Dakota
2375.5	0.3	6.7	Dakota
2376.5	0.3	8.5	Dakota
2377.5	0.4	8.4	Dakota
2378.5	0.2	13	Dakota
2379.5	0.3	8.2	Dakota
2380.5	0.2	13	Dakota
2383.5	0.5	3.2	Dakota
2384.5	0.3	4.1	Dakota
2394.5	0.01	2.9	Dakota
2395.5	0.01	3.3	Dakota
2398.5	0.01	3.5	Dakota
2399.5	0.01	4.2	Dakota
2407.5	0.01	7	Dakota
2408.5	0.1	3.3	Dakota
2409.5	0.5	10.5	Dakota
2410.5	0.1	7.3	Dakota
2411.5	0.1	6.9	Dakota
2412.5	0.1	10.5	Dakota
2413.5	0.2	7.9	Dakota
2414.5	0.8	12.2	Dakota
2415.5	2.5	13.2	Dakota
2416.5	2.8	14.2	Dakota
2417.5	4.9	10.7	Dakota
2418.5	39	18.8	Dakota
2419.5	6.5	15.7	Dakota
2420.5	103	17.3	Dakota
2421.5	2.3	13.4	Dakota
2422.5	13	14.7	Dakota
2423.5	35	17.7	Dakota
2424.5	37	18.5	Dakota
2425.5	30	16.6	Dakota

Appendix C-16. Mitchel Energy Federal 8-1 core porosity and permeability data.

Depth	Permeability (mD)	Porosity (%)	Formation
2426.5	4.4	14.9	Dakota
2427.5	66	24.6	Dakota
2428.5	1.1	16.7	Dakota
2429.5	3.2	17.3	Dakota
2430.5	6.3	17.7	Dakota
2431.5	0.8	15.8	Dakota
2432.5	0.4	13.1	Dakota
2433.5	0.6	18.5	Dakota
2438.5	0.1	5.4	Burro Cyn.
2439.5	0.01	4.3	Burro Cyn.
2461.5	0.01	4.1	Burro Cyn.
2462.5	0.01	4	Burro Cyn.
2466.5	0.01	2.8	Burro Cyn.
2467.5	0.2	1.4	Burro Cyn.
2468.5	0.01	5.7	Burro Cyn.
2469.5	0.01	0.9	Burro Cyn.
2470.5	0.1	4.5	Burro Cyn.
2471.5	0.2	4.2	Burro Cyn.
2472.5	0.3	9.4	Burro Cyn.
2473.5	0.5	12.4	Burro Cyn.
2474.5	0.2	12.6	Burro Cyn.
2475.5	1	7	Burro Cyn.
2476.5	14	7.9	Burro Cyn.
2477.5	10	12	Burro Cyn.
2478.5	48	10.2	Burro Cyn.
2479.5	0.4	13	Burro Cyn.
2480.5	6	10.5	Burro Cyn.
2481.5	34	10.7	Burro Cyn.
2482.5	0.5	14.6	Burro Cyn.
2483.5	2	7	Burro Cyn.
2484.5	3.6	10.1	Burro Cyn.
2485.5	0.3	11.3	Burro Cyn.
2486.5	1.2	9	Burro Cyn.
2487.5	0.6	12.1	Burro Cyn.
2488.5	5.7	7.5	Burro Cyn.
2489.5	0.7	12.1	Burro Cyn.
2490.5	2.2	8.2	Burro Cyn.
2491.5	0.4	10.6	Burro Cyn.
2492.5	0.4	8.8	Burro Cyn.
2493.5	0.3	5.4	Burro Cyn.

Appendix C-17. Mitchel Energy Federal 8-1 core porosity and permeability data continued.

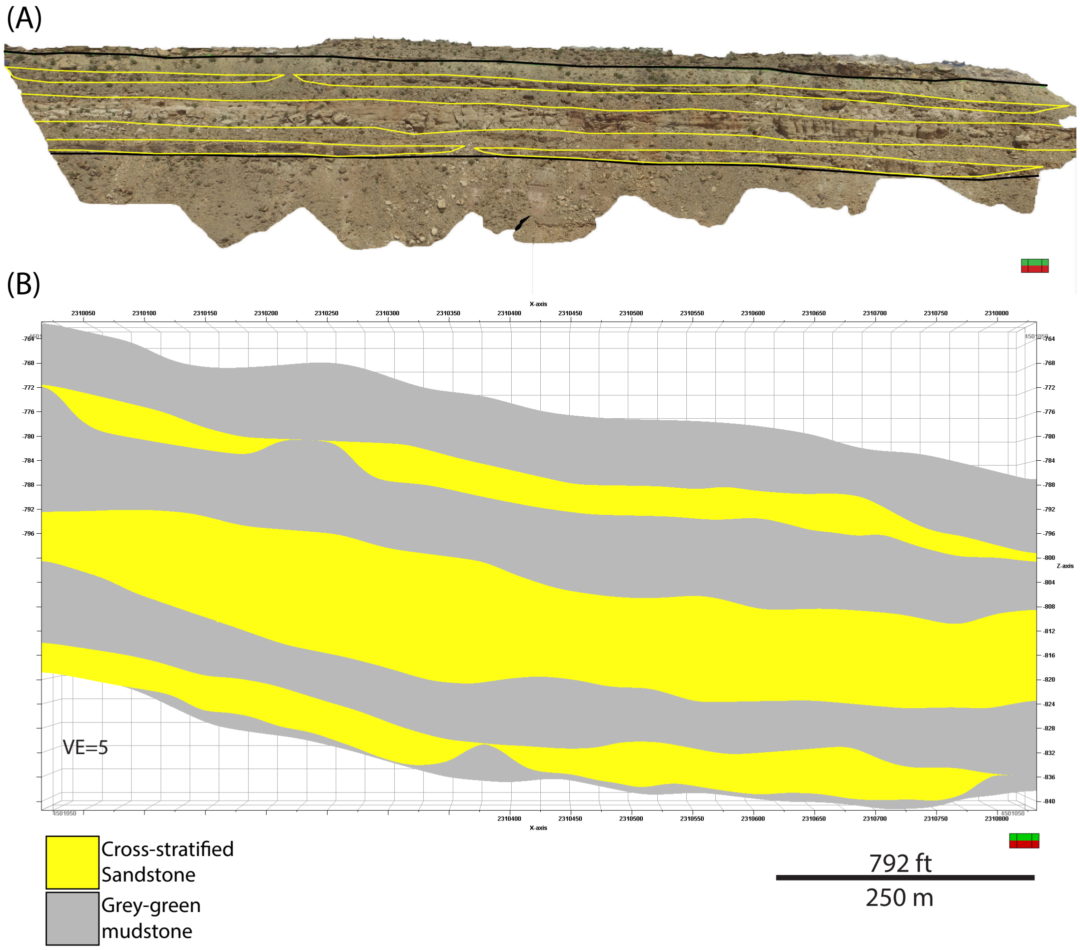

Appendix C-18. Model 1 is the least heterogeneous model scenario and includes limited Facies Associations elements and lithofacies. (A) Reservoir zones interpreted on a 3-D outcrop rendering based on Facies Associations and (B) associated lithofacies model.

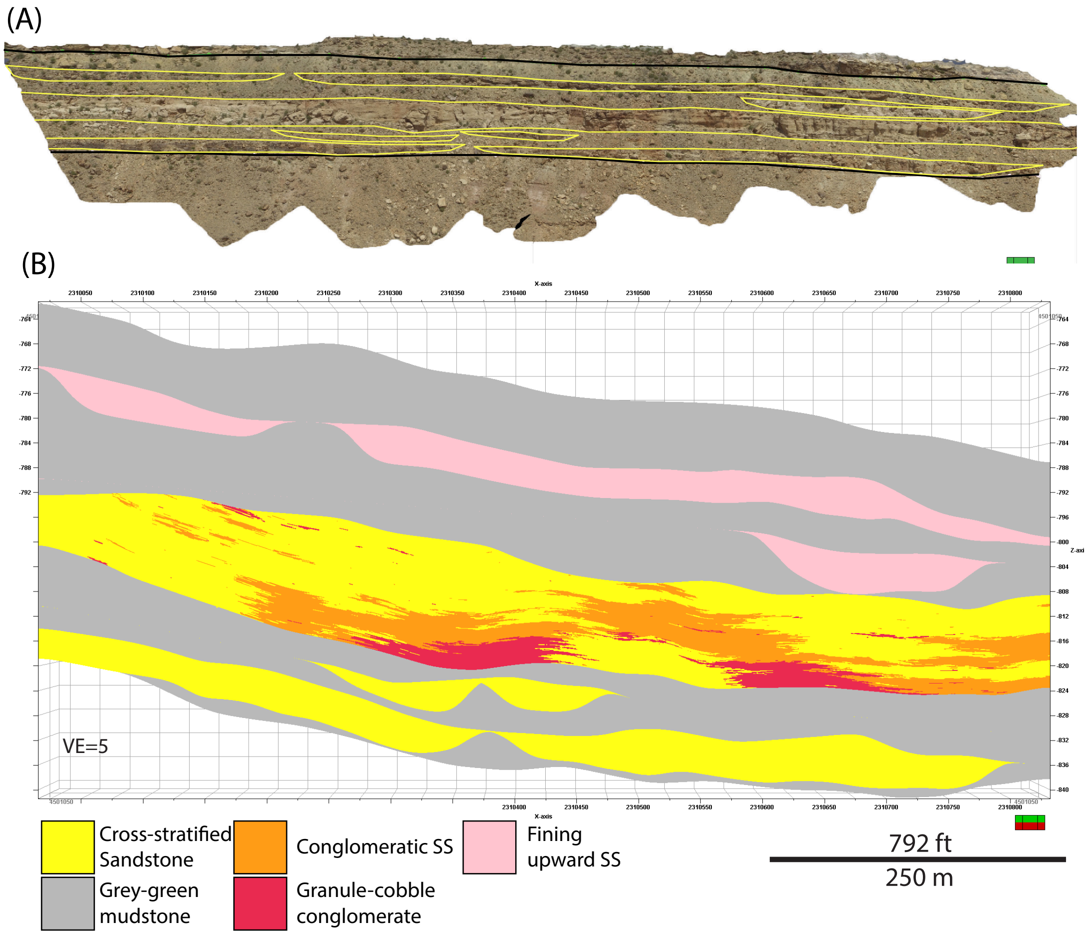

Appendix C-19. Model 2 includes all Facies Associations elements (1-4) and lithofacies. (A) Reservoir zones interpreted on a 3-D outcrop rendering based on Facies Associations and (B) associated lithofacies model.

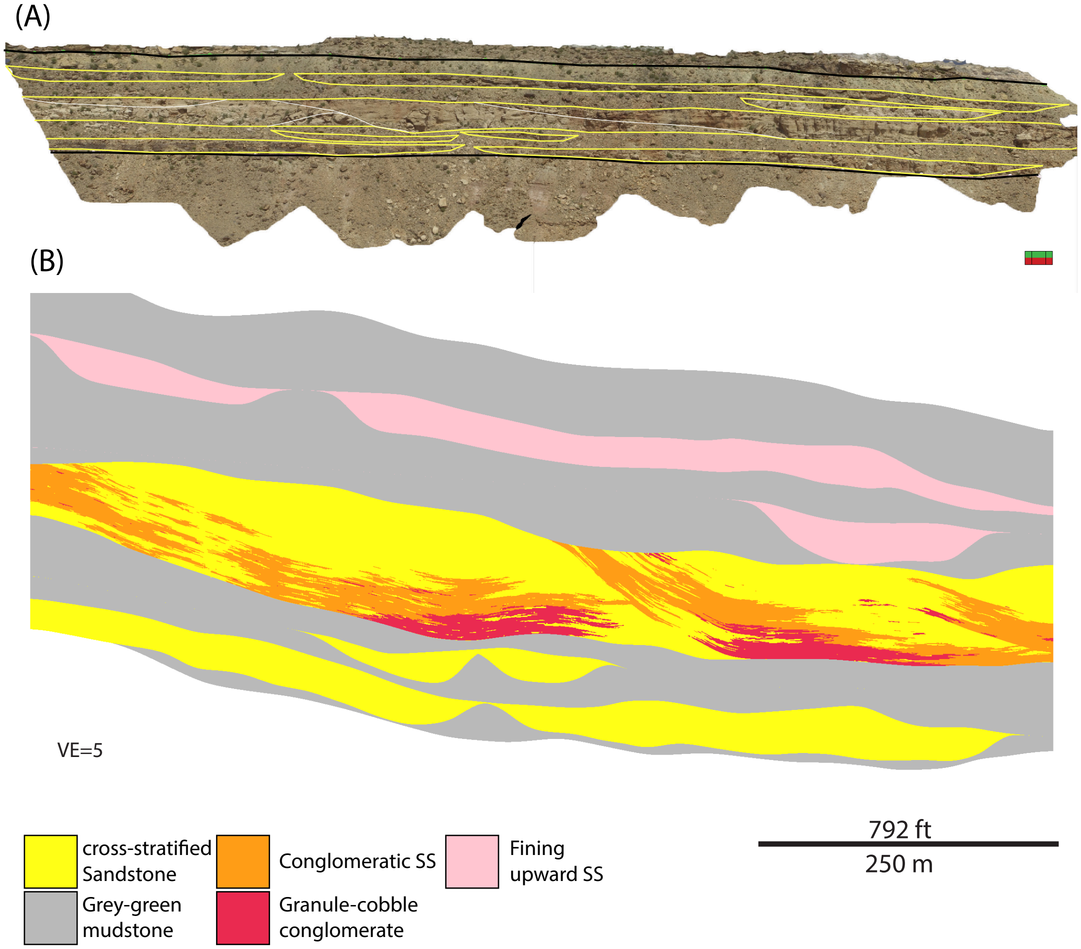

Appendix C-20. Model 3 is the most heterogeneous model scenario and includes all Facies Associations elements and lithofacies and channel bases throughout the middle Amalgamated Channel Complex. (A) Reservoir zones interpreted on a 3-D outcrop rendering based on Facies Associations and (B) associated lithofacies model.

Upscaling Methods from Petrel 2016	
Arithmetic Upscaling	Typically used for additive properties such as porosity, saturation and net-to-gross. Volume weighting will produce a more appropriate arithmetic mean when input values have variable presence within the resulting cell.
Harmonic Upscaling	Gives the exact effective permeability vertically if the reservoir is layered with constant permeability in each layer. The harmonic mean works well with log normal distributions. It is used for permeability because it is sensitive to lower values.
Geometric Upscaling	Normally a good estimate for permeability if it has no spatial correlation and is log normally distributed. The geometric mean is sensitive to lower values, which will have a greater influence of results.

Appendix C-21. Summary of Petrel 2016 upscaling methods used in this study. Arithmetic upscaling was used for porosity models. Harmonic and geometric upscaling was used for permeability models.

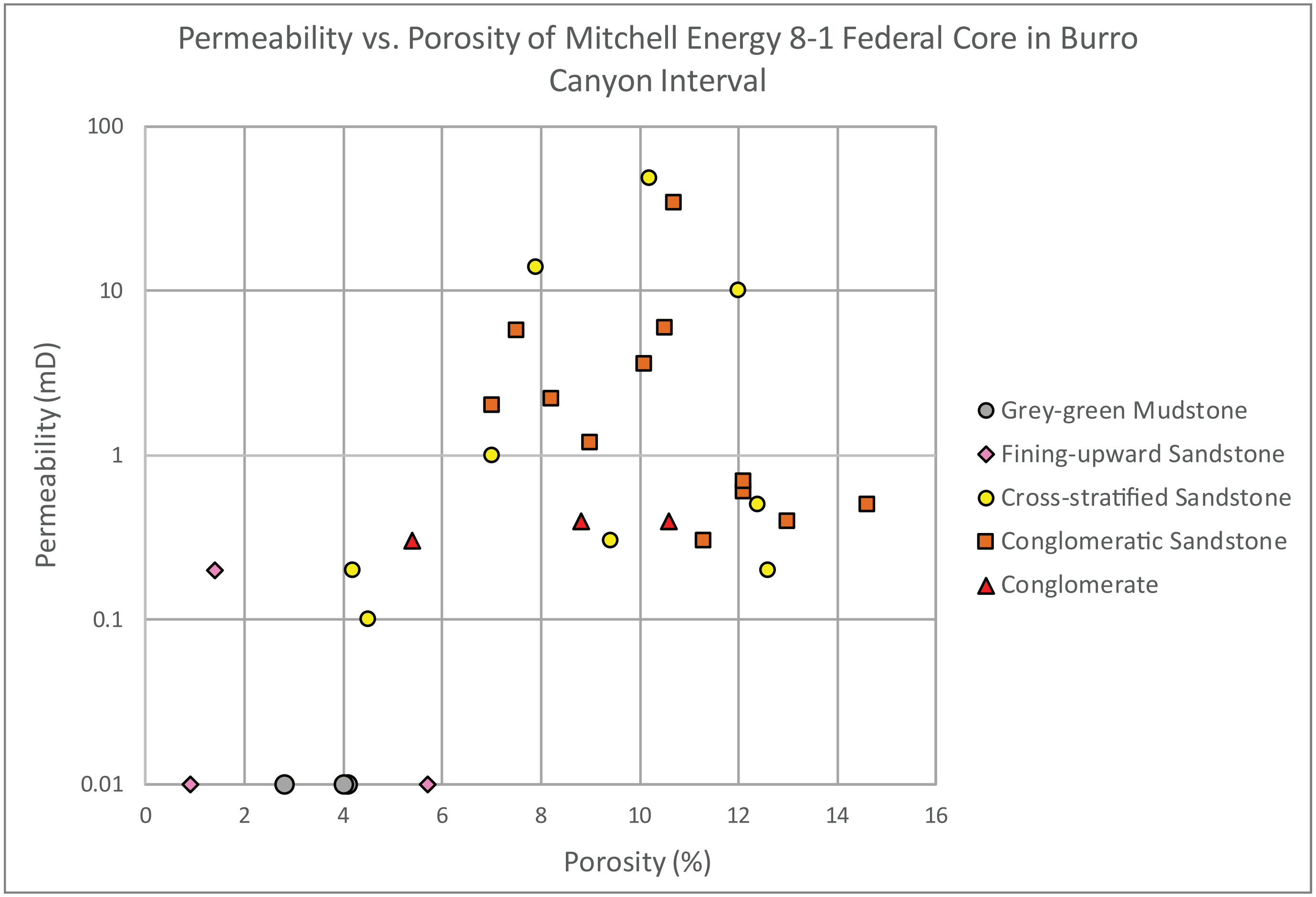

Appendix C-22. Permeability and porosity cross plot of Mitchell Energy 8-1 Federal core data for the Burro Canyon Formation used to populate petrophysical models in this study. Each facies is colored seperately to show relationships and trends in petrophysical data.

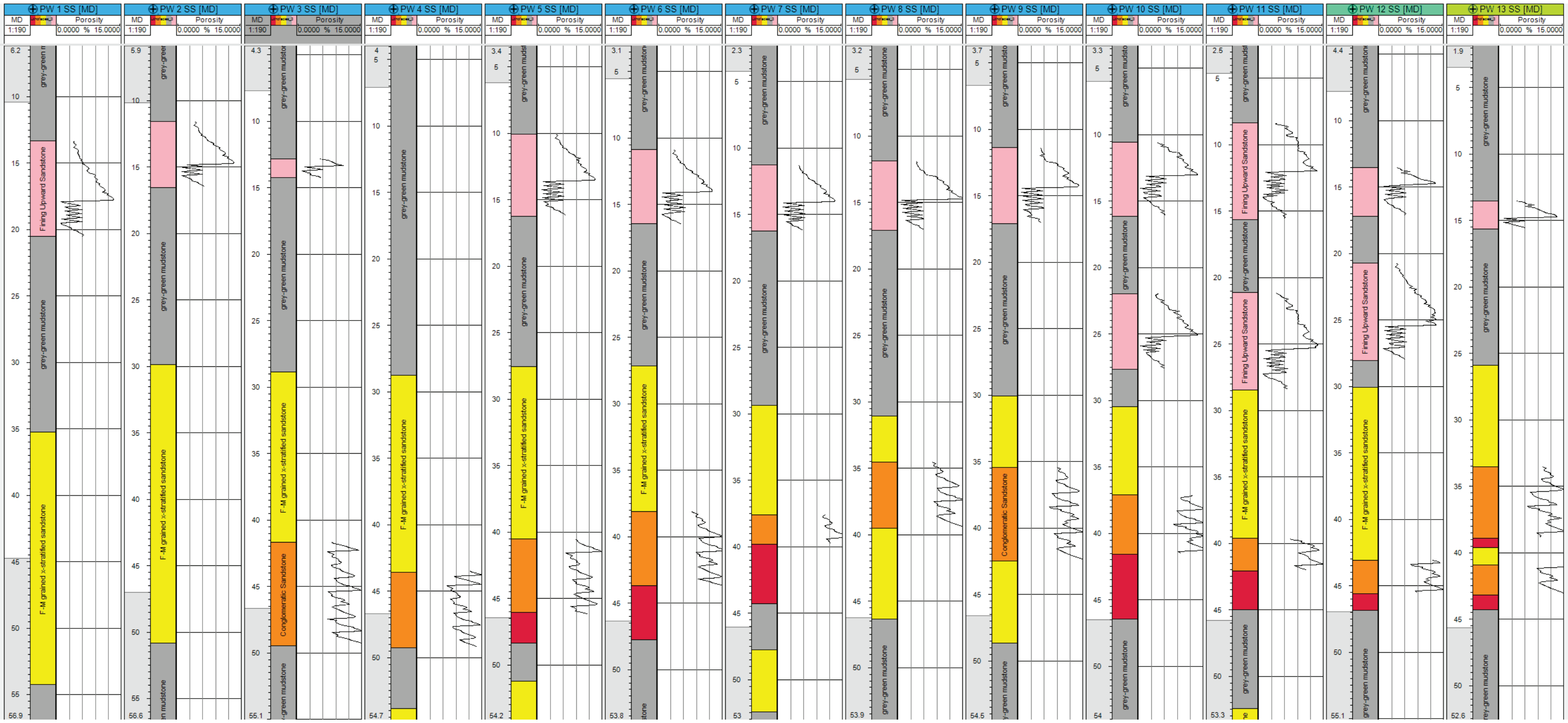

Appendix C-23. Well log cross section for all wells with data in the Burro Canyon Formation. Lithofacies log shown with associated porosity upward-decreasing trends in facies that display upward-fining beds. Well logs were used in zones with multiple cycles of upward-fining beds to constrain porosity models.

APPENDIX D
Fluid-Flow Simulations

Parameters	Value
Sgcr	0.05
Sorw	0.2
Swmin	0.2
Corey gas	6
Sorg	0.2
Swcr	0.22
Krg@Swmin	0.9
Corey O/W	3
Corey water	4
Krg@Sorg	0.8
Corey O/G	3
Krw@Sorw	0.8
Kro@Somax	0.9
Krw@S=1	1

Appendix D-1. Rock and fluid physics parameters used in fluid-flow simulations in Petrel E&P software.

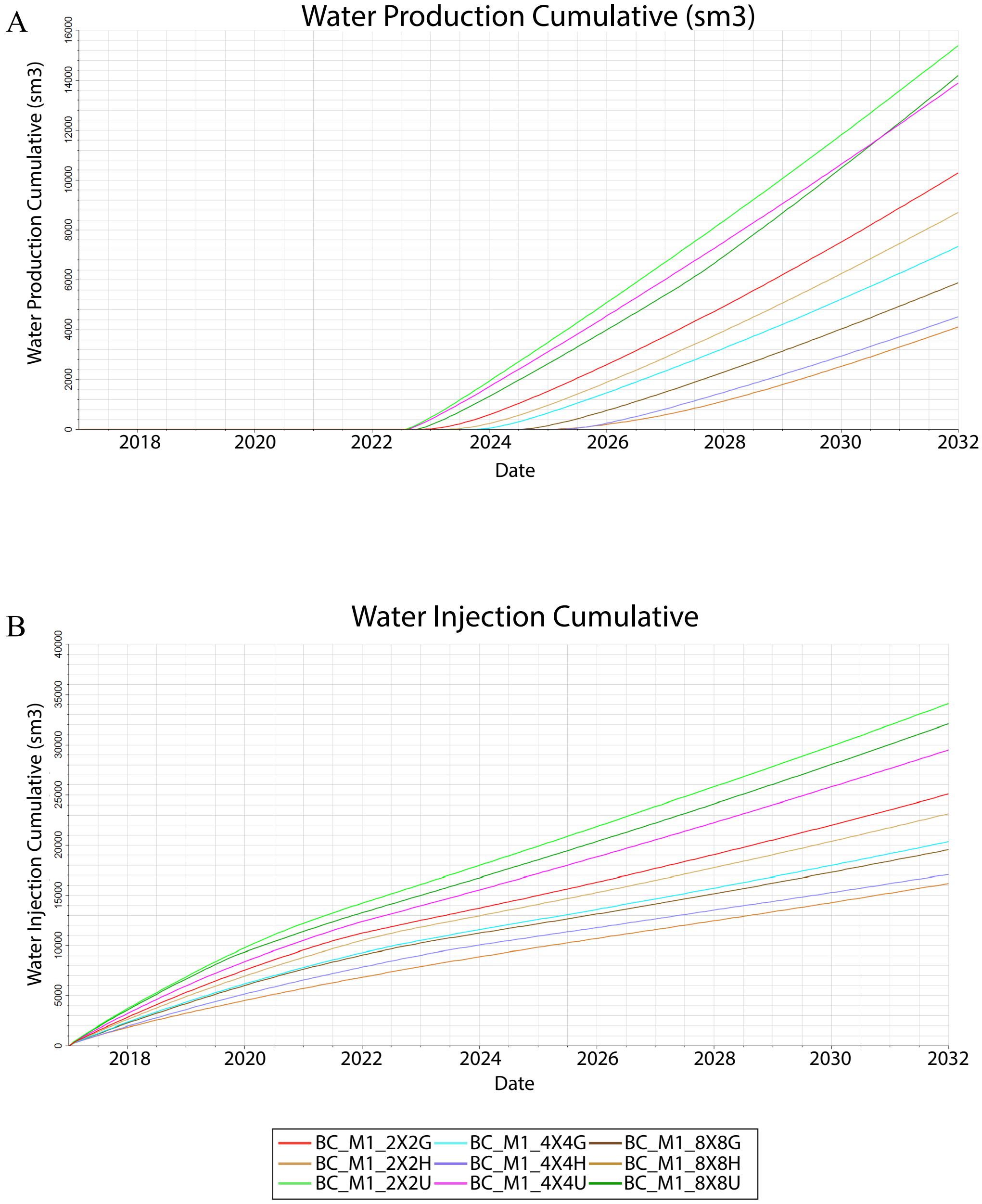

Appendix D-2. Fluid-flow simulation results for Model 1 scenario: (A) cumulative water production.(B) cumulative water injection.

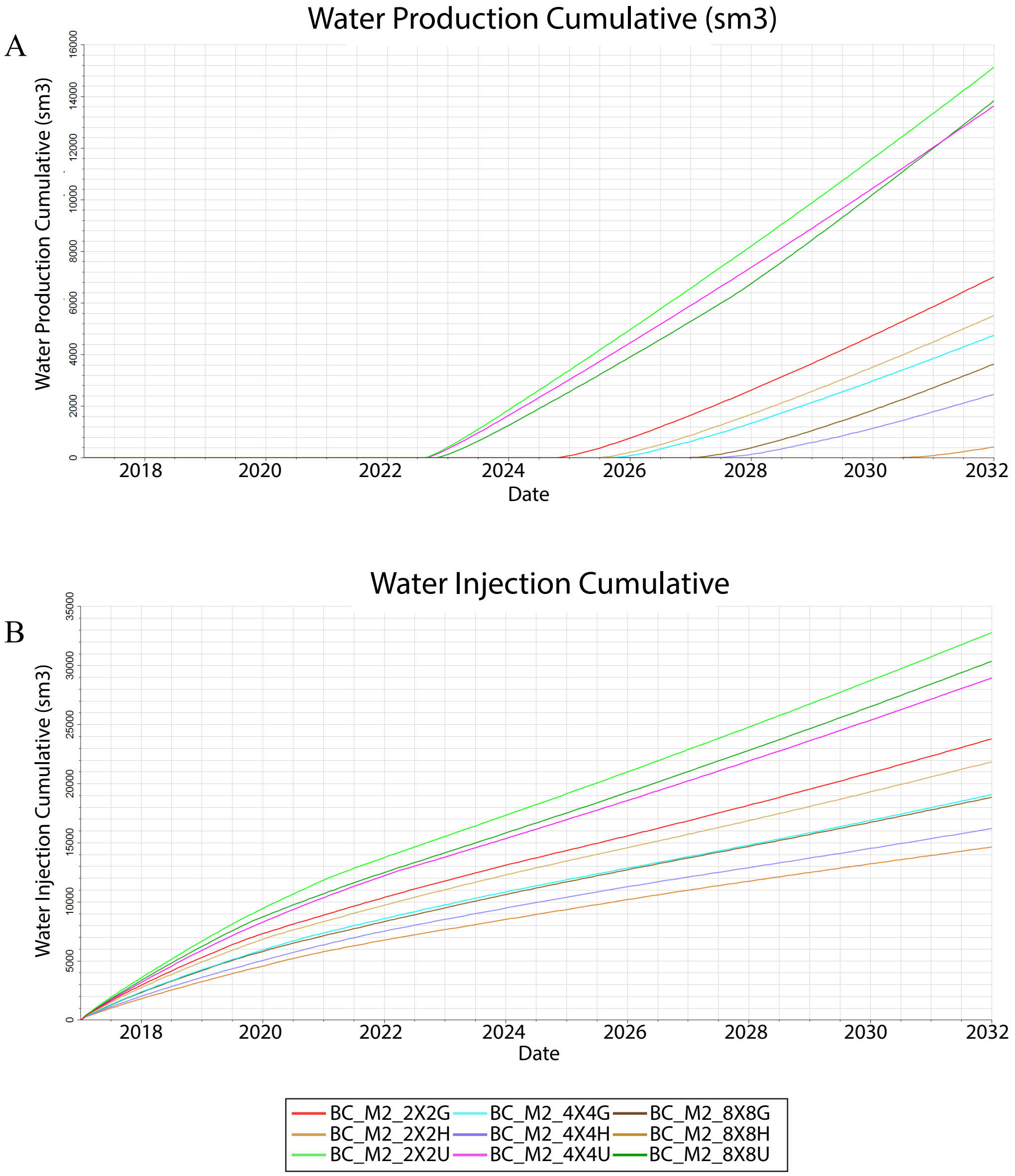

Appendix D-3. Fluid-flow simulation results for Model 2 scenario: (A) cumulative water production.(B) cumulative water injection.

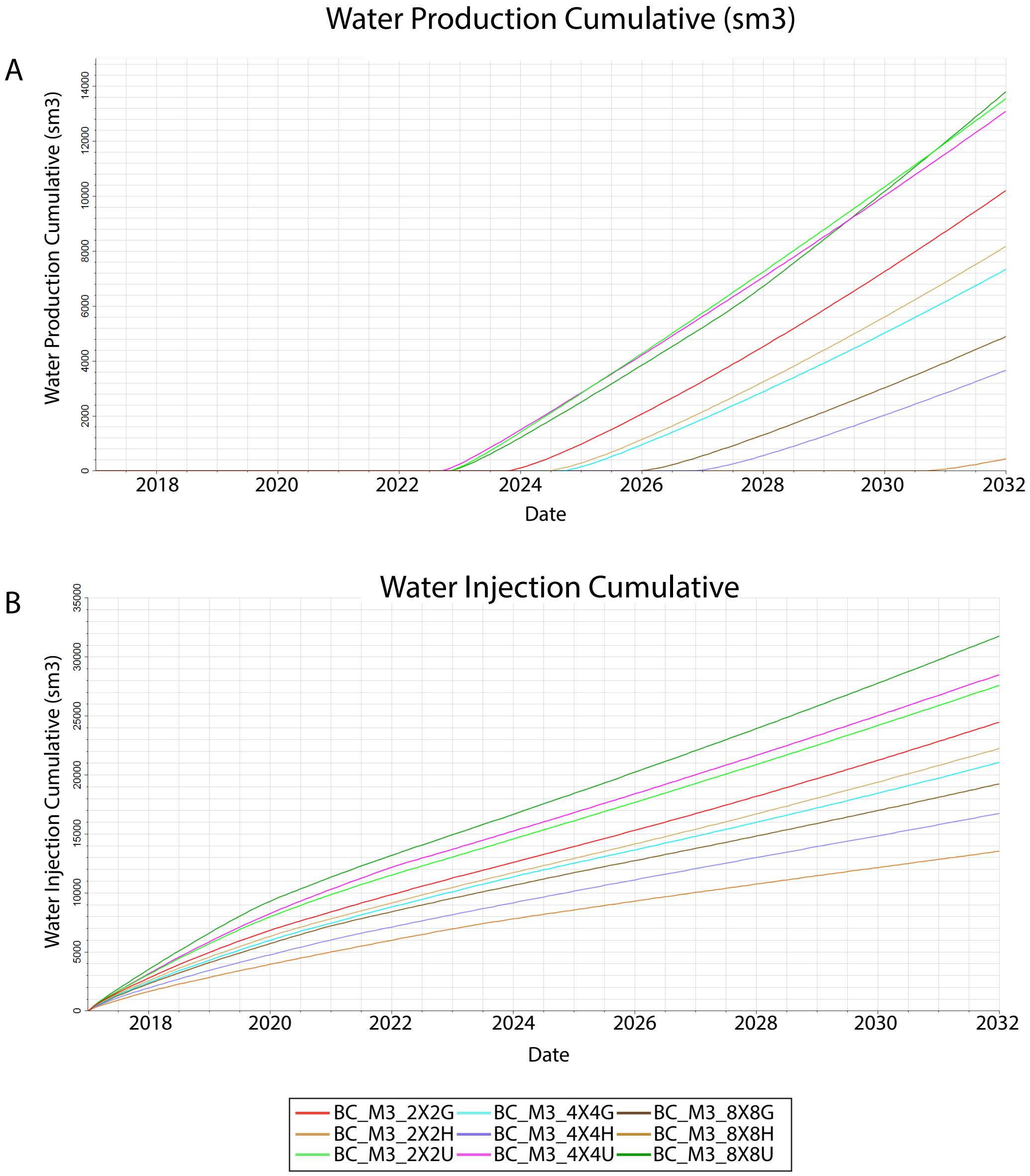

Appendix D-4. Fluid-flow simulation results for Model 3 scenario: (A) cumulative water production.(B) cumulative water injection.

Model Name	Break Through Time (months)	Recovery Efficiency @ BTT	Recovery Efficiency @ 15 years	Volumetric Sweep Efficiency @ BTT
Model 1_2x2_H	71	42.25%	49.11%	58.13%
Model 1_2x2_G	67	43.07%	49.67%	58.38%
Model 1_4x4_H	95	43.04%	47.44%	59.52%
Model 1_4x4_G	78	43.56%	48.80%	60.36%
Model 1_8x8_H	91	37.59%	46.65%	53.58%
Model 1_8x8_G	87	45.21%	49.93%	63.48%
Model 1_2x2_U	66	46.27%	55.42%	69.19%
Model 1_4x4_U	66	45.23%	51.75%	66.59%
Model 1_8x8_U	68	48.24%	57.17%	73.73%
Model 2_2x2_H	94	43.16%	48.40%	60.44%
Model 2_2x2_G	87	43.49%	49.44%	58.69%
Model 2_4x4_H	114	42.42%	46.25%	58.05%
Model 2_4x4_G	96	42.95%	47.23%	58.99%
Model 2_8x8_H	147	44.67%	47.56%	62.53%
Model 2_8x8_G	111	45.21%	50.20%	63.38%
Model 2_2x2_U	67	42.61%	49.24%	62.34%
Model 2_4x4_U	67	42.16%	47.77%	61.82%
Model 2_8x8_U	68	43.29%	50.39%	63.55%
Model 3_2x2_H	87	37.25%	41.22%	52.26%
Model 3_2x2_G	79	37.23%	41.60%	53.28%
Model 3_4x4_H	114	38.40%	41.71%	54.61%
Model 3_4x4_G	90	39.05%	43.12%	56.68%
Model 3_8x8_H	161	41.00%	42.19%	59.70%
Model 3_8x8_G	106	41.08%	44.18%	61.32%
Model 3_2x2_U	69	39.91%	43.21%	54.63%
Model 3_4x4_U	68	41.97%	47.69%	60.82%
Model 3_8x8_U	69	44.76%	52.90%	67.12%

Appendix D-5. Summary of fluid-flow simulation results for each model, grid size, and upscaling method. Model scenario: Model 1, Model 2, Model 3, Grid cell size: 2x2, 4x4, 8x8, upscaling method: H=harmonic mean, G=geometric mean, U=uniform porosity and permeability. Breakthrough time is shown in months, recovery efficiency is shown in percent at breakthrough time and at the end of the 15-year simulation period, and volumetric sweep efficiency is shown in percent at breakthrough time.

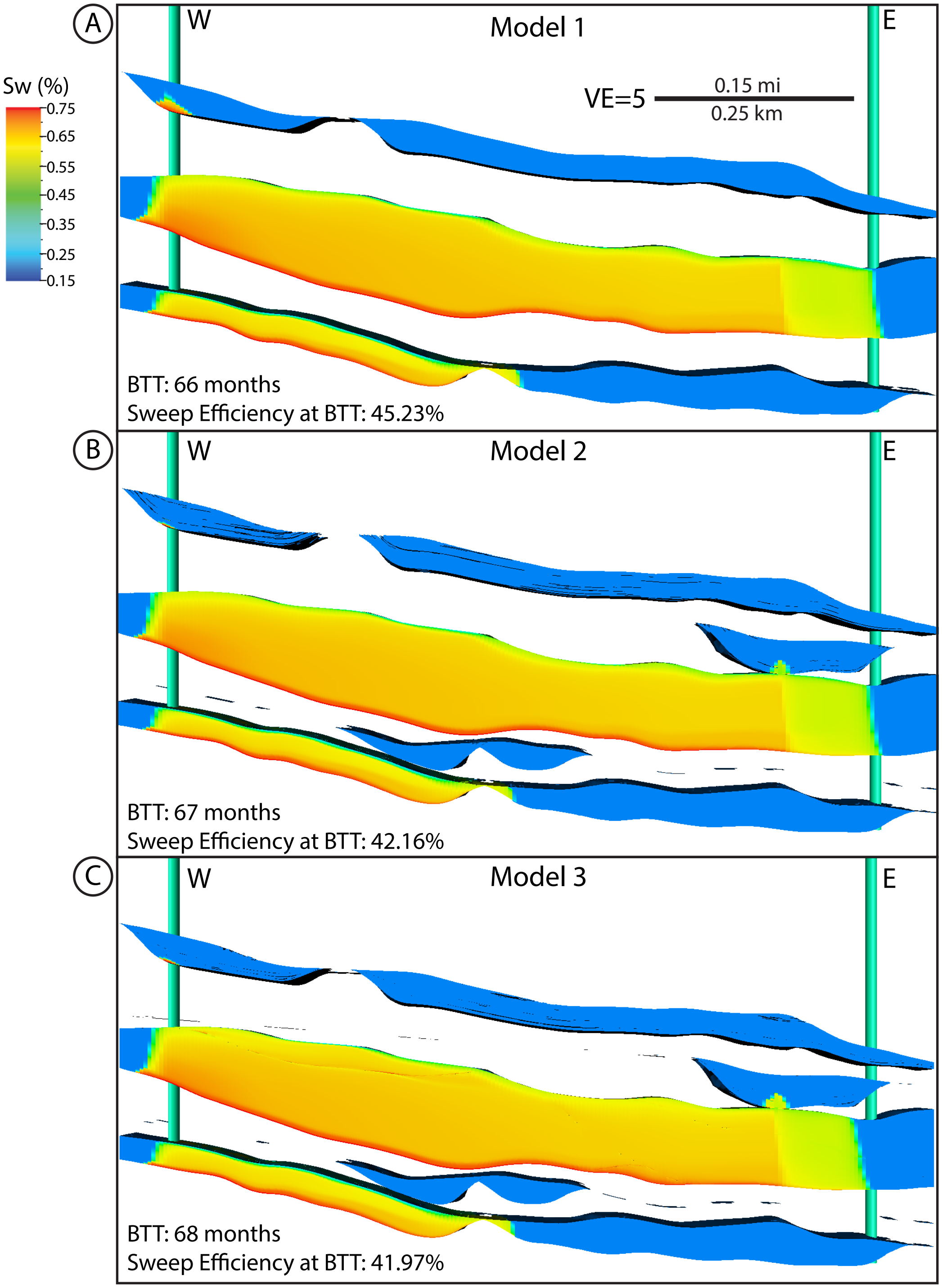

Appendix D-6. Water saturation models for the 4x4-grid simulations for each uniform property model simulation (Models 1-3) (A-C). Uniform property model simulations (models with a single value for porosity and permeability assigned to all reservoir zones) show a piston-like water front moving across the amalgamated channel complex and lower reservoirs. Uniform property model simulations all have similar breakthrough times (66-69 months) because of this movement.

APPENDIX E
Outcrop Field Data

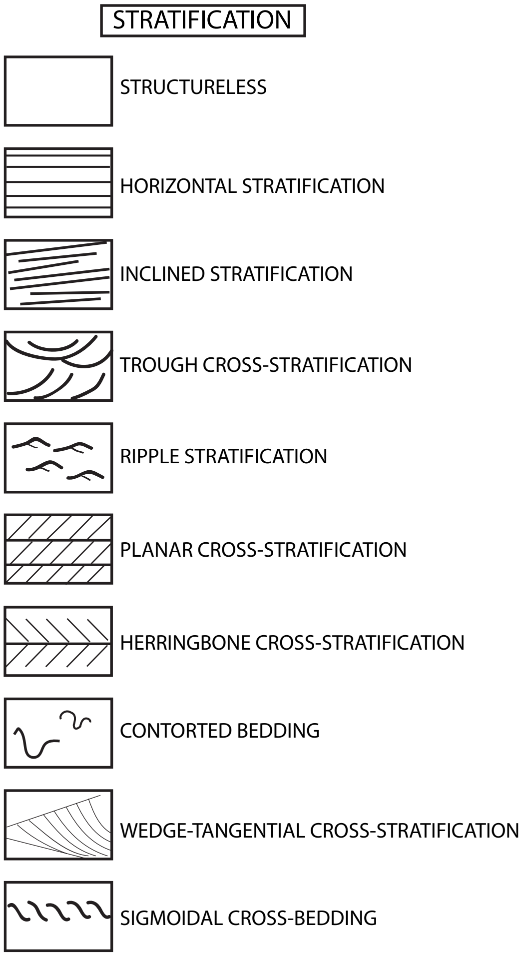

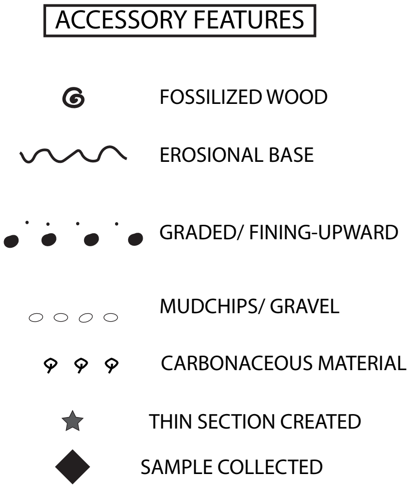

Section: MS 1
Geologist: Sarah Clark

Page 8 of 8
Date: 5-17-16

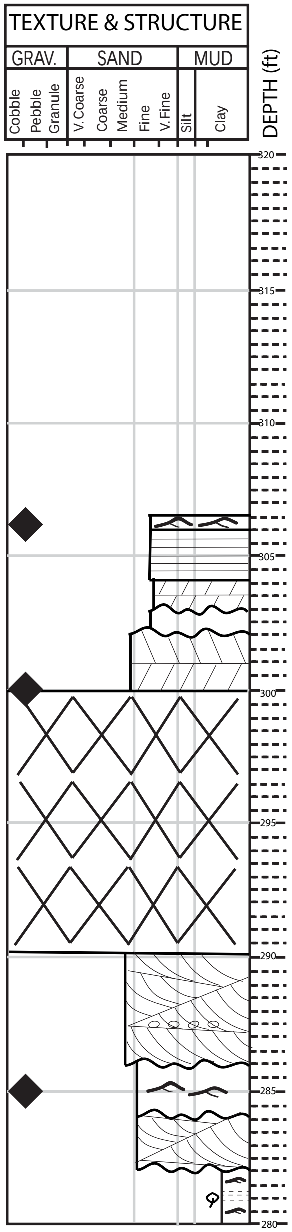

ROCK TYPE	STRATIFICATION	DESCRIPTION
Sandstone	Ripple stratification	Off white, fine grain, quartz cemented, well sorted
Sandstone	Horizontal, planar laminations	Off white, fine grain, well cemented sandstone with black lith. fragments
Sandstone	Tabuler-planar cross-strat.	Off white, fine grain, well cemented sandstone with black lith. fragments
Silty SS	Structureless	Tan, fine-medium grain silty sandstone, not well cemented, heavily weathered
Sandstone	Bidirectional cross-stratification	Tan-light brown, fine-medium grained, moderate sorting, well cemented sandstone with black lith. fragments
Covered section		
Sandstone	Wedge-tangential cross-stratification	Tan, medium grain, well sorted sandstone with some black lith. fragments
Sandstone	Ripple stratification	Tan-grey, fine grained, well sorted sandstone with quartz cement and lith. fragments
Sandstone	Wedge-tangential cross-stratification	Tan-grey, fine grained, well sorted, fissile, not well cemented sandstone with some grey-black lith. fragments
Mudstone	Thinly laminated to ripple-laminated	Dark brown-tan, carbonaceous mudstone interbedded with brown, ripple-laminated silty mudstone

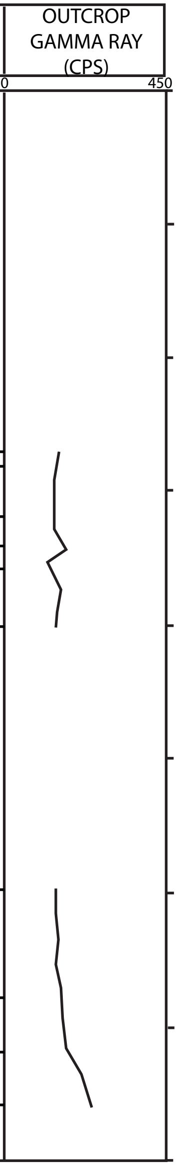

Section: MS 1 Page 7 of 8

Geologist: Sarah Clark Date: 5-17-16

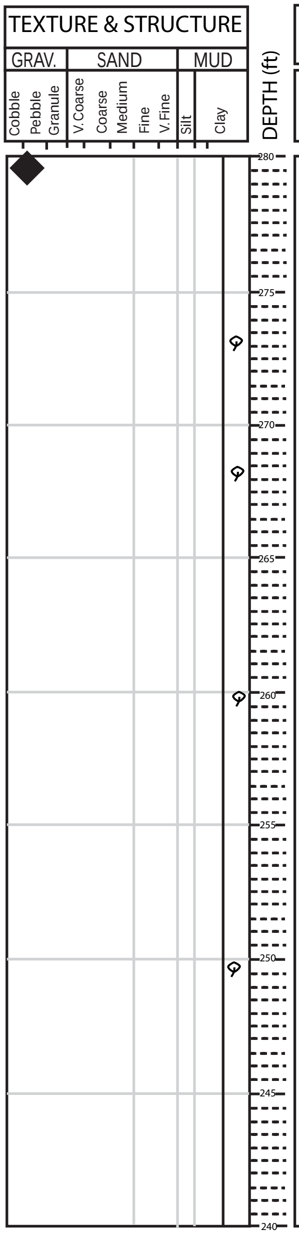

ROCK TYPE	STRATIFICATION	DESCRIPTION	OUTCROP GAMMA RAY (CPS) 0 450
Mudstone	Covered section	Dark grey, unconsolidated, loose carbonaceous mudstone	

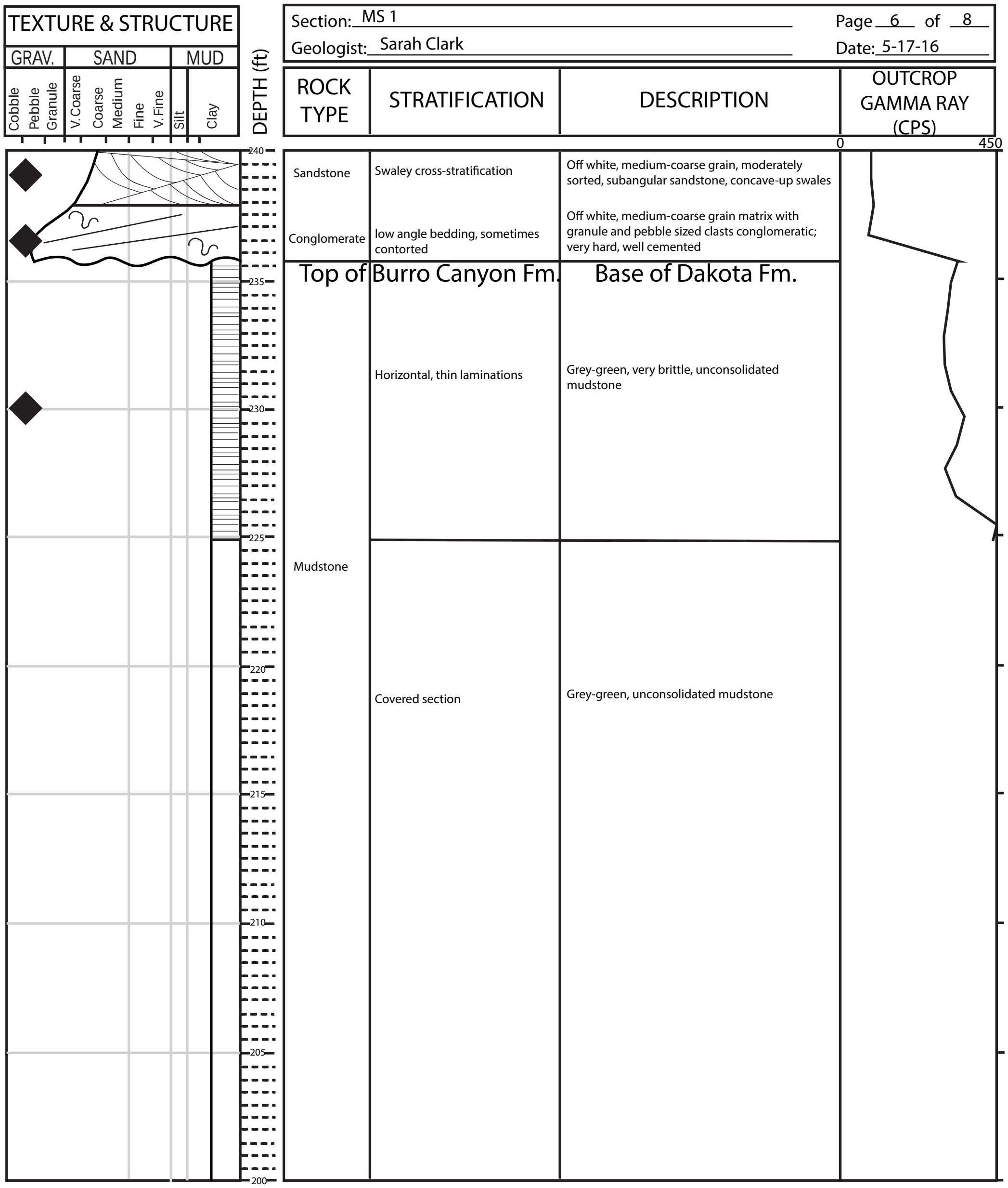

Section: MS 1

Page 6 of 8

Geologist: Sarah Clark

Date: 5-17-16

ROCK TYPE	STRATIFICATION	DESCRIPTION
Sandstone	Swaley cross-stratification	Off white, medium-coarse grain, moderately sorted, subangular sandstone, concave-up swales
Conglomerate	low angle bedding, sometimes contorted	Off white, medium-coarse grain matrix with granule and pebble sized clasts conglomeratic; very hard, well cemented
Top of	Burro Canyon Fm.	Base of Dakota Fm.
Mudstone	Horizontal, thin laminations	Grey-green, very brittle, unconsolidated mudstone
	Covered section	Grey-green, unconsolidated mudstone

Section: MS 1
Page 5 of 8
Geologist: Sarah Clark
Date: 5-17-16

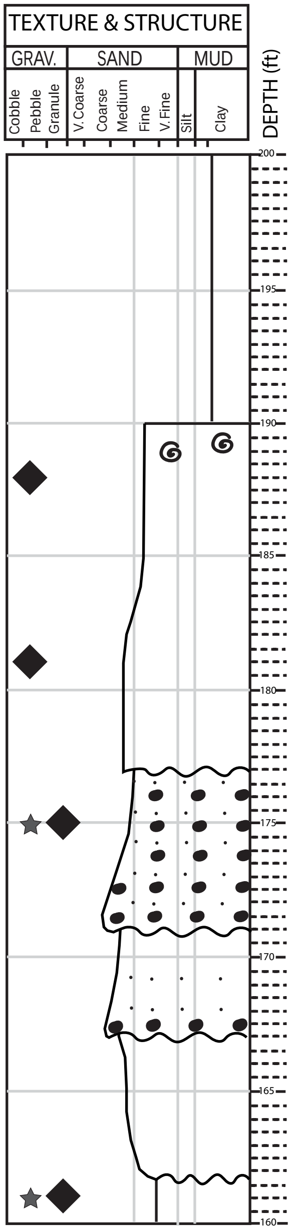

ROCK TYPE	STRATIFICATION	DESCRIPTION
Mudstone	Covered section	Grey-green, unconsolidated mudstone
Sandstone	Structureless, fining upward	Tan- white, fining upward sandstone; medium grain, well sorted with some hematite chips at base and fines into fine-grained, well sorted at top some fossilized wood fragments
Sandstone	Faint inclined bedding, thin fining upward cycles	Tan-white, cycles of coarse grain sand and white subangular gravel at bottom on scour surfaces fining into fine grain, poorly sorted sandstone. Cycles ~.5 ft thick each. Poorly consolidated
Sandstone	Faint inclined bedding, fining upward	Pink-tan, coarse grain sand and subround white and black gravel at base of unit fining upward to medium to coarse grain, poorly sorted sandstone at top
Sandstone	Highly weathered	Pink-tan, medium grain, subround, well sorted, poorly consolidated sandstone
Sandstone	Highly weathered	Pink, fine-medium grain, subangular, well sorted, loosely consolidated sandstone with hematite chips throughout

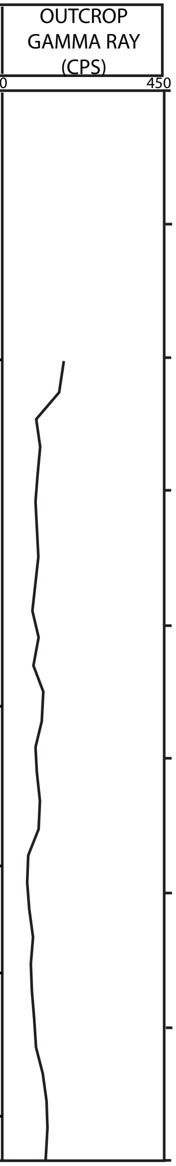

Section: MS 1 Page 4 of 8

Geologist: Sarah Clark Date: 5-17-16

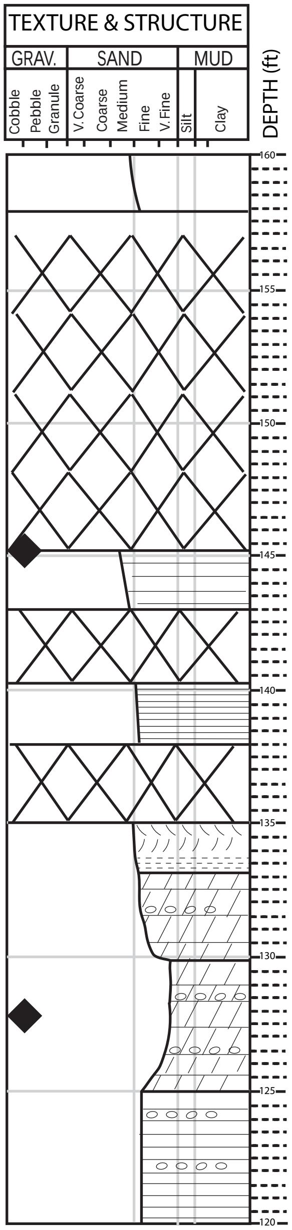

ROCK TYPE	STRATIFICATION	DESCRIPTION
Sandstone	Structureless/ highly weathered	Pink, fine-medium grain, subangular, well sorted, loosely consolidated sandstone with hematite chips throughout
Covered Section		
Sandstone	Horizontal, planar bedding	Tan-green, medium grain, subangular, well sorted sandstone with some hematite chips
Covered Section		
Sandstone	Horizontal, planar laminations	Tan-white, fine-medium grain, moderately well sorted sandstone with some coarse grains and black lith. fragments
Covered Section		
Sandstone	Tabular-tangential cross-stratification to faint horizontal laminations	Off white-tan, medium grains, well sorted sandstone with black lith. fragments
Sandstone	Tabular-planar cross-stratification	White, medium grain, well sorted sandstone with some dark brown-black lith. fragments
Sandstone	Tabular-planar cross-stratification	Tan-white, very fine grain, well sorted sandstone with medium grain black lith. fragments
Sandstone	Horizontal, planar laminations	Tan-white, fine grained, well sorted sandstone with black lith. fragments (coarse grained)

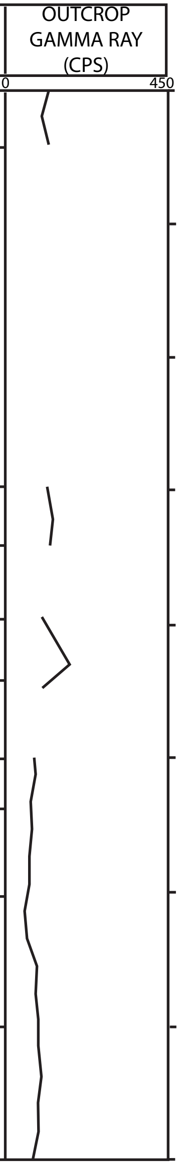

Section: MS 1

Page 3 of 8

Geologist: Sarah Clark

Date: 5-17-16

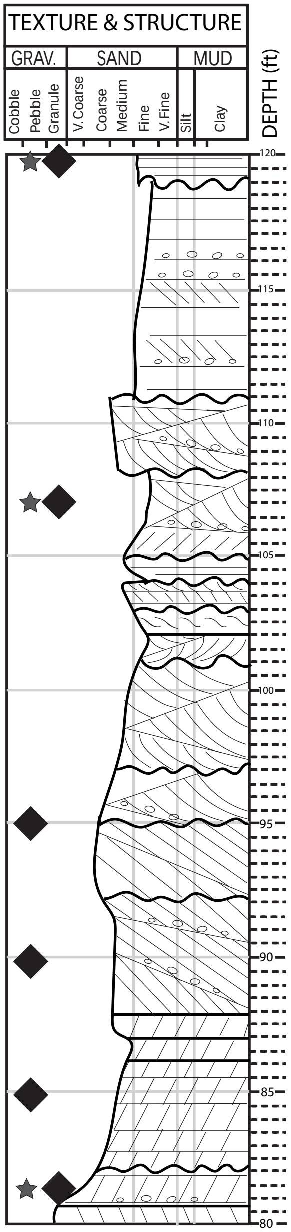

ROCK TYPE	STRATIFICATION	DESCRIPTION
Sandstone	Horizontal, planar laminations	Tan-white, fine grained, well sorted with black lith. fragments
Sandstone	Tabular bedding with some planar foresets	Tan-off white, fine grained, well sorted sandstone with some black granules/pebbles at scour surfaces
Sandstone	Wedge-tangential cross-stratification	Off white-red, coarse grained, well sorted sandstone with some rounded pebbles lining scour surfaces
Sandstone	Wedge-planar to tangential cross- stratification	Red-tan, lower-medium grain, well sorted sandstone with some black lith. fragments
Sandstone	Horizontal bedding	Tan- red-brown, upper-fine to medium grain, well sorted sandstone
Sandstone	Tabular- planar to tangential cross-strat.	Tan, upper-medium to coarse grain, well sorted
Sandstone	Tabular- sigmoidal cross-strat.	Red, medium grain, well sorted
Sandstone	Wedge- tangential cross-strat.	Tan, upper-fine grain, well sorted, subround
Sandstone	Wedge- tangential cross-stratification	Tan-off white, graded lower coarse-medium grains, well sorted sandstone; no gravel-sized grains
Sandstone	Wedge-tangential cross-stratification	Tan-grey, subangular, medium-lower coarse grain sandstone, some graded bedding, some gravel at scour surfaces
Sandstone	Wedge-planar cross-stratification	Tan-grey, subangular, coarse-very coarse grain sandstone
Sandstone	Wedge-planar cross-stratification	Tan-grey, poorly sorted, upper medium-coarse grain sand matrix, with very coarse- pebble grains concentrated along scour surfaces. Gravel is mostly subround, sand-sized grains are subangular
SS & Congl. SS	Tabular-planar cross-stratification low angle	Tan-red, medium to coarse grain, poorly sorted sandstone with gravel lenses
Conglomeratic Sandstone	Tabular-planar cross-stratification low angle	Tan-red, very course grain sandstone with white, tan, and grey, subround clasts ~1-3 cm. Granule and pebble sized clasts aligned with bedding planes, some gravel lenses
Sandstone	Tabular-planar cross-stratification low angle	Tan-red, med. grain, mod. sorted with very coarse, angular grains aligned with base of beds
Conglomerate	See below	

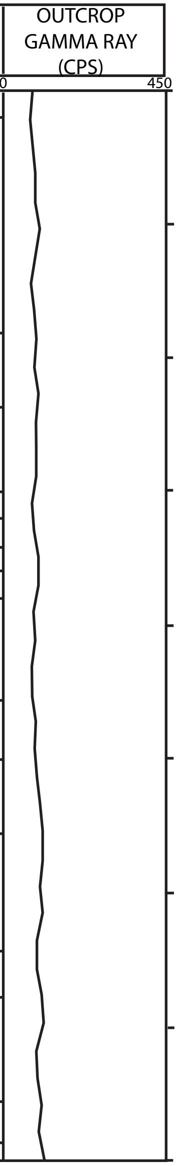

Section: MS 1

Geologist: Sarah Clark

Page 2 of 8

Date: 5-17-16

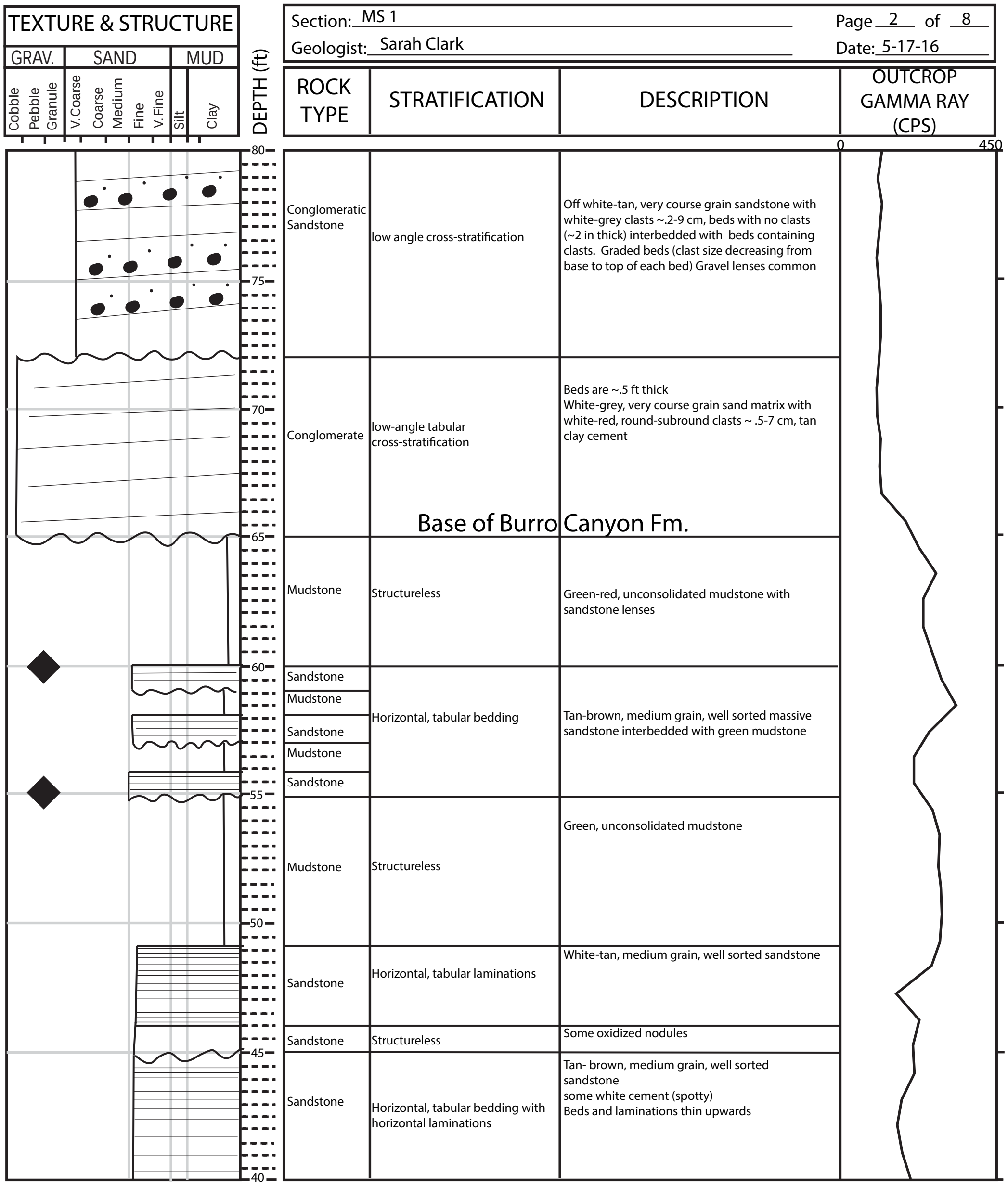

ROCK TYPE	STRATIFICATION	DESCRIPTION
Conglomeratic Sandstone	low angle cross-stratification	Off white-tan, very course grain sandstone with white-grey clasts ~.2-9 cm, beds with no clasts (~2 in thick) interbedded with beds containing clasts. Graded beds (clast size decreasing from base to top of each bed) Gravel lenses common
Conglomerate	low-angle tabular cross-stratification	Beds are ~.5 ft thick White-grey, very course grain sand matrix with white-red, round-subround clasts ~ .5-7 cm, tan clay cement
Mudstone	Structureless	Green-red, unconsolidated mudstone with sandstone lenses
Sandstone Mudstone Sandstone Mudstone Sandstone	Horizontal, tabular bedding	Tan-brown, medium grain, well sorted massive sandstone interbedded with green mudstone
Mudstone	Structureless	Green, unconsolidated mudstone
Sandstone	Horizontal, tabular laminations	White-tan, medium grain, well sorted sandstone
Sandstone	Structureless	Some oxidized nodules
Sandstone	Horizontal, tabular bedding with horizontal laminations	Tan- brown, medium grain, well sorted sandstone some white cement (spotty) Beds and laminations thin upwards

Base of Burro Canyon Fm.

Section: MS 1 Page 1 of 8
Geologist: Sarah Clark Date: 5-17-16

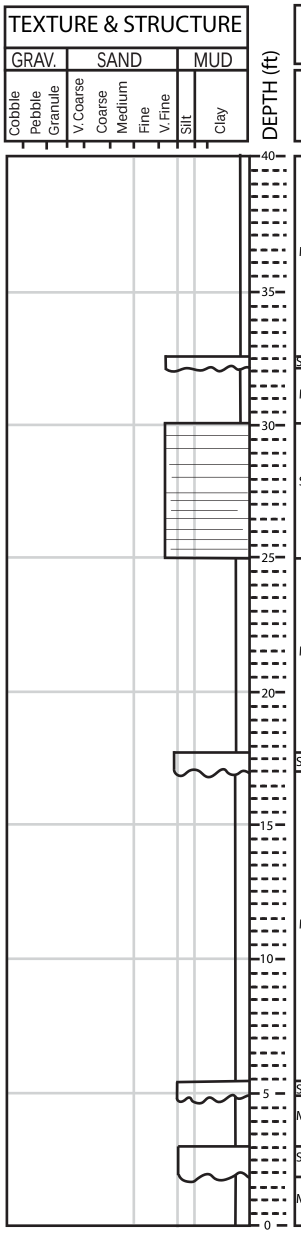

ROCK TYPE	STRATIFICATION	DESCRIPTION
Mudstone	Structureless	Green, unconsolidated mudstone
Sandstone		
Mudstone	Structureless	Green, unconsolidated mudstone
Sandstone	Horizontal, planar bedding	.5-1 ft thick beds Green-grey, v.f. grain, massive beds; beds thicken upward
Mudstone	Structureless	Green, unconsolidated mudstone
Silty SS	Structureless	Green-grey, v.f. grained, crystalline cemented, silty sandstone
Mudstone	Structureless	Green, unconsolidated mudstone
Silty SS	Structureless	
Mudstone	Non-Stratified	Green, unconsolidated mudstone
Silty SS	Structureless	Green-grey, very fine grained, crystalline cemented, silty sandstone
Mudstone	Non-Stratified	Green, unconsolidated mudstone

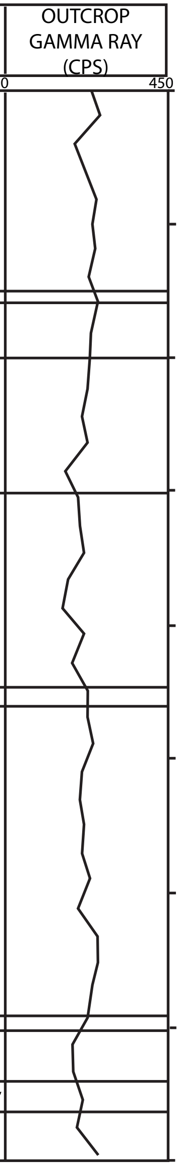

Section: MS 2
Page 6 of 6
Geologist: Sarah Clark
Date: 5-17-16

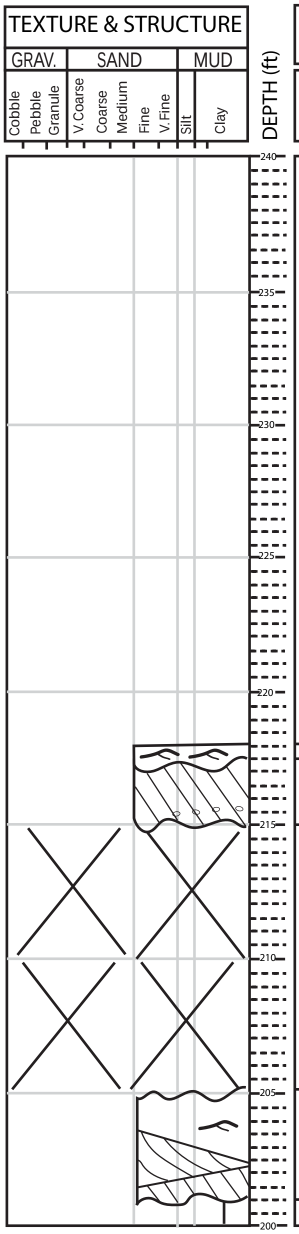

ROCK TYPE	STRATIFICATION	DESCRIPTION	GAMMA RAY
Sandstone	Ripple stratification	See below, no lithic fragments	
Sandstone & Coal	Tabular-planar cross-stratification	Tan-off white, fine grained, well sorted, quartz cemented sandstone, increasing lithic fragment content upwards with coal stringers throughout	
Covered Section			
Sandstone	Wedge-tabular to tangential cross-stratification, possible ripples	Tan-off white, fine grained, well sorted, quartz cemented sandstone	
Mudstone	Structureless	Dark grey-black, fissile, carbonaceous mudstone	

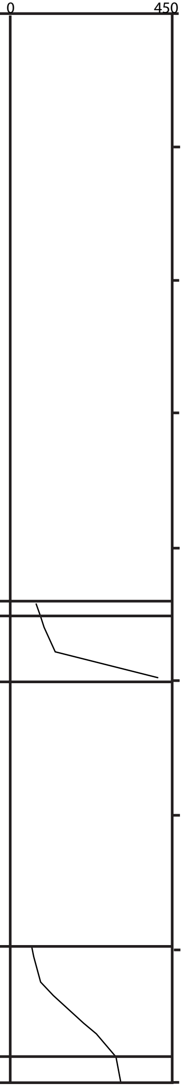

Section: MS 2 Page 5 of 6

Geologist: Sarah Clark Date: 5-17-16

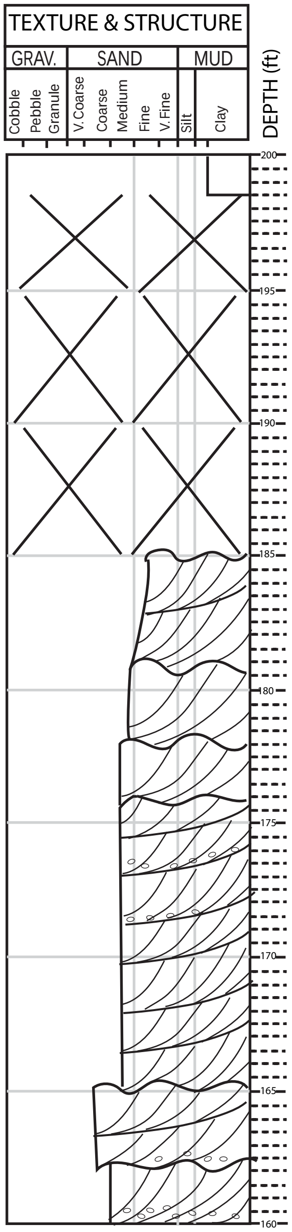

ROCK TYPE	STRATIFICATION	DESCRIPTION
Mudstone	Structureless	Dark grey-black, carbonaceous mudstone
Covered Section		
Sandstone	Trough-tangential cross-stratification	White-tan, fine-medium, subround, moderately sorted sandstone, few white-black lithic fragments throughout
Sandstone	Trough-tangential cross-stratification	White-tan, medium, subround, well sorted sandstone, few lithic fragments throughout
Sandstone	Trough-tangential cross-stratification	White-tan, medium-coarse, subangular, good sorting sandstone, common white-black lithic fragments
Sandstone	Trough-tangential cross-stratification	White-tan, medium, subangular, well sorted sandstone. Lithic fragments absent in lower section, but become common in top 5 ft of section
Sandstone	Trough-tangential cross-stratification	White-tan, coarse, subangular, well sorted sandstone. Few white-black, coarse-granule sized lithics
Sandstone	Trough-tangential cross-stratification	White-tan, medium-coarse, subangular, moderately sorted sandstone. Abundant white-black, coarse-granule sized lithics

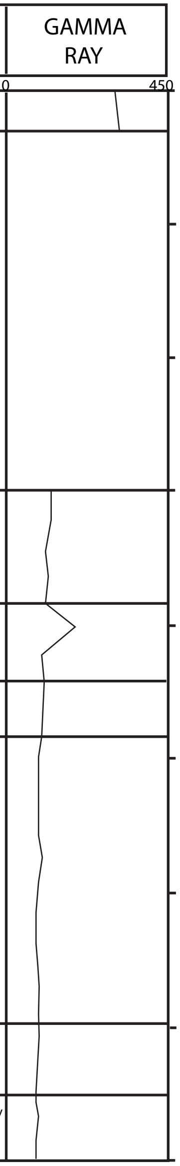

Section: MS 2
Page 4 of 6
Geologist: Sarah Clark
Date: 5-17-16

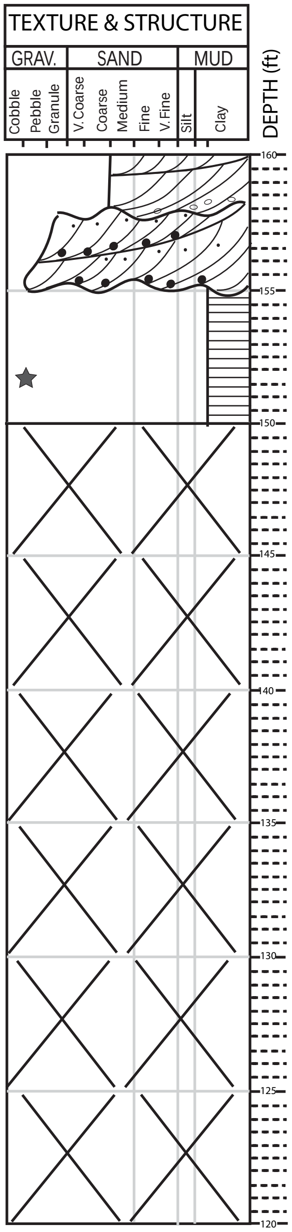

ROCK TYPE	STRATIFICATION	DESCRIPTION	GAMMA RAY
Sandstone	Trough-tangential cross-stratification	White-tan, medium-coarse grained, subangular, poorly sorted sandstone with common white-tan medium-coarse grained lithic fragments	
Conglomeratic Sandstone	Trough-tangential cross-stratification	Off white, grading conglomeratic sandstone. 20% white-black, granule- pebble sized, subround, elongate clasts in medium-coarse grained sand matrix. Clasts fine upward.	
Top Burro Canyon Fm./ Base Dakota Fm.			
Mudstone	Horizontal, planar laminations	Grey-green, brittle, silicified mudstone	
Covered Section			

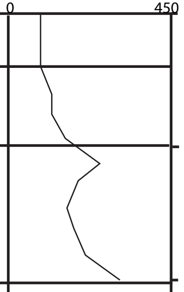

Section: MS 2

Geologist: Sarah Clark

Page 3 of 6

Date: 5-17-16

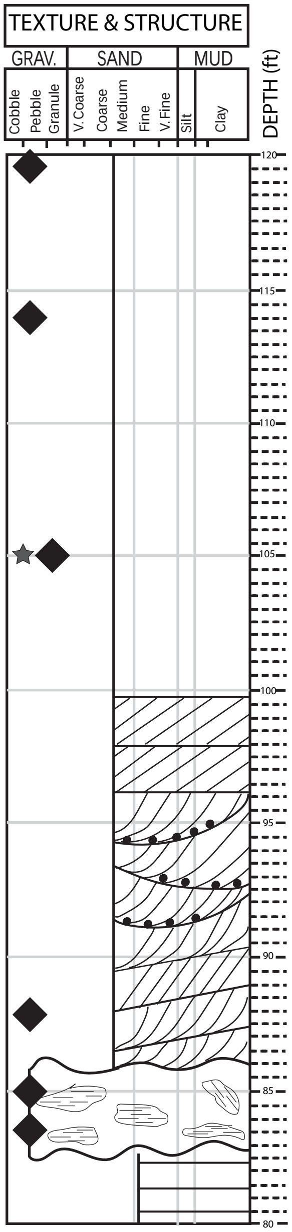

ROCK TYPE	STRATIFICATION	DESCRIPTION
Sandstone	Weathering has removed surficial stratification	Tan-off white, medium grained, well cemented sandstone Heavily weathered
Sandstone	Trough-tangential to tabular -planar towards top cross-stratification	Tan-off white, upper-fine to lower-medium grained, subangular, moderately sorted sandstone, pebble lag along trough bases
Sandstone	Complex (inclined tabular-tangential & planar) cross-stratification	Tan-white, medium to coarse grained, subround-subangular, poorly sorted sandstone, with white-black, coarse-granule sized, subangular lithic clasts. Lithic content decreases upwards in section with rounded pebble-sized clasts common in upper section
Conglomerate	Structureless with suspended large mudstone clasts	White-tan, very hard conglomerate with 40% pebble-sized, subangular clasts and fine-coarse grained, poorly sorted sand matrix. Suspended mudstone (ripup) clast clusters throughout
Sandstone	Horizontal, planar bedding	Off white, fine grained, subangular, well sorted sandstone, with some white, fine grained, subangular lithic clasts

GAMMA RAY

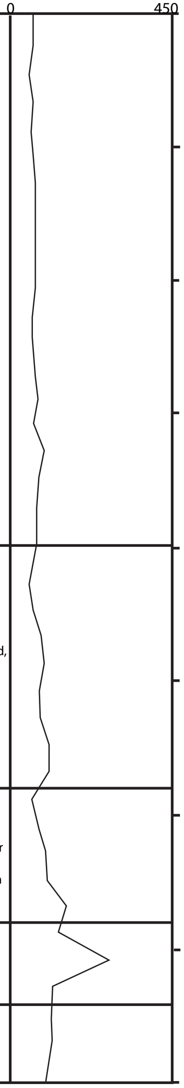

Section: MS 2 Page 2 of 6

Geologist: Sarah Clark Date: 5-17-16

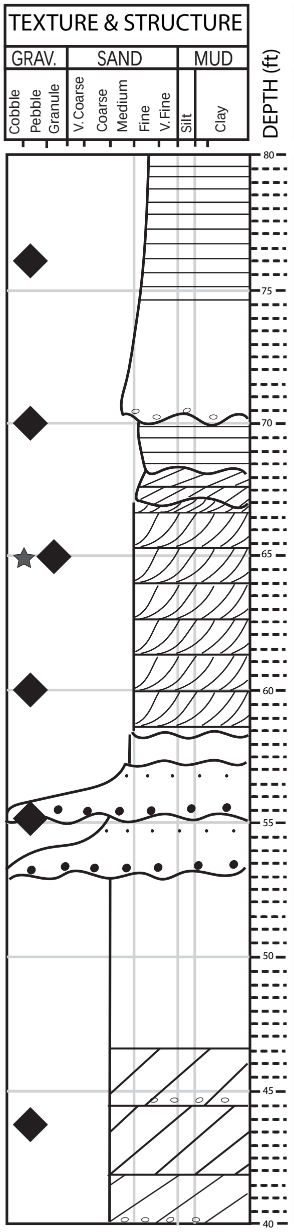

ROCK TYPE	STRATIFICATION	DESCRIPTION
Sandstone	Horizontal, planar bedding Structureless	White-red/ tan weathering, fine grained , subangular to subround, well-sorted sandstone, very hard- quartz cement? White-red/ tan weathering, medium grained , subround, moderately-sorted sandstone, some black/white lithic fragments
Sandstone	Horizontal, planar bedding	White-off white, upper fine-lower medium, subround, well-sorted, clean sandstone
Sandstone	Tabular-planar cross-stratification	White-tan, fine grained, clean, well-sorted, subround sandstone
Sandstone	Tabular-tangential cross-stratification	White-tan, upper fine-lower medium, clean, subround, good sorting, soft- clay cement?
Sandstone	Structureless	White-grey, medium grained, moderately sorted, subangular sandstone with some lithic fragments
Congl. SS Conglomerate Congl. SS Conglomerate	Structureless/ grading upward	White-tan, very fine-lower very coarse sandstone, very poorly sorted with cobble-sized clast conglomerate grades up to conglomeratic sandstone with medium-coarse sand and granule-sized clasts (<1 cm). Cycles of graded beds ~4 ft thick
Sandstone	Structureless Faint/ less distinct bedding Tabular-planar cross-stratification	Tan-off white, fine-medium grain, with subangular -angular, coarse-very coarse, white lithic fragments. Lithics oriented parallel to laminations in lower section and become more random and mixed in the upper section. Some rounded, pebble-sized clasts throughout.

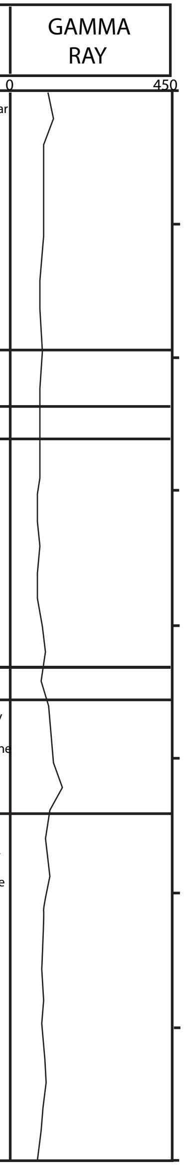

Section: MS 2 Page 1 of 6

Geologist: Sarah Clark Date: 5-17-16

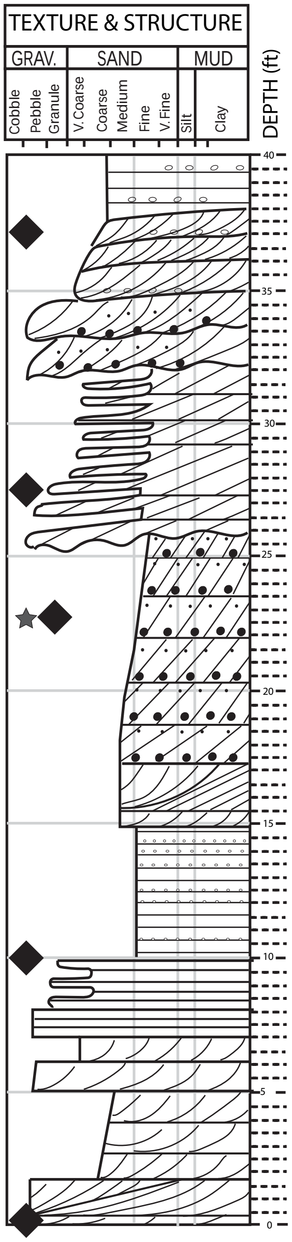

ROCK TYPE	STRATIFICATION	DESCRIPTION	GAMMA RAY
Sandstone	Horizontal, planar bedding	White-off white, medium-coarse grained, subangular sandstone with clay cements. Laminations of med-v. coarse white lithic fragments	
Interbedded SS & Congl. SS Conglomerate	Tabular-tangential cross-stratification	Basal conglomerate grading into interbedded congl. sandstone and sandstone. SS- fine-med. grain, w/ some angular lithics Congl. SS- med.-coarse grained sand with coarse-pebble -sized clasts Conglomerate cycles fine up in ~1 ft cycles	
Interbedded SS & Conglomerate	Tabular-planar cross-stratification	White-tan interbedded sandstone and conglomerate SS- very coarse grained with subangular medium lithic fragments fining upward to fine -medium grained sandstone Conglomerate- ~40% white, rounded <1 cm granual -sized clasts with coarse grained sand	
Sandstone	Tabular-planar cross-stratification	White-off white fining, and ~2-4 in graded cycles. Medium grain, clean, subround, well sorted sandstone with medium sand and very coarse- pebble sized clasts along base of cycles. Section fines upward to fine-grained sandstone	
Sandstone	Complex (trough-tangential & planar) cross-stratification	White, medium grained, subround, well sorted sand with very coarse grained- pebble sized tan-white clasts (3-4 cm) lining basal scour surfaces	
Sandstone	Horizontal, planar laminations (1 in thick)	White, fine-medium grained, subround, well sorted sand with very coarse-granule sized tan-white clasts (<3 cm) lining basal scour surfaces	
Interbedded SS & Congl. SS	Horizontal, planar bedding	White-tan interbedded Congl. SS and SS. Coarse, subangular SS with some vC grained lithic fragments. Cong SS- vC, subangular sand with 40% 1-2 cm granules	
Conglomerate	See above	White-tan conglomerate, 60% 2-3 cm clasts, med. sand	
Congl. SS Conglomerate	Tabular-trough cross-stratification	White-tan conglomerate grading into cong. SS. Coarse grained sand with very coarse-granule/ pebble clasts (white, tan, red)	
Interbedded SS & Congl. SS	Tabular-tangential cross-stratification	White-tan interbedded sandstone and conglomeratic sandstone. Medium-coarse, subangular sand with some lithics throughout. <3 cm grey-white, rounded clasts	
Conglomerate	Wedge-tangential cross-stratification	White-tan conglomerate, coarse grained, subangular, well-sorted sand, with some lithic fragments and 80% <4 cm subround clasts (grey, tan, white)	

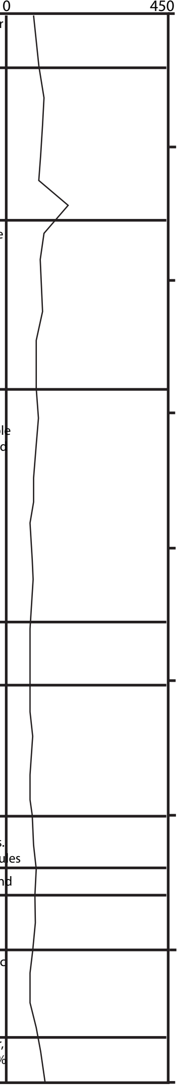

Dip Direction	Dip (degrees)	Location
35.8	3.5	MS 1
107.9	2.4	MS 1
68.0	8.5	MS 1
81.8	15.2	MS 1
81.6	15.2	MS 1
326.0	2.3	MS 1
339.6	1.6	MS 1
145.0	61.2	MS 1
10.0	32.2	MS 1
343.3	21.9	MS 1
36.0	11.3	MS 1
13.0	12.2	MS 1
359.5	16.4	MS 1
58.8	10.5	MS 1
66.7	20.0	MS 1
58.9	20.5	MS 1
354.6	11.4	MS 1
46.3	16.3	MS 1
36.6	7.4	MS 1
108.3	4.3	MS 1
62.1	13.2	MS 1
50.4	14.2	MS 1
7.2	9.8	MS 1
130.6	15.4	MS 1
141.5	6.8	MS 1
55.0	2.4	MS 1
71.5	6.7	MS 1
11.6	34.0	MS 1
336.6	17.1	MS 1
279.2	13.2	MS 1
295.1	13.4	MS 1
339.8	18.7	MS 1
343.0	28.1	MS 1
321.5	30.6	MS 1
324.7	24.8	MS 1
48.1	20.9	MS 1
48.7	19.3	MS 1
50.0	20.5	MS 1
49.0	6.4	MS 1
42.0	23.7	MS 1
15.1	31.5	MS 1
26.0	24.8	MS 1
32.7	22.8	MS 1
42.4	34.1	MS 1

Appendix E-1. Paleocurrent measurements taken along Measured Sections 1 and 2.

Dip Direction	Dip (degrees)	Location
11.4	3.2	MS 1
146.4	9.1	MS 1
45.6	28.0	MS 1
25.4	20.8	MS 1
5.2	17.3	MS 1
41.0	17.3	MS 1
24.5	28.3	MS 1
36.5	21.7	MS 1
13.2	33.9	MS 1
155	25	MS 1
50	24	MS 1
42	19	MS 1
60	14	MS 1
41	11	MS 1
54	6	MS 1
60	27	MS 1
1	9	MS 1
60	5	MS 1
6	15	MS 1
8	19	MS 1
35	28	MS 1
44	14	MS 1
206	12	MS 1
224	20	MS 1
25	6	MS 1
25	12	MS 1
41	13	MS 1
63	2	MS 1
74	10	MS 1
22	14	MS 1
5	4	MS 1
336	20	MS 1
33	4	MS 1
4	21	MS 1
9	11	MS 1
55	4	MS 1
50	26	MS 1
340	6	MS 1
39	34	MS 1
16	5	MS 1
34	5	MS 1
30	20	MS 1
21	5	MS 2
90	14	MS 2

Appendix E-1. Paleocurrent measurements taken along Measured Sections 1 and 2.

Dip Direction	Dip (degrees)	Location
15	21	MS 2
52	20	MS 2
66	19	MS 2
58	22	MS 2
31	16	MS 2
65	10	MS 2
72	30	MS 2
94	24	MS 2
84	2	MS 2
36	12	MS 2
10	5	MS 2
32	15	MS 2
46	15	MS 2
19	11	MS 2
51	17	MS 2
16	14	MS 2
80	15	MS 2
68	25	MS 2
10	20	MS 2
28	8	MS 2
45	20	MS 2
47	15	MS 2
50	16	MS 2
2	19	MS 2
90	14	MS 2
35	10	MS 2
352	80	MS 2
51	80	MS 2
44	40	MS 2
55	60	MS 2
43	40	MS 2

Appendix E-1. Paleocurrent measurements taken along Measured Sections 1 and 2.

Thin section ID	Measured Section	Location in MS (ft)	Lithofacies	Used in Figure 7
2_81	1	81	conglomerate	Figure 7F
2_107	1	107	cross-bedded sandstone	
2_120	1	120	planar laminated sandstone	
2_161	1	161	fining-upward sandstone	Figure 7I
2_175	1	175	fining-upward sandstone	
3_23	2	23	conglomeratic sandstone	Figure 7G
3_65	2	65	cross-bedded sandstone	
3_105	2	105	cross-bedded sandstone	Figure 7H
3_A	2	152	grey-green mudstone	Figure 7J

Appendix E-2. List of thin sections created from samples taken along measured sections 1 and 2. Thin sections used in Figure 7 are indicated.

GPS Waypoint	Latitude	Longitude	Altitude
1	38.766065	-108.245291	1528.5
2	38.766088	-108.245308	1530.3
3	38.766221	-108.245101	1530.2
4	38.766210	-108.245098	1532.2
5	38.766344	-108.244930	1526.5
6	38.766501	-108.244701	1539.2
7	38.766565	-108.244575	1539.0
8	38.766592	-108.244566	1539.0
9	38.767199	-108.243273	1543.8
10	38.767233	-108.243314	1544.0
11	38.767255	-108.243349	1546.1
12	38.767762	-108.243049	1543.0
13	38.767771	-108.243072	1544.1
14	38.767881	-108.243060	1545.2
15	38.767880	-108.243036	1546.1
16	38.768266	-108.242986	1563.4
17	38.768082	-108.242988	1565.7
18	38.767974	-108.243042	1561.3
19	38.767930	-108.243011	1559.7
20	38.768001	-108.243092	1560.5
21	38.768000	-108.242970	1560.4
22	38.768071	-108.243040	1563.1
23	38.768049	-108.243052	1564.1
24	38.768072	-108.243113	1566.7
25	38.768078	-108.243094	1566.7
26	38.768067	-108.243193	1565.9
27	38.768082	-108.243229	1568.1
28	38.768102	-108.243255	1570.0
29	38.768121	-108.243283	1572.3
30	38.768203	-108.243317	1570.2
31	38.768192	-108.243340	1571.0
32	38.768197	-108.243329	1572.7
33	38.768129	-108.243389	1573.1
34	38.768149	-108.243381	1574.2
35	38.768150	-108.243398	1575.4
36	38.767713	-108.243702	1579.0
37	38.767699	-108.243732	1580.2
38	38.767729	-108.243755	1582.3
39	38.767738	-108.243782	1582.8
40	38.767743	-108.243804	1584.6

Appendix E-3. GPS waypoints collected along Measured Section 1 traverse along the west side of 650 Road in Escalante Canyon.

GPS Waypoint	Latitude	Longitude	Altitude
41	38.767767	-108.243829	1584.8
42	38.767754	-108.243836	1586.0
43	38.767766	-108.243861	1586.9
44	38.767761	-108.243863	1588.3
45	38.767772	-108.243908	1590.2
46	38.767771	-108.243925	1591.3
47	38.767773	-108.243955	1592.9
48	38.767779	-108.244007	1594.7
49	38.767769	-108.244122	1596.0
50	38.767774	-108.244219	1597.9
51	38.767798	-108.244281	1598.7
52	38.767758	-108.244294	1601.0
53	38.767685	-108.244387	1602.5
54	38.767688	-108.244437	1604.8
55	38.767699	-108.244505	1606.5
56	38.767703	-108.244553	1608.0
57	38.767722	-108.244569	1608.9
58	38.767705	-108.244581	1608.6

Appendix E-3. GPS waypoints collected along Measured Section 1 traverse along the west side of 650 Road in Escalante Canyon.

GPS Waypoint	Latitude	Longitude	Altitude
1	38.767568	-108.24199	1548.1
2	38.767581	-108.241958	1544.8
3	38.767617	-108.241928	1548.9
4	38.76762	-108.241937	1549.8
5	38.767615	-108.241906	1549.9
6	38.767603	-108.241846	1551.5
7	38.767594	-108.241798	1552.6
8	38.767602	-108.241744	1554
9	38.767614	-108.24173	1554.8
10	38.767635	-108.241728	1554.6
11	38.767606	-108.241679	1555.6
12	38.767605	-108.241683	1556.7
13	38.767612	-108.241656	1554.9
14	38.767593	-108.241607	1555.2
15	38.767603	-108.241621	1557.1
16	38.767566	-108.241594	1558.6
17	38.767565	-108.241608	1561.7
18	38.767584	-108.241656	1561.1
19	38.767731	-108.241552	1564.5
20	38.767913	-108.241318	1567.5
21	38.769195	-108.241462	1582.7
22	38.76959	-108.242169	1578.6
23	38.769314	-108.241702	1574.6
24	38.769329	-108.241711	1573.7
25	38.76928	-108.241723	1578.8
26	38.769261	-108.241721	1579.1
27	38.769297	-108.241707	1581.9
28	38.769332	-108.241716	1582.1
29	38.769309	-108.241653	1584.5
30	38.769345	-108.241599	1587.8
31	38.769352	-108.241599	1588.4
32	38.769377	-108.241557	1588.4
33	38.769401	-108.241532	1588.7
34	38.769436	-108.241514	1589.7
35	38.769437	-108.241479	1591.2
36	38.769472	-108.241432	1594.3
37	38.769502	-108.241411	1596.7

Appendix E-4. GPS waypoints collected along Measured Section 2 traverse along the east side of 650 Road in Escalante Canyon.

Dip Direction	Dip (degrees)	Latitude	Longitude	Measured Section #
35.8	3.5	38.76437400	-108.25301388	1
107.9	2.4	38.76437010	-108.25300005	1
68.0	8.5	38.76437010	-108.25300005	1
81.8	15.2	38.76449977	-108.25295965	1
81.6	15.2	38.76791717	-108.25728775	1
326.0	2.3	38.76611324	-108.24498209	1
339.6	1.6	38.76502259	-108.25427318	1
145.0	61.2	38.76504560	-108.25425725	1
10.0	32.2	38.76511575	-108.25425047	1
343.3	21.9	38.76506081	-108.25427930	1
36.0	11.3	38.76515653	-108.25422406	1
13.0	12.2	38.76514429	-108.25418592	1
359.5	16.4	38.76508583	-108.25428123	1
58.8	10.5	38.76510234	-108.25427712	1
66.7	20.0	38.76514676	-108.25428600	1
58.9	20.5	38.76502359	-108.25435817	1
354.6	11.4	38.76505444	-108.25438960	1
46.3	16.3	38.76502234	-108.25415131	1
36.6	7.4	38.76495922	-108.25414125	1
108.3	4.3	38.76495922	-108.25414125	1
62.1	13.2	38.76497322	-108.25415818	1
50.4	14.2	38.76497980	-108.25417134	1
7.2	9.8	38.76497980	-108.25417134	1
130.6	15.4	38.76497573	-108.25414108	1
141.5	6.8	38.76497573	-108.25414108	1
55.0	2.4	38.76500662	-108.25480132	1
71.5	6.7	38.76500662	-108.25480132	1
11.6	34.0	38.76500469	-108.25484642	1
336.6	17.1	38.76502053	-108.25490853	1
279.2	13.2	38.76503554	-108.25497122	1
295.1	13.4	38.76503910	-108.25495924	1
339.8	18.7	38.76497774	-108.25502990	1
343.0	28.1	38.76497389	-108.25499570	1
321.5	30.6	38.76502741	-108.25506100	1
324.7	24.8	38.76514123	-108.25496997	1
48.1	20.9	38.76510875	-108.25512017	1
48.7	19.3	38.76513625	-108.25515001	1
50.0	20.5	38.76508943	-108.25513098	1

Appendix E-5. Summary of latitude and longitude taken for paleocurrent measurements collected along Measured Section 1.

Dip Direction	Dip (degrees)	Latitude	Longitude	Measured Section #
49.0	6.4	38.76508843	-108.25513115	1
42.0	23.7	38.76510670	-108.25518664	1
15.1	31.5	38.76508155	-108.25519351	1
26.0	24.8	38.76508155	-108.25519351	1
32.7	22.8	38.76510703	-108.25519477	1
42.4	34.1	38.76509878	-108.25516820	1
11.4	3.2	38.76509878	-108.25516820	1
146.4	9.1	38.76493856	-108.25477048	1
45.6	28.0	38.76494728	-108.25475707	1
25.4	20.8	38.76494862	-108.25475656	1
5.2	17.3	38.76494694	-108.25477073	1
41.0	17.3	38.76494648	-108.25477492	1
24.5	28.3	38.76501081	-108.25480158	1
36.5	21.7	38.76776900	-108.24304500	1
13.2	33.9	38.76780200	-108.24305100	1
155	25	38.76784300	-108.24305100	1
50	24	38.76784400	-108.24304900	1
42	19	38.76787200	-108.24304200	1
60	14	38.76788900	-108.24303000	1
41	11	38.76800300	-108.24308400	1
54	6	38.76801500	-108.24305700	1
60	27	38.76803600	-108.24307200	1
1	9	38.76806000	-108.24299000	1
60	5	38.76813200	-108.24297400	1
6	15	38.76806100	-108.24291400	1

Appendix E-5. Summary of latitude and longitude taken for paleocurrent measurements collected along Measured Section 1.

Dip Direction	Dip (degrees)	Height in Measured Section (ft)	Measured Section #
8	19	86	1
35	28	89	1
44	14	91	1
206	12	91	1
224	20	92	1
25	6	95	1
25	12	101	1
41	13	103	1
63	2	102	1
74	10	103	1
22	14	103.5	1
5	4	105	1
336	20	105	1
33	4	108	1
4	21	111.5	1
9	11	111	1
55	4	115	1
50	26	114	1
340	6	115	1
39	34	125	1
16	5	135	1
21	5	3	2
90	14	4.5	2
15	21	5	2
52	20	12	2
66	19	15	2
58	22	18	2
31	16	17	2
65	10	19	2
72	30	20	2
94	24	25	2
84	2	24	2
36	12	27	2
10	5	26	2
32	15	28	2
46	15	30	2
19	11	34	2
51	17	35	2
16	14	36	2
80	15	35	2
68	25	35	2
10	20	37	2
28	8	39	2
45	20	34	2
47	15	38	2
50	16	41	2
2	19	43	2
90	14	44	2
35	10	45	2
352	80	47	2
51	80	48	2
44	40	49	2
55	60	55	2
43	40	57	2

Appendix E-5. Summary of paleocurrent measurements collected along Measured Sections 1 and 2 and what footage they were recorded at.

APPENDIX F

Dakota Formation Sedimentology

Sedimentology

The Dakota Formation begins with a granule-pebble conglomerate at the K-2 unconformity and is overlain by the bi-directional cross-stratified sandstone facies. Above that is a thick section of unconsolidated laminated mudstone with some competent bedding seen at the top of the unit with a thick section of bi-directional cross-stratified sandstone and current-rippled sandstone above.

Key Lithofacies Descriptions

Dakota facies A: granule-pebble conglomerate

The granule-pebble conglomerate facies in the Dakota Formation is composed of brown, contorted to horizontally bedded conglomerate. The matrix is a medium to very coarse grained, subround sand. Framework grains are gray, brown, and black, subround, granule and pebble sized clasts (<2 cm; 0.78 in). Clasts are predominately chert and flint with some silicified limestone and quartzite. Flute-like sole marks are found at the base of the conglomerate facies overlying the Burro Canyon gray-green mudstone facies.

Dakota facies B: cross-stratified sandstone

The cross-stratified sandstone facies is composed of tan to brown, varying medium-scale cross-stratified sandstone. Sandstone is fine to medium grained, subround, well sorted, and sometimes fissile and silty. Stratification observed includes tabular-tangential cross-stratification and wedge-tangential cross-stratification with beds approximately .1m to 0.3 m (0.33 ft to 1 ft). Foresets are sometimes low-angle. Black mud chips are common throughout the units.

Dakota facies C: laminated mudstone

The laminated mudstone facies is a dark gray, thinly-laminated, carbonaceous mudstone that can be found interbedded with a brown, silty, ripple-laminated mudstone. Mudstone is very unconsolidated and difficult to see bedding in most areas. Where the stoss-side of ripples can be seen, length is approximately 3 cm (1.2 in) and lee face is approximately 0.5 cm to 1 cm (0.19 in to 0.4 in) in height.

Dakota facies D: current-rippled sandstone

The current-rippled sandstone is a tan to brown, rippled sandstone with some gray to black mud chips throughout. The sand is fine grained, well sorted, and subangular. The ripple crests are asymmetric. The stoss-side is best preserved and varies between approximately 4 cm to 7 cm (1.5 in to 2.7 in) in length. The lee face measures approximately 0.5 cm (0.19 in) in height where it is preserved.

Dakota facies E: bi-directional cross-stratified sandstone

The bi-directional cross-stratified sandstone facies is composed of a tan to brown, bi-directional to sometimes swaley (concave-upward) cross-stratified sandstone. The sand is fine to medium grained, moderately sorted, subangular, and fissile with some gray to black lithic fragments found throughout. Swale package thicknesses range from approximately 5.08 cm (2 in) to 10.16 cm (4 in). Minor coal stringers approximately 1 mm (0.03 in) in length are found.

Interpreted Environment of Deposition

The Dakota formation began deposition in a high-sinuosity fluvial environment and progressed through swamp-marsh and estuarine and tidal channels in the Dakota Formation as the Mancos Sea approached from the northeast.

The Dakota Formation is interpreted to be composed of sinuous fluvial deposits that grade into swamp-marsh and estuarine- and tidal-channel environments. The basal conglomerate is considered an unconformity lag and together with the cross-stratified sandstone unit above it represents sinuous fluvial deposits on the lower-coastal plain. Thick deposits of carbonaceous mudstone are indicative of swamp or marsh environments. Coal interbeds are observed in the mudstone unit, which were deposited where swamps persisted long enough and accumulated sufficient vegetation (Young, 1973). Above the swamp-marsh deposits rests thick accumulations of estuarine- and tidal-channel deposits. The sandstone units in the Dakota Formation are mostly aggradational, which is a prominent feature of an estuarine environment, as compared to a typical coarsening-upward trend of a deltaic deposit (Nichols, 2009). Current ripples and bidirectional cross-stratification are the main environmental indicators observed in the fine- to medium-grained sandstones. The current-rippled sandstones are indicative of estuarine channels flowing into a lagoonal environment. Coal stringers found in these sandstones were deposited during periods of washover into the lagoon area (Walker and Cant, 1984). The interbedded carbonaceous-laminated mudstone and ripple-laminated siltstone was deposited in mudflats along the margins of estuarine channels (Young, 1973). Bidirectional cross-stratification (bi-directional cross-stratification) is the product of ebb- and flow-tide deposits in tidal bars and channels flowing to and from the sea to the northeast during this time (Walker and Cant, 1984; Nichols, 2009).

Appendix F-1. Key lithofacies of the Dakota Formation. A) granule-pebble conglomerate, B) cross-stratified sandstone, C) laminated mudstone, D) current-rippled sandstone (image taken from above), E) bi-directional cross-stratified sandstone (bi-directional foresets bounded by swale-like bounding surfaces).

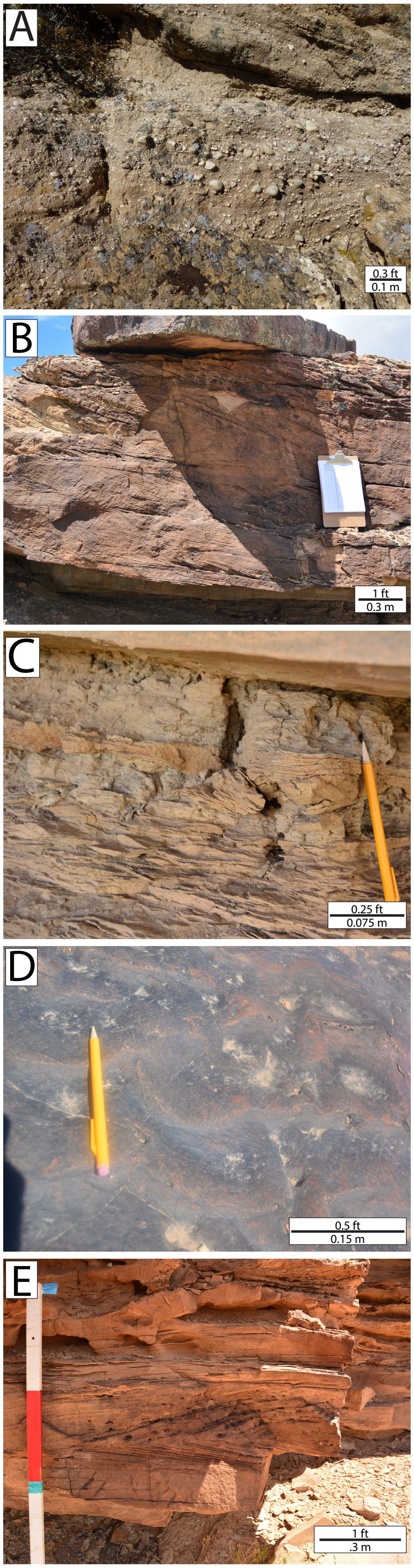

Formation	Facies	Grain Size	Grain Shape/ Sorting	Dominant Features	Environment of Deposition
Dakota	granule-pebble conglomerate	medium-very coarse sand matrix; <2 cm clasts	subround, poorly sorted matrix; round-subround clasts	contorted to horizontal bedding	high-sinuousity fluvial, unconformity lag
Dakota	cross-stratified sandstone	fine-medium	Subround, well sorted	varying medium-scale cross-stratification, sometimes fissile and silty, minor black mudchips	high-sinuosity fluvial
Dakota	laminated mudstone	clay	N/A	thinly laminated carbonaceous mudstone interbedded with ripple laminated silty mudstone	swamp or marsh
Dakota	current-rippled sandstone	fine	subangular, very well sorted	ripples with asymmetric crests	estuarine channel fill
Dakota	herringbone cross-stratified sandstone	fine-medium	subangular, moderately sorted	bi-directional cross-stratification	tidal bar and channel fill

Appendix F-2. Summary of key lithofacies observed in the Dakota Formation in Escalante Canyon.